

Electrical Impedance Tomography for Cardiovascular Imaging and Monitoring

by

Symon Stowe

A thesis submitted in partial fulfillment of the requirements for the
degree of

Ph.D.

in

Biomedical Engineering

Carleton University

Ottawa, Ontario

© 2021

Symon Stowe

*To my parents, sisters and those that supported this project
unknowingly ...*

Abstract

This thesis serves to show the background, methods, planned methods and timeline for the final thesis. The thesis will consist of 6 chapters, in introduction to give background and motivation for the research

Acknowledgements

Write here

Contents

Abstract	i
Acknowledgements	i
Contents	ii
List of Figures	iii
List of Tables	iv
list of Acronyms	v
1 Introduction	1
1.1 Problem	2
1.2 Thesis objectives	4
1.3 Contributions	5
1.3.1 Publications	7
1.3.1.1 Published works related to the thesis:	7

2	Background	8
2.1	Impedance Imaging	8
2.2	Bioimpedance	9
2.2.1	The Cardiac Cycle	10
2.2.2	Bioimpedance of Perfusion	13
2.3	Perfusion Imaging	15
2.3.1	Nuclear Medical Imagaing	16
2.3.2	CT	17
2.3.3	MRI	18
2.3.4	EIT	19
2.4	Electrical Impedance Tomography	22
2.4.1	EIT measurements	22
2.4.1.1	Electrodes	22
2.4.1.2	Current injection and voltage measurement	23
2.4.2	Imaging Techniques	26
2.4.3	Forward Problem	26
2.4.4	Discretization and the Finite Element Method	29
2.4.5	Inverse Problem	30
2.4.5.1	Regularization	30
2.4.5.2	Image Reconstruction	31
2.4.5.3	Image Reconstruction with GREIT	32
2.4.6	Internal Electrodes	34
2.4.6.1	Motion Correction	34

2.5	Summary	34
3	Bolus- and frequency-based perfusion	35
3.1	Introduction	35
3.2	Methods	39
3.2.1	Overview	39
3.2.2	Animals	40
3.2.3	Data Acquisition and Image Reconstruction	41
3.2.4	Functional EIT Images	43
3.2.4.1	Bolus injection image (P_B)	44
3.2.4.2	Frequency-Filtering	44
3.2.4.3	Ensemble Averaging	46
3.2.5	Image Comparison	48
3.2.6	Statistical Analysis	49
3.3	Results	49
3.4	Discussion	53
3.5	Summary	57
4	FEM mesh refinement for 3D EIT	58
4.1	Motivation	58
4.2	Introduction	58
4.3	METHODS	61
4.3.1	Overview	61
4.3.2	Mesh Generation	61

4.3.3	Simulation	66
4.3.4	Electrode refinement for arbitrary FEMs	68
4.4	Results	68
4.5	Discussion	73
4.6	Summary	76
5	Custom EIT Meshes	78
5.1	Introduction	78
5.2	Methods	81
5.2.1	Automatic segmentation of the thorax	82
5.2.1.1	External boundary	83
5.2.1.2	Chest cavity	83
5.2.1.3	Lungs	85
5.2.2	Manual segmentation correction	87
5.2.3	Mesh generation	92
5.2.4	Evaluation on ARDS patients	92
5.3	Results	93
5.4	Discussion	97
5.5	Summary	100
6	Internal Electrode Sensitivity	102
6.1	Introduction	102
6.2	Methods	105
6.2.1	Tank model	105

6.2.2	Image reconstruction	106
6.2.3	Sensitivity calculation	107
6.2.4	Current injection and measurement	107
6.3	Results	109
6.3.1	Sensitivity in an ovine model	109
6.4	Discussion	113
6.5	Summary	115
7	Internal Electrode Motion	116
7.1	Introduction	116
7.2	Methods	118
7.2.1	Simulations	119
7.2.1.1	Tank models	119
7.2.1.2	Measurements	121
7.2.2	Movement correction	121
7.2.3	Image comparison	124
7.2.4	<i>In-vivo</i> recordings	125
7.2.4.1	Internal electrode probe design	125
7.2.4.2	Electrode placement	125
7.2.4.3	Ovine model	127
7.2.4.4	Reconstruction	127
7.2.4.5	Pulsatile amplitude	127
7.3	Results	129
7.3.1	Simulation	129

7.3.2 <i>In-vivo</i>	130
7.4 Discussion	134
7.5 Summary	137
8 Conclusion	139
8.1 Summary of Findings	139
8.2 Future Work	139
Appendices	140
A GMSH models	141
A.1 Tank model	141
A.2 Internal probe model	141
B Algorithms	142
B.1 External boundary	143
B.2 Ribcage	144
B.3 Lungs	144
Bibliography	140

List of Figures

1.1	Overview of thesis objectives	5
2.1	Current and Equipotential lines	9
2.2	Sketch of the anatomical heart	12
2.3	Example ECG waveform	13
2.4	Adjacent and "skip 4" stimulation patterns	25
3.1	Overview of the EIT analysis methods	42
3.2	Selection of the bolus signal	45
3.3	Frequency analysis methods	47
3.4	Ensemble averaging analysis	48
3.5	Jaccard index scores	50
3.6	Example perfusion images	52
4.1	Example meshes for various refinement strategies	63
4.2	Mesh size surrounding the electrode	64
4.3	Balance point calculation method	65
4.4	Mesh sensitivity error vs. elements per electrode	70

4.5	Sensitivity distribution and regions of interest	71
4.6	Sensitivity error with shifting node balance	72
4.7	Advanced mesh example of an internal probe	75
5.1	Raw CT images at the 4 th intersoital space	81
5.2	Mesh generation method overview.	82
5.3	Boundary segmentation methods.	84
5.4	Chest cavity segmentation methods.	86
5.5	Lung segmentation methods.	88
5.6	Manual segmentation data loading	89
5.7	Manual segmentation interface with initial input	90
5.8	Manually corrected segmentation	91
5.9	Lung segmentation results	94
5.10	Custom and generic meshes	95
5.11	Example ventilation distributions	96
5.12	Example ventilation distributions	97
6.1	Internal electrode configurations	106
6.2	Current injection patterns with internal electrodes	108
6.3	Internal electrode simulation reconstructions	110
6.4	Sensitivity with different internal electrode configurations	111
6.5	Sensitivity using internal electrodes with modified injection patterns .	112
6.6	Sensitivity distribution in a lamb model	113
7.1	Spherical and cylindrical internal electrodes	120

7.2	Motion correction methods	124
7.3	Probe prototype	126
7.4	Ovine model with internal probe	128
7.5	Results of the probe location correction	131
7.6	Results of the probe location correction	132
7.7	Results of the probe location correction	133

List of Tables

4.1	Parameters used to generate meshes	67
7.1	Ovine model with internal probe	129
7.2	Ovine model with internal probe	130

Chapter 1

Introduction

Electrical impedance tomography (EIT) is an imaging modality that uses an arrangement of electrodes to simultaneously apply stimulation currents and measure the resulting electric potentials. Measurements of potential at the electrodes are used in conjunction with prior information to reconstruct images of the internal conductivity. In biomedical applications, the variance in conductivity between different tissue types and fluids enables non-invasive imaging of functional activity using electrodes on the body surface.

Thoracic EIT focuses on imaging cardiopulmonary activity using a belt of electrodes placed around the ribcage. In images of the chest, the signal is often dominated by impedance changes due to air movement in the lungs. The much smaller signals due to blood flow are of great interest for continuous monitoring and diagnostic applications, but are challenging to identify.

This thesis explores techniques to improve sensitivity to blood movement, or

perfusion, in EIT through the development of novel meshing techniques and electrode configurations incorporating internal electrodes. We investigate the current limitations of perfusion monitoring in 2D, and analyze novel meshing techniques and electrode placements for their ability to improve thoracic imaging and increase sensitivity to blood flow.

1.1 Problem

EIT can be used to image blood movement in two ways. First, it is possible to track the flow of blood using a conductivity-contrasting agent injected into a vein or artery and second, filtering the signal to isolate cardiac-frequency impedance changes. Using a conductive bolus injection to image perfusion has been well established and can give an easily detectable signal when using large volumes or high concentrations of the contrasting agent, but they do not allow continuous monitoring and frequent injections may pose risks to the patient. In thoracic EIT bolus injections also typically occur during apnea to facilitate removal from the respiratory component. Filtering techniques for perfusion imaging are much more appealing for monitoring applications as they are less invasive and could be used continuously, but they present several challenges.

The primary challenge is the small amplitude of the signal. Impedance changes related to cardiac activity are often an order of magnitude smaller than signals related to respiration and can be challenging to identify without additional signals like an electrocardiogram (ECG), and averaging many heartbeats together. When

averaging over several heartbeats, the ability of the system to monitor in real time is greatly diminished. Additionally there is some uncertainty surrounding the source of cardiac-frequency impedance changes. It is unclear to what extent the impedance changes stem from pulsatile motion in the thorax compared to the movement of blood, and if they can be used as a true measure of perfusion.

EIT is minimally invasive, requiring only the application of electrodes to the body surface, but does not have high sensitivity in the central regions of the chest where perfusion changes are likely to occur. As electrical current travels through the body it diffuses away from the electrodes, travelling in three dimensions along the paths of least resistance. EIT is most sensitive to impedance changes close to the electrodes where the current density is highest, and along the path of the injected current.

The placement of electrodes internally has the potential to increase current density and sensitivity in the center of the thorax. The benefits of internal electrodes have been simulated in 2D showing great improvements in reconstruction accuracy and sensitivity (Nasehi Tehrani *et al.*, 2012a), but in practice there are several challenges to overcome. Due to differences in physiology it is challenging to model the correct location of the internal electrodes between subjects and electrodes placed internally may move with relation to the external electrodes during different physiological processes. To accurately reconstruct images with internal electrodes an accurate model is required with precise placement of electrodes and a model that matches the subject and is refined to meet the accuracy requirements. It is in part due to these challenges that internal electrodes have not been widely used in real-world situations, and to our knowledge no implementation of internal electrodes in conjunction with a 3D

arrangement of external electrodes has been used for *in-vivo* imaging.

The applications of an EIT system with increased sensitivity to perfusion changes in the thorax are extensive. Methods to monitor blood pressure non-invasively are currently under development and could be greatly improved with increased sensitivity near the region of interest. Increased sensitivity near the heart could enable EIT to be realized as a low-cost solution to monitor and image hemodynamic activity more accurately.

1.2 Thesis objectives

The goal of this project is to improve sensitivity of EIT to perfusion using improved mesh accuracy and custom electrode locations. This thesis approaches problem from three angles (figure 1.1). We investigate the limitations of current perfusion monitoring techniques, advanced meshing techniques, and novel electrode configurations with internal electrodes and their applications to improve thoracic EIT.

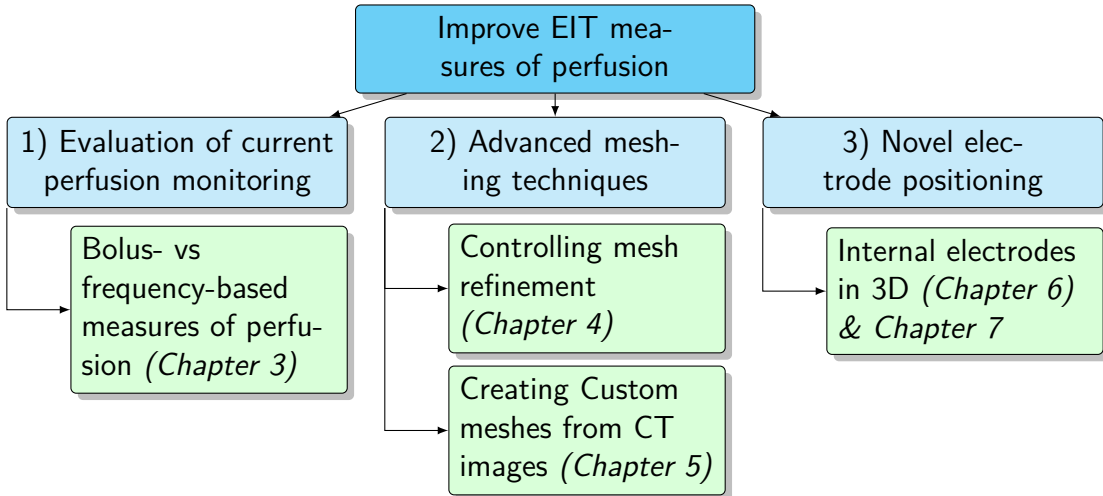


Figure 1.1: We aim to improve EIT measures of perfusion through 3 avenues. 1) Comparing and investigating the limitations of existing perfusion imaging methods; 2) Advancing meshing techniques; and 3) Using novel electrode locations consisting of a 3D external configuration with internal electrodes.

1.3 Contributions

This thesis presents several contributions to the field of perfusion imaging and meshing in EIT.

- A method to determine the node distribution in a finite element model mesh to reduce error in sensitivity calculations. Chapter 4 presents an analysis between meshing software commonly used in EIT and recommends a technique to place a fixed number of nodes that maximizes sensitivity accuracy. A finer node density has often been suggested near the electrode due to the higher sensitivity, but no analysis was available to determine where a set number of nodes should be located in a model to minimize sensitivity error. Using a balance point technique this chapter was able to determine the best distribution of nodes to calculate the sensitivity of voltage measurements to conductivity

changes.

- A tool to generate accurate, custom meshes of arbitrary boundaryies for EIT reconstruction from from CT images. Chapter 5 documents the design and validation of a tool to generate meshes for image reconstruction from CT images. diagnostic CT images were automatically segmented and a tool to manually check the segmentations and generate meshes was created.
- An analysis of 3D electrode placmenets with intenal electrodes on internal sensitivity. Chapter 6 presents an analysis of the sensitivity patterns corresponding to internal electrodes when used with 2 planes of external electrodes. Internal electrodes are expected to increase sensitivity in the center of the model, but it is not clear to what extent image reconstructions may be improved, or how many electrodes should be placed internally. This chapter provides an analysis of the sensitivity when using internal electrode in 3D with different injection patterns.
- A method to reconstruct images using internal electrode measurements in the presence of noise. Chapter 7 demonstrates the effect of internal electrode probe motion on image reconstruction and presented a technique using the interferance in reconstructed images due to the movement artefact to create a model with a corrected probe location. This technique improves reconstruction performance and noise levels in the presence of electrode motion.

1.3.1 Publications

1.3.1.1 Published works related to the thesis:

- Stowe, S., Boyle, A., Sage, M., See, W., Praud, J.-P., Fortin-Pellerin, É., & Adler, A. (2019). Comparison of bolus- and filtering-based EIT measures of lung perfusion in an animal model [Publisher: IOP Publishing]. *Physiol. Meas.*, 40(5), 054002
- Stowe, S., Zhao, Z., Huxter, E., He, H., Long, Y., & Adler, A. (2021b). Generating forward models from CT images for ventilation monitoring in ARDS patients. *Proceedings of the 21st International Conference on Biomedical Applications of Electrical Impedance Tomography*, 20
- Stowe, S., & Adler, A. (2020). The effect of internal electrodes on electrical impedance tomography sensitivity [ISSN: 2694-0604]. *2020 42nd Annual International Conference of the IEEE Engineering in Medicine Biology Society (EMBC)*, 1457–1460
- Stowe, S., Samson, N., Nadeau, C., Morin, C., Praud, J.-P., Fortin-Pellerin, É., & Adler, A. (2021a). Using esophageal electrodes for increased sensitivity to cardiac-frequency impedance changes. *Proceedings of the 21st International Conference on Biomedical Applications of Electrical Impedance Tomography*,

Chapter 2

Background

This section presents the this is short and needs a lot more detail and also figures.

This section briefly reviews the current techniques for lung perfusion and hemodynamic monitoring, and provides a general overview of the state of 3D EIT as used for thoracic imaging and monitoring.

2.1 Impedance Imaging

Impedance imaging has been in use since the early 1900s for geophysical applications. Originally introduced as a technique to image below the earth's surface, current was transmitted between two electrodes placed into the ground and any anomalies in subsurface conductivity produced deviation in the equipotential lines. Including current injections and measurements from multiple locations and using known electrical properties of geological structures Conrad Schlumberger identified features of underground geological structures (Allaud and Martin, 1977).

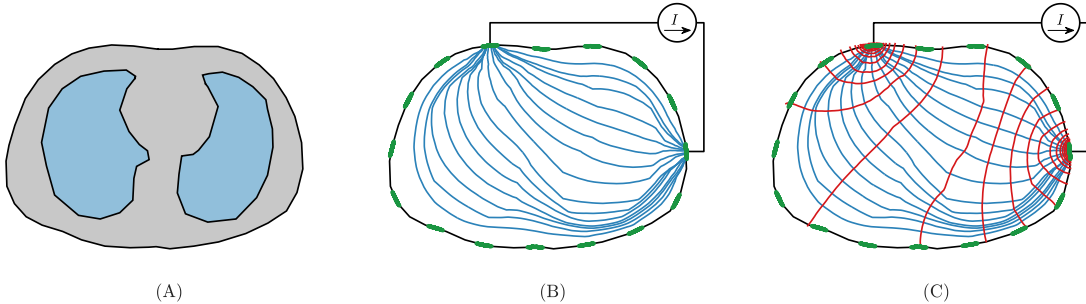


Figure 2.1: (A) A body comprising tissues of different conductivity, (B) Electrodes are placed on the surface and current is injected between a pair or electrodes. The current pathways are indicated by the blue lines. (C) The resulting equipotential lines within the body are shown in red.

These same techniques can be applied in biomedical applications where voltage is measured on an array of body surface electrodes while current is applied between select electrode pairs (figure 2.1). Due to impedance differences associated with biological tissues and their physiological function (Geddes and Baker, 1967; McAdams and Jossinet, 1995), EIT has been proposed for a wide range of applications from thoracic monitoring (Frerichs *et al.*, 2017) to neuronal and brain imaging (Holder, 1992).

2.2 Bioimpedance

In thoracic imaging the most commonly measured impedance changes occur due to movement of air in the lungs, the flow of blood, and the motion of organs (Adler and Boyle, 2017). During inhalation, the volume of air in the lungs increases, lowering the conductivity of the lung tissue. The resistivity of lung tissue varies significantly

between expiration and inspiration giving a value of $7 \Omega \text{ m}$ during expiration and $23 \Omega \text{ m}$ during inspiration at 100 kHz (Witsoe and Kinnen, 1967), resulting in a measurable variation in impedance during respiration (Eyüboğlu *et al.*, 1989). There are also other significant sources of impedance change that make EIT signal interpretation challenging. Simulations have attributed up to 20 percent of the respiratory signal to the effect of chest expansion and movement of the chest wall (Adler *et al.*, 1994).

The source of impedance changes due to the flow of blood is even more complex. Since the resistivity of blood is so much lower than other tissues ($1.5 \Omega \text{ m}$), the increase of blood due to pulsatile flow should decrease the impedance of structures it passes through by a detectable amount (Eyüboğlu *et al.*, 1989). It is often assumed that the component of EIT images at the cardiac frequency is related to the perfusion of blood, but the exact source of cardiosynchronous EIT signals is unclear (Nguyen *et al.*, 2012; Patterson, 2010). A continuous flow of blood alone is insufficient to induce a significant impedance change, as the volume and concentration of the conductive medium is unchanged. Any impedance-based measure of perfusion relies on the cardiosynchronous EIT signals which have numerous possible sources (Adler *et al.*, 2017b).

2.2.1 The Cardiac Cycle

The cardiac cycle consists of the activity in the heart between the beginning of one heart beat, and the next. There are two main stages of the cardiac cycle: the diastole, when the heart relaxes and is filled with blood, and the systole, when contraction

of the heart pumps blood to lungs and all other body systems (Pappano and Wier, 2019). A simplified anatomy of the heart is presented in figure 2.2. Since ECG recordings are frequently used to synchronize EIT data, it is helpful to look at the timing of the cardiac cycle as it relates to features of ECG traces. An example ECG waveform is pictured in figure 2.3.

During the first stage of the cardiac cycle is the ventricular diastole, indicated by the P wave on an ECG trace, during which the heart relaxes and expands pulling blood into the ventricles from the atria (Pappano and Wier, 2019). Blood enters the atrium on the right side of the heart through the superior and inferior vena cava and on the left side of the heart, the atrium is filled by oxygenated blood from the lungs through the pulmonary veins (Pappano and Wier, 2019). Next is the atrial contraction during which time the atria pump additional blood into the ventricles, and the ventricular volume and pressure is maximized. At the peak of the ventricular volume, the ventricles contract and depolarize which corresponds to the QRS complex (Pollock and Makaryus, 2021). On the right side of the heart, deoxygenated blood is pumped to the lungs where it perfuses into the lung tissue, and on the left side of the heart oxygenated blood is pumped to the rest of the body through the aorta (Pappano and Wier, 2019). The smallest volume in the ventricles occurs after the ventricular repolarization represented in the ECG by T wave (Pollock and Makaryus, 2021).

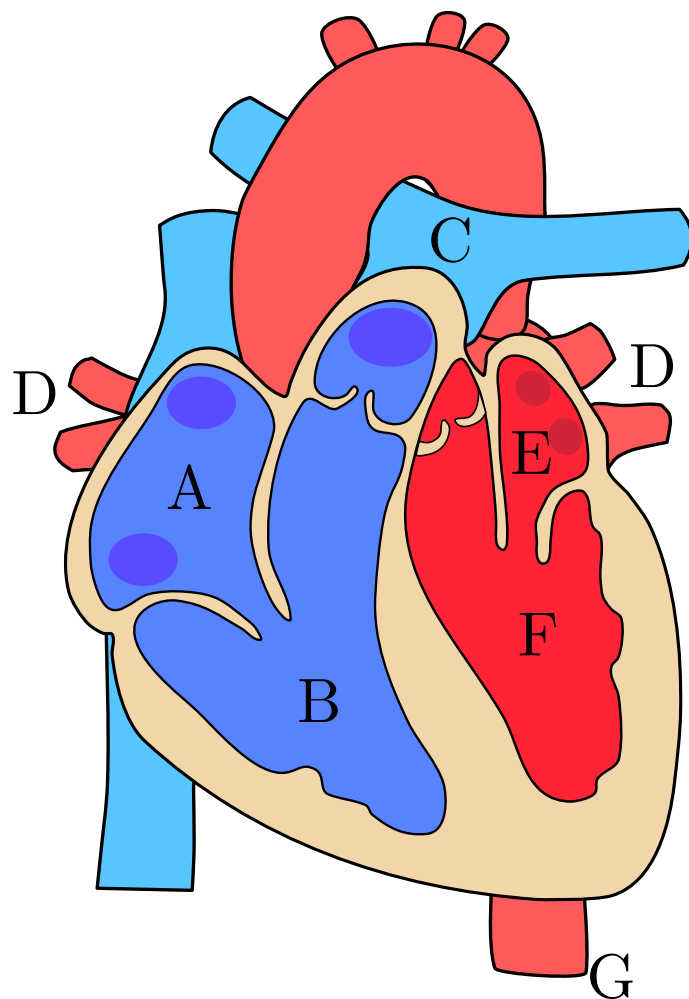


Figure 2.2: The pathway of the blood from entry to the heart to the descending aorta is indicated by the letters. Deoxygenated blood enters the heart through the right atrium (A) where it is moved to the right ventricle (B). From there it passes through the pulmonary artery (C) into the lungs where it perfuses and is oxygenated. Blood return from the lungs through the pulmonary veins (D) then enters the left atrium (E). Finally, the blood is pumped from the left ventricle (F) to the rest of the body through the aorta, and the descending aorta (G).

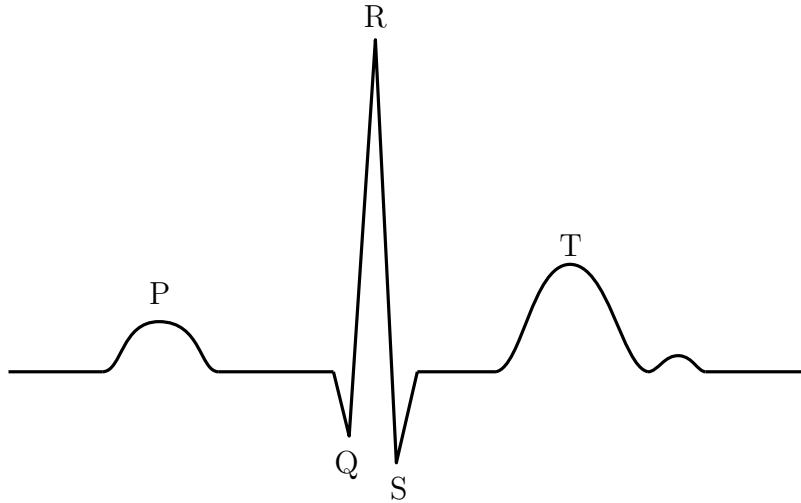


Figure 2.3: An example ECG waveform to compare electrical signals in the heart to blood volume changes. The P wave represents the beginning of the cardiac cycle with the ventricles begin to fill. The QRS complex corresponds with ventricular depolarization and occurs as the ventricles contract they contract. The beginning of the QRS complex corresponds with the maximum ventricular volume. The minimum volume in the ventriles occurs after ventricular repolarization represented by the T wave.

2.2.2 Bioimpedance of Perfusion

There are several factors that may contribute some part of the impedance change during the cardiac cycle. Some of these factors include:

- Changes in blood volume within the heart as blood is pumped. As the ventricles fill with blood the volume increases and results in a more conductive heart (Nyboer *et al.*, 1970).
- Variations in arterial and blood vessel volume. Due to the elasticity of arteries and blood vessels, the pulsatile flow of blood passing through results in variation of vessel diameter, affecting the impedance (Eyüboğlu *et al.*, 1987).
- Physical deformation of structures due to motion of the heart. The motion of the heart can have significant contribution to cardiosynchronous EIT im-

ages (Adler *et al.*, 2017b; Proen  a *et al.*, 2015), with simulations showing that heart motion was the main contributor to impedance change due to the ventricle (Proen  a *et al.*, 2015).

- The orientation of red blood cells. During pulsatile flow the orientation of red blood cells changes, which had been shown to affect the impedance of the blood (Gaw, 2010).
- Ballistic forces in the body generated by the heart. During each heartbeat blood is pumped downwards through the descending aorta with a large force pushing the rest of the body upwards (Gordon, 1877). Different directions of flow in the aorta result in a repeating ballistic signal on the rest of the body (Kim *et al.*, 2016). This results in motion on the electrodes and body which can introduce significant artefacts in EIT signals (Adler *et al.*, 1994).

The contribution of each of these factors will ultimately depend on the placement of the electrodes and the specific geometry and physiology of a patient. When imaging changes in stroke volume, changes relating to posture, breathing and changes in belt position resulted in changes that overpowers the perfusion signals (Patterson *et al.*, 2001).

Despite the challenges of isolating cardiosynchronous EIT signals related to perfusion there is still a great interest in improving accuracy and stability due to the unique advantages offered by EIT over current state-of-the-art methods.

2.3 Perfusion Imaging

Determining the flow of blood within vital organs such as the heart, brain and lungs allows doctors to make quick decisions to treat patients in life threatening situations. In the brain perfusion imaging can be used to diagnose and monitor dementia and Alzheimer's disease (Barker *et al.*, 2014; Dougall *et al.*, 2004), or to detect and diagnose ischemic strokes (Koenig *et al.*, 1998; Konstas *et al.*, 2009). Perfusion images of the heart can be used to diagnose ischemic heart disease (Prvulovich and Bomanji, 1998), which is caused by a reduction of blood flow to the heart, typically due to a build-up of plaque in the arteries of the heart (Mendis *et al.*, 2011). Ventilation/perfusion scans can be used in the lungs to measure the distribution of perfusion and ventilation in the lungs (Mortensen and Berg, 2019). The primary use is to detect mismatches between the ventilation in perfusion to detect pulmonary embolisms (PIOPED-Investigators, 1990).

Nuclear medicine has been at the forefront of perfusion imaging, but has a long acquisition time, and images can be fuzzy and challenging to interpret (Prvulovich and Bomanji, 1998). Recent developments in computed tomography (CT) and magnetic resonance imaging MRI imaging yield clearer images and can give metrics regarding blood flow and blood volume over a period of time (Prvulovich and Bomanji, 1998). EIT has been proposed as a technique to monitor perfusion due to its sensitivity to blood movement, and development is currently underway to establish EIT as a technique to monitor perfusion (Nguyen *et al.*, 2015; Nguyen *et al.*, 2012), blood flow (Braun *et al.*, 2018a; Braun *et al.*, 2018b), and blood pressure (Proen  a *et al.*, 2020; Proen  a *et al.*, 2017). The following section explores the advantages and

pitfalls of state of the art perfusion monitoring techniques.

2.3.1 Nuclear Medical Imaging

The two primary nuclear medicine techniques used for perfusion imaging are single-photon emission computed tomography (SPECT), and scintigraphy. These techniques image gamma rays that are emitted from a gamma-emitting radionuclide injected into the patient (Mettler and Guiberteau, 2006). The radioisotopes are integrated into drugs that enable them to travel to a specific organ or tissue. Perfusion imaging with scintigraphy and SPECT is primarily used in the lungs and heart. The emitted gamma rays are measured by external detectors called gamma cameras (Mettler and Guiberteau, 2006). The main difference between the two is that SPECT creates 3D images, and scintigraphy images are 2D. Scintigraphy uses a gamma camera placed in a single location, while SPECT uses a detector that rotates around the patient and captures gamma images from several angles. A typical SPECT system rotates 3–5 degrees per acquisition and takes approximately 15–20 minutes to complete a full scan, although scan times can be shorter when multiple detectors are used to capture images from multiple angles simultaneously (Mettler and Guiberteau, 2006).

Nuclear medical imaging can be used to image both ventilation and perfusion which has been used to diagnose pulmonary embolisms (Mortensen and Berg, 2019). Ventilation/perfusion scans are a specific type of perfusion scan that uses lung scintigraphy. During ventilation an aerosolized radionuclide is inhaled through a mask placed over the nose and mouth. To image lung perfusion a different radionuclide is injected and its passage through the lung is imaged. Both phases are imaged

using a gamma camera (Mortensen and Berg, 2019). This technique can be time and labour intensive, and results in radiation exposure to both the technician and patient (Gandev *et al.*, 2005). The duration of a single scan to measure ventilation and perfusion is approximately 15 minutes, including time required to breath the radionuclidite prior to imaging (Hur *et al.*, 2014). Reducing the time required to improve image acquisition time and reduce radiation exposure has been shown to give less reliable measures of perfusion (Hur *et al.*, 2014). Nuclear medicine imaging methods have a lower radiation dose than CT perfusion imaging techniques, but suffer from a much lower resolution and longer imaging time (Aljizeeri *et al.*, 2013). As such CT is becoming the preferred method to image myocardial perfusion (Aljizeeri *et al.*, 2013).

2.3.2 CT

Contrast-enhanced CT has been used since 1980 to estimate perfusion in the brain and estimate perfusion (Axel, 1980). Contrast enhanced perfusion imaging has been used to image perfusion due to ischemic stroke (Koenig *et al.*, 1998; Miles *et al.*, 1991). This technique uses an injection of 25–35 mL of a contrast agent, and the progress of the contrast agent through blood vessels and capillaries near to the brain is imaged over 75–90 seconds. Techniques are typically used to reduce overall radiation exposure, but imaging duration is limited by safety concerns due to radiation exposure (Konstas *et al.*, 2009). Contrast-enhanced CT has also been found to be an effective and cost effective technique to image myocardial perfusion in cardiovascular disease (Aljizeeri *et al.*, 2013), but images require an invasive cardiac

catheterization and pose a risk of radiation exposure to both patients and technicians (Vijayalakshmi *et al.*, 2007).

2.3.3 MRI

There are three main techniques used to image perfusion using MRI. The first uses a contrast agent to image which is used to either induce a reduction of amplitude in images (Jackson *et al.*, 2005) the concentration of contrast agent present in the images can be used as an approximation of perfusion (Jackson *et al.*, 2005). The second technique also uses an injected contrast agent. This technique images the transit of a contrast agent as it travels from the blood into a tissue (Sourbron and Buckley, 2013). In this technique the contrast agent is not imaged directly, but impacts the magnetic properties of water molecules it passes resulting in a change in image intensity in regions with contrast agent (Sourbron and Buckley, 2013). The final technique is arterial spin labelling, which does not rely on an injected contrast agent, but rather applies a magnetic label to the water in blood and the perfusion is estimated by tracing the flow of this labelled blood (Koretsky, 2012).

MRI is typically used for cerebral perfusion imaging due to its safety and lack of ionizing radiation (Watson, 2015). It is not suitable for continuous perfusion imaging due to the acquisition time which ranges from 1-5 minutes depending on the method (Essig *et al.*, 2013), and it can not be used at the bedside.

2.3.4 EIT

EIT has been suggested as an ideal tool to continuously monitor perfusion (Leonhardt and Lachmann, 2012). EIT is cost-effective, non-invasive, does not use ionizing radiation, and images can be acquired continuously at a high sampling rate (Adler and Boyle, 2017). Despite these advantages of EIT, spatial resolution is low, and image accuracy is further limited by artefacts introduced by poor electrode contact and electrode movement (Adler and Boyle, 2017). The spatial resolution of EIT is typically thought to be approximately 20–50% of the electrode separation, but can be affected by the measurement protocol and image reconstruction techniques (Polydorides and McCann, 2002).

EIT has been evaluated for its ability to measure cardiac output and lung perfusion since the late 1980s (Brown *et al.*, 1992; Eyüboğlu *et al.*, 1989; Frerichs *et al.*, 2002; Zadehkoochak *et al.*, 1992). Since then, various configurations of EIT have been evaluated (Borges *et al.*, 2012; Nguyen *et al.*, 2015). Due to the speed and safety of measurement acquisition, EIT might be used to continuously monitor perfusion in subjects much more frequently than current state of the art techniques.

There are two main ways perfusion related changes can be imaged with EIT. Like with many perfusion imaging techniques, a contrast agent can be injected to image the transit of blood through vessels and organs. Typically a sodium chloride bolus with a concentration between 5–20% is used as a contrast agent for EIT (Nguyen *et al.*, 2012), and an algorithm to determine the regional blood flow to the lung and heart (Borges *et al.*, 2012). This technique was found that measures of perfusion using a contrast agent with EIT were highly correlated to SPECT images of perfusion

(Borges *et al.*, 2012). The same study found that pulsatile images of EIT showed little correlation to bolus measures and SPECT scans.

When breathing is paused, the signals based only on the cardiac activity can be more easily extracted. It was found that during apnoea the global impedance recorded with EIT measurements corresponded with stroke volume measured using the thermodilution method with a pulmonary arterial catheter (Fagerberg *et al.*, 2009). Ventilation perfusion ratios have been calculated during apnoea by comparing ventilation and perfusion signal amplitude with a specified region of interest (Fagerberg *et al.*, 2009). There is some concern that the perfusion measured during apnoea may not accurately represent true perfusion during regular respiration as the apnoea impacts the regular respiratory cycle (Leonhardt and Lachmann, 2012), and since apnoea cannot be sustained continuously there is interest in an alternative method to increase sensitivity to cardiosynchronous changes.

The majority of work on perfusion imagingin with EIT has focused on imaging the pulsatile or cardiosynchronous component of EIT data (Nguyen *et al.*, 2012). As discussed in section section 2.2.2 there are many potential sources of the cardiosynchronous signal, and the effect of perfusion related changes is not well understood. Perfusion had been calculated using digital filtering to extract the related componenet of an EIT signal. Deibebe *et al.* (2008) have shown that principal component analysis (PCA) can be used to separate ventilation and cardiac frequency signals and identify the component related to the heart. Once the cardiac-frequency component of the EIT signal is identified the pulmonary component must also be isolated. One of the most widely used techniques is selecting a region of interest that

corresponds to the organ, tissue or flow to me measured (Braun *et al.*, 2018a; Solà *et al.*, 2011).

Techniques to improve accuracy of EIT models and increase sensitivity to cardiosynchronous activity such as internal and 3D electrode configurations could improve accuracy of techniques to isolate pulsatile activity in a specific region, and could enable an improved perfusion measure using EIT, and a means of continuously monitoring perfusion during ventilation. In this thesis we explore the effect of both increased mesh accuracy and internal electrodes, and discuss their potential for improving sensitivity to perfusion with EIT.

2.4 Electrical Impedance Tomography

Most EIT systems consist of: a current source to inject a current between two electrodes; a system to measure differential voltage between pairs of electrodes; and electrodes, applied to the body surface. This section further discusses each of these aspects of EIT and introduces concepts of image acquisition and reconstruction.

2.4.1 EIT measurements

A “frame” of EIT data consists of a series of measurements made on an array of electrodes placed around a region of interest. In this thesis we focus on measurements of the thorax.

2.4.1.1 Electrodes

EIT recordings are made using several types of electrodes. Both polarizable and non-polarizable electrode types are used, silver-silver chloride electrodes are often applied directly to the body and stainless steel, brass, textile and rubber electrodes have also been used (Adler and Boyle, 2017) and are sometimes integrated into electrode belts. The polarization of EIT electrodes is not significant at the frequencies (>20 kHz) that are typically used (Adler and Boyle, 2017).

When making measurements with EIT systems there is very little current flowing through non-injecting electrodes due to the high impedance of the integrated voltmeter (Holder, 2004). For this reason, the effects of the electrode-body impedance are minimal on electrodes that are not injecting current. Measurements that are

largely affected by this impedance on injecting electrodes typically have a phase shift and are often removed before reconstruction.

Changing contact impedance has a large effect on EIT measurements can be influenced by changes in posture or pressure on electrodes (Coulombe *et al.*, 2005). Contact impedance is often improved on electrodes by adding a conductive gel (Waldmann *et al.*, 2017), but it can decrease over long measurements as the gel dries (Lozano *et al.*, 1995).

2.4.1.2 Current injection and voltage measurement

To calculate impedance three main considerations must be made with regard to the injected current: the frequency, amplitude and pattern.

Low frequency currents will preferentially pass around cells through the extracellular fluid due to the high capacitive component of the cell membrane (Foster and Lukaski, 1996), whereas high frequency currents will be more affected by the capacitive component (Holder, 2004). Since EIT requires a linear relationship between the measured voltages and tissue impedance to produce valid reconstructions, it is important to select frequencies of less than 1 MHz to ensure that cell and neural membrane is not the dominant factor in the impedance measurements (Barber and Brown, 1984). Impedance measurements below 100 KHz have shown to be primarily resistive on lung tissue (Witsoe and Kinnen, 1967), and most EIT systems use frequencies between 10 kHz and 1 Mhz (Holder, 2004).

The selection of current amplitudes is primarily selected based on considerations to patient safety (Adler and Boyle, 2017). The guideline defined by IEC 60601-1

(International Electrotechnical Commission, 2021), set a limit of 10 mA on current across all electrodes at 100 kHz, and lower limits at lower frequencies. For EIT frequencies between 20–100 kHz are often used with an injected current between 1–5 mA. In order to meet the guidelines at low frequencies, when injecting sinusoidal currents it is also important to use complete current cycles so that DC currents are not applied to the body (Adler and Boyle, 2017). When using internal electrodes there are additional safety considerations that limit current amplitudes

The pattern of current injection and voltage measurement is commonly referred to in EIT as the stimulation and measurement pattern. Typically a current is injected between two electrodes while the resulting voltages are measured between adjacent pairs. The two most common injection patterns are adjacent, and “skip 4”. Examples of these measurement patterns are shown in figure 2.4 on a 16 electrode system. The terms adjacent and skip 4 describe the space between pairs of injecting or measurement electrodes. Regardless of the pattern, a frame of EIT data is generated in the same way. Current is injected between a pair of electrodes as voltage is measured between all remaining pairs, then current is injected between the next pair of electrodes and voltages are measured again. This results in voltage measurements on each electrode pair for every current injection. For a 16 electrode system this results in 256 measurements in each frame. For a 32 electrode system there are 1024. As mentioned in section 2.4.1.1, voltage measurements made on the stimulating electrodes are often removed resulting in 208 measurements per frame on a 16 electrode system, and 928 measurements per frame on a 32 electrode system.

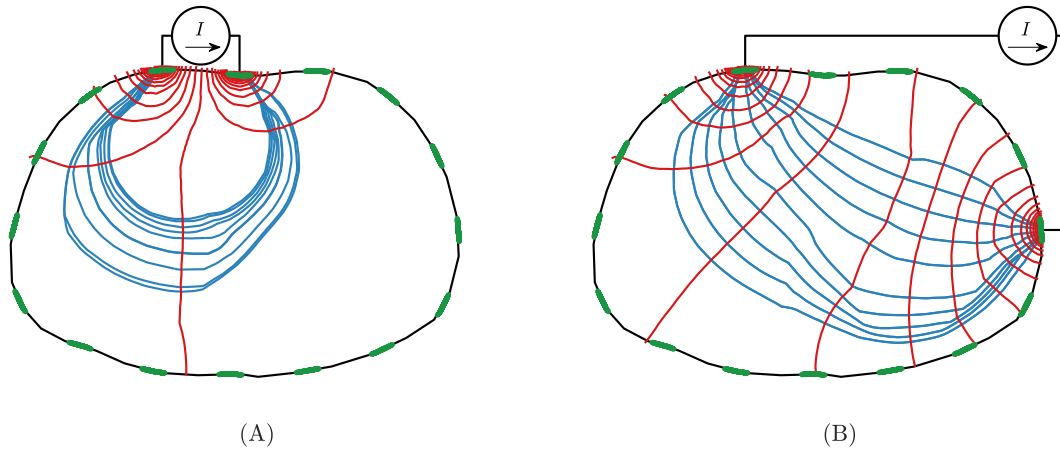


Figure 2.4: Two common stimulation patterns are simulated on a simple human model shown in figure 2.1. Injected current is shown in blue and the resulting equipotential lines are shown in red. (A) An example of an adjacent stimulation pattern. Current is injected between pairs of adjacent electrodes. For each current injection voltage is measured between all sequential pairs. (B) An example of the “skip 4” injection pattern. Current is injected between every 5th electrode skipping 4 between the injecting electrodes. during each current injection, voltage measurements are made using the same skip 4 pattern between each of the 16 electrodes and their corresponding pair. A single frame of data is generated by all measurements made for each possible injection pattern. For 16 electrodes this results in 256 measurements.

2.4.2 Imaging Techniques

There are several challenges that make absolute EIT imaging difficult. The differences in tissue impedance are subtle relative to artefact introduced by unknown boundary locations and electrode positions (Adler and Boyle, 2017; Adler *et al.*, 2015; Nissinen *et al.*, 2009). EIT is instead typically used to reconstruct impedance changes between two points in time.

Time difference EIT is sensitive to the movement of fluids within the body and is well suited to image functional activity such as the inflation of the lungs and the flow of blood. Time-difference EIT is also much more stable in the presence of errors that remain constant such as incorrectly modelled boundary and electrode locations (Adler and Boyle, 2017; Brown, 2003). Frequency difference EIT is also possible based on the different impedance response of tissue types to changing frequencies. Frequency difference uses two or more different frequencies and calculates an image based on the change in electrical properties. Most frequencies used to differentiate between different tissue types are at high frequencies where current starts to flow across the cell membranes. These high frequencies are out of the range of most current EIT systems and frequency changes due to different lower frequencies are limited (Adler and Boyle, 2017). This thesis uses time-difference EIT to images changes in movement and fluid volumes in the thorax.

2.4.3 Forward Problem

In simulation, we have a model with known geometry and impedance and we wish to solve for the voltage at the electrodes due to a stimulation current. This process

is called the forward problem. A model used to calculate a solution for the forward problem is called a forward model.

This problem is well-posed, and can be solved analytically on simple, regular geometries. For the inverse solution we require Maxwell's formulation of Faraday's Law:

$$\Delta \times \vec{E} = -\frac{\partial}{\partial t} \vec{B} \quad (2.1)$$

and Ampere's Law:

$$\Delta \times \vec{H} = \vec{J} + \frac{\partial}{\partial t} \vec{D}. \quad (2.2)$$

To set up the solution we first assume that the current used for EIT is sufficiently low frequency relative to the scale of interest that we can use a quasistatic approximation of Maxwell's equations (Larsson, 2007). Under this assumption the derivative components of equation (2.1) and equation (2.2) can be set to zero giving:

$$\Delta \times \vec{E} = 0 \quad (2.3)$$

and

$$\Delta \times \vec{H} = \vec{J}. \quad (2.4)$$

In this static case the electric field due to a potential can be described by

$$\vec{E} = -\Delta \vec{u}. \quad (2.5)$$

Finally we require Ohm's Law, describing the relationship between the current

density, conductivity and electric field:

$$\vec{J} = \sigma \vec{E}. \quad (2.6)$$

Using the magnetic field identity for the divergence of curl $\Delta \cdot (\Delta \times \vec{H}) = 0$ with equation (2.4), we get

$$\Delta \cdot \vec{J} = 0. \quad (2.7)$$

Combining equation (2.7) with Ohm's Law (equation (2.6)) we get

$$\Delta \cdot (\sigma \vec{E}) = 0. \quad (2.8)$$

And finally with equation (2.5) relating the electric field and potential we get

$$\Delta \cdot \sigma \Delta \vec{u} = 0 \quad (2.9)$$

which gives the relationship between a conductivity distribution and the resulting potential.

The current density on the boundary is given by:

$$j_n = -\vec{J} \cdot \vec{n} = \sigma \Delta \vec{u} \cdot \vec{n}. \quad (2.10)$$

Where \vec{n} is a unit vector normal to the boundary. Equation (2.10) cannot be used in EIT where the current density on the boundary is not uniform (Somersalo *et al.*, 1992). Instead we require a formulation that give current density on injecting

electrodes and no current density on the rest of the boundary (Somersalo *et al.*, 1992). Somersalo *et al.* (1992) give a formulation of a complete electrode model for the voltage on L electrodes (E) where the voltage measured on each electrode (U) is constant.

$$u + z_l(\sigma \Delta u \cdot \vec{n}) = U_l \quad \text{on } E_l, \quad l = 1, 2, \dots, L. \quad (2.11)$$

The impedance of each electrode contact (z) is also typically treated as a constant over the surface of an electrode (Somersalo *et al.*, 1992). This complete electrode model has been shown to predict voltage accurately (Somersalo *et al.*, 1992).

2.4.4 Discretization and the Finite Element Method

For EIT analytic solutions are possible for simple geometries, but in a majority of cases numerical methods are required. One of the primary discretization techniques is the finite element method FEM where the domain is divided into a number of smaller elements. An element is triangular in 2D and tetrahedral in 3D. The collection of nodes, and elements making up a larger model is commonly called a mesh. Each line connecting two nodes of a mesh can be visualized as a resistor, used to model the conductivity of an object.

2.4.5 Inverse Problem

To reconstruct images we must solve for impedance distribution from known voltage measurements. This is known as the inverse problem. The ability to reconstruct impedance distributions from a known voltage distribution is challenging and relies

on the assumption that the relationship between voltage and conductivity is linear (Barber and Brown, 1984). Unlike the forward problem, due to the small number of electrodes relative to the large number of internal elements the inverse probelm is ill-posed (Holder, 2004).

The sensitivity of EIT is often represented by a jacobian matrix, \mathbf{J} , which gives the change in measurement relative to another factor. To reconstruct a conductivity distribution a conductivity jacobian, \mathbf{J}_c , is used which links the change in boundary voltage measurements to the change in impedance. It can be represented by

$$\mathbf{J}_C = \frac{\Delta U}{\Delta \sigma}. \quad (2.12)$$

The jacobian gives the relationship between the conductivity of each voxel, and the resulting measurements (Holder, 2004). In practice the jacobian can be calculated using the adjoint field (Vauhkonen *et al.*, 1999).

2.4.5.1 Regularization

The sensitivity of measurements to changes is vastly different throughout the model. Near electrodes where the current density is high, there is high sensitivity to conductivity changes but there is limited sensitivity away from the electrodes. This contributes to the ill-posed nature of the inverse problem (Holder, 2004). To overcome this regularization must be used to stabalize reconstruction. Regularization imposes restrictions on a minimization problem to ensure a unique solution. In EIT some typical regularization techniques include the maximum *a priori* approach (Adler and Guardo, 1996), Tikhonov regularization (Vauhkonen *et al.*, 1998), and singular value

decomposition (Osteebee, 1998).

2.4.5.2 Image Reconstruction

The standard linear formulation (Holder, 2004) to solve for the conductivity change in each voxel ($\Delta\hat{\sigma}$) for a given set of difference measurements (\mathbf{b}) is

$$\Delta\hat{\sigma} = \mathbf{J}^T \mathbf{W} (\mathbf{J} \mathbf{W} \mathbf{J}^T + \mathbf{W})^{-1} \mathbf{b}. \quad (2.13)$$

Where \mathbf{W} is a covariance matrix that incorporates *a priori* information such as the error weighting, and regularization (Adler and Guardo, 1996). The term $\mathbf{J}^T \mathbf{W} (\mathbf{J} \mathbf{W} \mathbf{J}^T + \mathbf{W})^{-1}$ is also called the reconstruction matrix and can be represented by the term \mathbf{R} , since after initial calculation it typically remains constant for a given model. Conductivity distributions can be solved using the reconstruction matrix using the equation:

$$\Delta\hat{\sigma} = \mathbf{R} \mathbf{b}. \quad (2.14)$$

There are several techniques used to calculate error weighting and prior information represented by \mathbf{W} , such as the NOSER algorithm (Cheney *et al.*, 1990). There are also techniques that have been specifically designed to compensate for the limitations and characteristics of EIT systems such as GREIT (Adler *et al.*, 2009).

2.4.5.3 Image Reconstruction with GREIT

GREIT (Graz consensus Reconstruction algorithm for EIT) is a consensus algorithm that is used to reconstruct EIT images according to limitations and characteristics of typical EIT systems (Adler *et al.*, 2009). The reconstruction matrix calculated with GREIT depends on the forward model, noise model and the desired performance metrics. GREIT uses a forward model that models electrodes using the complete electrode model discussed in section 2.4.3. The forward model has information regarding the stimulation measurement pattern, body geomerty, and electrodes.

GREIT constructs a set of training images using a small (less than 5% of the model diameter) conductive target in the forward model. A training set consists of images of a conductive object placed at many (100–500) locations within the model. A noise model consisting of a gaussian estimate of measurement noise, and measurements with electrode motion noise is generated.

Training targets are blurred so that their diameter increases to 20% of the model diameter, but the position remains constant. This is used as the desired image for a training target. The weighting relative to noise and other perfomance metrics is set to minimize recoonstruction errors between the training target and idea image. The weights are set based on the radius of the training image to penalize changes outside the desired image radius to minimize shape deformation and ringing artefact. The weighting can also be adjusted to meet specific perfomance characteristics of interest. A description of all performance characteristics that can be specified is found in (Adler *et al.*, 2009). When applying the training, weighting is also set to increase uniformity of the resolution in the reconstructed image. Some resolution

near the electrode is lost, but weighting help to ensure that targets reconstruct to the same size through the model.

To calculate a reconstruction matrix (\mathbb{R}), error (ϵ) is minimized over all training targets (k) with respect to the weighting parameters ($\mathbf{w}^{(k)}$), measurements (\mathbf{b}), and the desired images ($\tilde{\mathbf{x}}$).

$$\epsilon^2 = \sum_k \|\tilde{\mathbf{x}}^{(k)} - \mathbf{R}\mathbf{b}^{(k)}\|_{\mathbf{W}^{(k)}}^2 \quad (2.15)$$

To minimize the equation for error we set the derivative of ϵ^2 with respect to the reconstruction matrix equal to 0.

$$\epsilon^2 = \sum_k \|\tilde{\mathbf{x}}^{(k)} - \mathbf{R}\mathbf{b}^{(k)}\|_{\mathbf{W}^{(k)}}^2 \quad (2.16)$$

Grychtol *et al.* (2016) show that equation (2.15) can be rearranged to solve for the reconstruction matrix as:

$$\mathbf{R} = \mathbf{D}\Sigma_t\mathbf{J}^T(\mathbf{J}\Sigma_t\mathbf{J}^T + \Lambda\Sigma_n)^{-1} \quad (2.17)$$

Where \mathbf{D} is the desired image matrix from all training images, Σ_t is the effective covariance of all training targets after weighting with \mathbf{W} and Σ_n is the noise covariance. This reconstruction method is widely used in EIT for both 2D and 3D electrode configurations and is shown to give even resolution throughout the image (Adler *et al.*, 2009).

2.4.6 Internal Electrodes

TODO: ADD overview from wherever I put it!

2.4.6.1 Motion Correction

TODO: Just background

2.5 Summary

TODO: bring it back to the general motivation briefly

Chapter 3

Bolus- and frequency-based perfusion

This chapter had been adapted from:

Stowe, S., Boyle, A., Sage, M., See, W., Praud, J.-P., Fortin-Pellerin, É., & Adler, A. (2019). Comparison of bolus- and filtering-based EIT measures of lung perfusion in an animal model [Publisher: IOP Publishing]. Physiol. Meas., 40(5), 054002

3.1 Introduction

Electrical Impedance Tomography (EIT) uses electrical stimulation and measurements at electrodes on the body surface to reconstruct images of internal conductivity distribution and its changes. The most common application of EIT, experimentally and clinically, has been for imaging of the thorax (Frerichs *et al.*, 2017). Using a ring of electrodes around the chest, EIT is able to calculate images of impedance changes

in the abdomen. Although most research has focused on imaging of ventilation, there is significant interest in imaging cardiovascular phenomena with EIT (Adler *et al.*, 2012; Leonhardt and Lachmann, 2012).

EIT has been evaluated for its ability to measure cardiac output and lung perfusion since the early 90s (Eyüboğlu *et al.*, 1989; Frerichs *et al.*, 2002; Zadehkoochak *et al.*, 1992). Since then, various configurations of EIT have been evaluated (Borges *et al.*, 2012; Nguyen *et al.*, 2015). The effect of posture on EIT images was evaluated by Reifferscheid *et al.* (2011), who showed that changing posture introduces a large and reproducible variability into ventilation distribution as imaged by EIT. Based on results showing a common relationship between the effect of gravity and perfusion in both children and adults (Bhuyan *et al.*, 1989), in newborns we expect to see a comparable directional change in perfusion due to the changes in posture. Recently, Braun *et al.* (2018) evaluated EIT's ability to monitor cardiac output, showing that EIT is more reliable for monitoring cardiac output trends than absolute cardiac output. EIT has also been investigated for monitoring of systemic blood pressure (Solà *et al.*, 2011), and for monitoring of pulmonary arterial pressure (Proença *et al.*, 2017).

EIT measurements are sensitive to blood movement in two main ways. First, it is possible to image the transit of the contrast agent through the heart and lungs via a conductivity-contrasting bolus into the veins and second, through digital filtering of the time series of EIT images at the heart frequency (Leathard *et al.*, 1994). While multiple EIT measures of perfusion are used, their relationship is not well understood. It is currently unclear to what degree pulsatile impedance changes represent blood flow, and how they limit the potential for heart-frequency filtering

to correctly estimate the true perfusion (Nguyen *et al.*, 2012).

Injection of a contrast agent to measure regional lung perfusion has been compared with electron beam computed tomography (EBCT) and determined to be feasible for measuring perfusion across different animals (Frerichs *et al.*, 2002). Perfusion measurement via conductivity contrasts has the advantage of measuring the true perfusion, but requires placement of a catheter to introduce the contrast agent. Bolus-derived measurements cannot be made continuously because they rely upon the circulation of a contrast agent. In addition, the accumulation of NaCl (the main conductivity contrast used) over multiple injections can lead to hypernatremia which limits the rate at which bolus injections can be made.

Calculating the heart-frequency conductivity changes in the thorax offers the benefit of a continuous functional measure calculated directly from EIT signals (possibly in conjunction with a synchronization signal such as the ECG). Heart-frequency EIT signals are typically an order of magnitude smaller than ventilation signals; thus, when measurements are made during tidal ventilation, a large period of data must be used in order to reduce the ventilation signal. On the other hand, measurements during apnoea can be used to eliminate the ventilation signal, but for the safety of the patient the apnoea was limited to 30 s. In healthy human subject of less than one year old it takes a mean of 118 s for the blood oxygen saturation levels to drop below 90% (Fu *et al.*, 1996), however the length of safe apnoea is much shorter for the sick preterm infant. The time period was chosen based on experience in the lab showing that 30 s seconds was not associated with bradycardia or desaturation to less than 90% blood oxygen saturation.

There is a debate within the EIT community about the meaning of heart-frequency EIT signals (Adler and Boyle, 2017; Frerichs *et al.*, 2017). Not all perfusion results in a cardiac-frequency change (for example, continuous blood flow in capillaries), and non-perfusion effects (for example, heart movement in the thoracic cavity) can result in heart-frequency EIT signals. This debate is reflected by the terminology – perfusion vs. pulsatility. Those who prefer “pulsatility” or “heart-frequency FEIT image” seek to emphasise that frequency filtered signals are not “perfusion” (although they may be related). While these pulsatility based EIT images are clearly not a direct measure of perfusion, the signals appear to be useful and are often measured and reported (Bartocci *et al.*, 1999; Ericsson *et al.*, 2016; Halter *et al.*, 2008; Moens *et al.*, 2014). To the authors’ knowledge, no systematic comparison of frequency-based perfusion measures has been published.

The heart-frequency signal can be derived from frequency filtering or ensemble averaging. Frequency-filtering uses a filter to isolate the frequency of heart-frequency conductivity changes, and was introduced by Zadehkoochak *et al.* (1992) and Leathard *et al.* (1994). Frequency filtering is susceptible to interference from ventilation when the heart rate is at a harmonic of the breathing rate. Ensemble averaging is another filtering approach which averages signals at a synchronized time, for example at the QRS peak (Bartocci *et al.*, 1999; Deibebe *et al.*, 2008). The impedance change due to each heart beat is aligned and averaged to give a single heart-related impedance change, representative of all heart-beats in the segment.

In this paper, we are motivated to better understand the relationship between lung perfusion and heart-frequency filtering measures, and between the various fil-

tering approaches used to determine heart-frequency components. Our questions are: 1) to what extent do heart-frequency filtering-based measures correspond to perfusion, 2) what are the advantages and disadvantages of different approaches to heart-frequency filtering of EIT data, and 3) which techniques are recommended. In our experimental protocol, we have selected posture-change to introduce changes in the regional distribution of lung perfusion. These changes are then compared using bolus- and filtering-based EIT measures.

3.2 Methods

3.2.1 Overview

Data were acquired as an additional protocol within a study to determine a baseline for lung damage due to gas ventilation in neonatal lambs. This is part of an effort to establish total liquid ventilation (TLV) as a less-injurious ventilation strategy for the delicate lungs of neonatal subjects (Sage *et al.*, 2018). In order to induce changes in ventilation and perfusion patterns, posture changes were made between supine, prone, left and right lateral positions.

3.2.2 Animals

The study was conducted in accordance with the Canadian Council on Animal Care guidelines upon approval by the animal research ethics board of Université de Sherbrooke (protocol 417-17BR).

Seven healthy neonatal lambs (2–4 days old and 2.95 ± 0.27 kg) were used. An-

imals were anaesthetised (ketamin 10 mg/kg IM at induction followed by propofol 100 mcg/kg/min and ketamin 2 mg/kg/h IV) and placed under mechanical gas ventilation with: peak inspiratory pressure (PIP) 15 cmH₂O, positive end-expiratory pressure (PEEP) 5 cmH₂O, respiratory rate (RR) of 60/min, and fractional concentration of O₂ in inspired gas (FiO₂) of 30%.

A catheter was inserted into the carotid artery for blood gas and continuous blood pressure monitoring. A jugular venous access was inserted to inject the saline bolus for generating perfusion images. Each animal was shaved for placement of a custom EIT belt around the lower third of the sternum in the transverse plane.

For each animal a bolus injection protocol was used: 1.5 mL of 7.5% saline was injected into the jugular vein at a constant rate over approximately 2s. Before each bolus, ventilation was stopped for ten seconds, and a further twenty seconds of apnoea was maintained before restarting ventilation.

After one hour of ventilation (for stabilization) EIT recordings were made during the position change procedure. Each lamb was rotated onto its right side. Five minutes after turning the subject, the bolus injection protocol was implemented. The animal was then ventilated normally, remaining on the right side for an additional five minutes, before being positioned on the left side for 5 minutes of regular ventilation, followed by the bolus injection protocol.

At 2 hours of ventilation, the position change procedure was repeated, changing the positioning of the lamb from prone to supine as the bolus injection protocol was repeated and EIT recordings were captured.

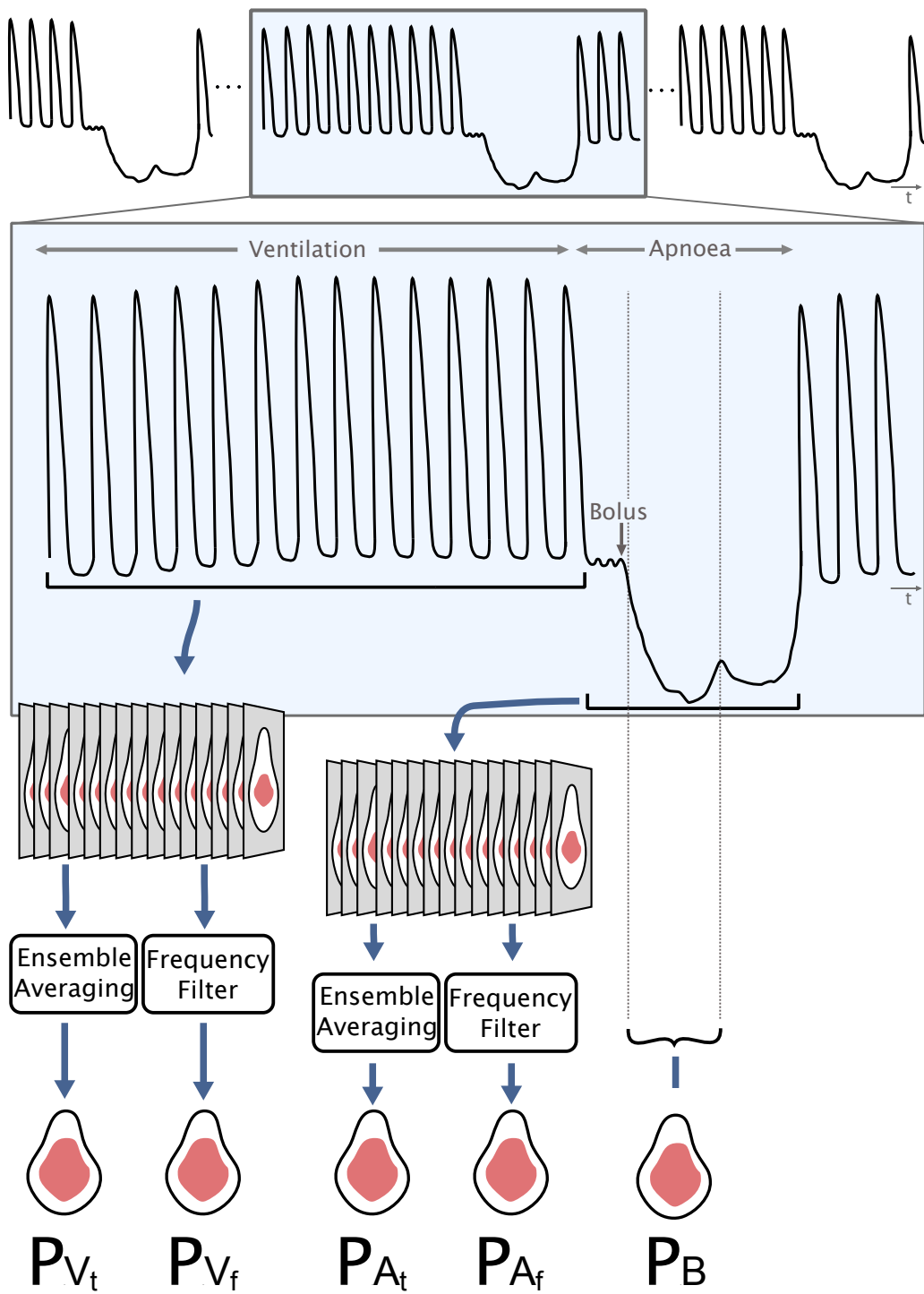


Figure 3.1: This figure is a schematic overview of analysis methods for EIT perfusion. The upper curve illustrates the global EIT signal during a period of ventilation followed by apnoea and renewed ventilation. During apnoea a bolus of conductivity contrasting saline is introduced. From these data 5 fEIT images are calculated: P_{V_t} : pulsatility (perfusion) image during ventilation, calculated by ensemble averaging EIT data during ventilation; P_{V_f} : pulsatility (perfusion) image during ventilation, calculated by frequency filtering EIT data during ventilation; P_{A_t} : pulsatility (perfusion) image during apnoea, calculated by ensemble averaging EIT data during apnoea; P_{A_f} : pulsatility (perfusion) image during apnoea, calculated by frequency filtering EIT data during apnoea; P_B : perfusion image from bolus, calculated between a reference measure during apnoea and one during the bolus

3.2.3 Data Acquisition and Image Reconstruction

EIT data was acquired with the Pioneer Set (Swisstom, Landquart, Switzerland) using a custom electrode belt (at an acquisition rate of 20 frames/s). The belt uses 32 brass electrodes equally spaced around the thorax, using an ultrasound gel to ensure good contact and minimise the contact impedance. The selected data in this study comes from lateral positioning changes recorded after 1.5 hours of ventilation and prone to supine positioning changes after 2 hours.

EIT images were reconstructed using GREIT (Adler *et al.*, 2009), which calculates a reconstruction matrix \mathbf{R} from which the reconstructed image is calculated as $\hat{\mathbf{x}} = \mathbf{R}\mathbf{y}$, where \mathbf{y} are the time-difference measurements, $\mathbf{y}(t) = \mathbf{v}(t) - \mathbf{v}(t_r)$, where $\mathbf{v}(t)$ represents the data frame acquired at time, t , and $\mathbf{v}(t_r)$ measurements acquired at a “reference” time, t_r in the case of this experiment the reference was a mean of 10 images preceding the bolus injection.

The linear reconstruction matrix $\mathbf{R} = \mathbf{D}\boldsymbol{\Sigma}_t\mathbf{J}^T(\mathbf{J}\boldsymbol{\Sigma}_t\mathbf{J} + \boldsymbol{\Sigma}_n)^{-1}$ is calculated from a finite element model of the body and electrode geometry $F(\cdot)$ and covariance estimates of the image, $\boldsymbol{\Sigma}_t$, noise, $\boldsymbol{\Sigma}_n$ (Grychtol *et al.*, 2016), and a spatial filtering matrix, \mathbf{D} .

EIT data from this experiment was prone to errors consisting of brief periods of zeroed measurements stemming from the synchronisation equipment. Measurements that were zeroed by the device were removed and replaced with linearly extrapolated data to allow for frequency-based analysis over all selected segments of data. A moving median filter with a width of 3 was used to further remove the noise caused by single measurement errors in the signal.

3.2.4 Functional EIT Images

In each animal 4 episodes were recorded — one in each posture — to generate 5 different functional EIT images.

The images Bolus-based measures of lung perfusion (P_B) were calculated using time-difference reconstructions. Heart-frequency filtering during ventilation (P_{Vf}) and apnoea (P_{Af}) used frequency analysis of EIT image sequences, as illustrated in figure 3.3, and ensemble averaging-based methods during ventilation P_{Vt} and apnoea P_{At} are calculated using ensemble averaging of identified pulsatile components figure 3.4.

The following methods were conducted on segments of data collected both during apnoea and ventilation. Apnoea regions were selected as the total time that ventilation was arrested, including the bolus section and had a duration of 30s. The ventilation data was selected as 30s of data immediately preceding the induction of apnoea. Regions of interest including lung, and heart areas in the images were defined by the lamb model provided in EIDORS (Adler *et al.*, 2017a).

3.2.4.1 Bolus injection image (P_B)

The beginning of the saline bolus injection was determined as the point immediately preceding the drop in impedance from the conductive agent, and is shown in figure 3.2 at the point marked “injection”. The mean of 10 images including and immediately preceding the bolus injection were used as the reference to which all bolus images were reconstructed from. To image perfusion, the point with maximum decline in impedance over the sum of the pixels in the lung region relative to the reference was

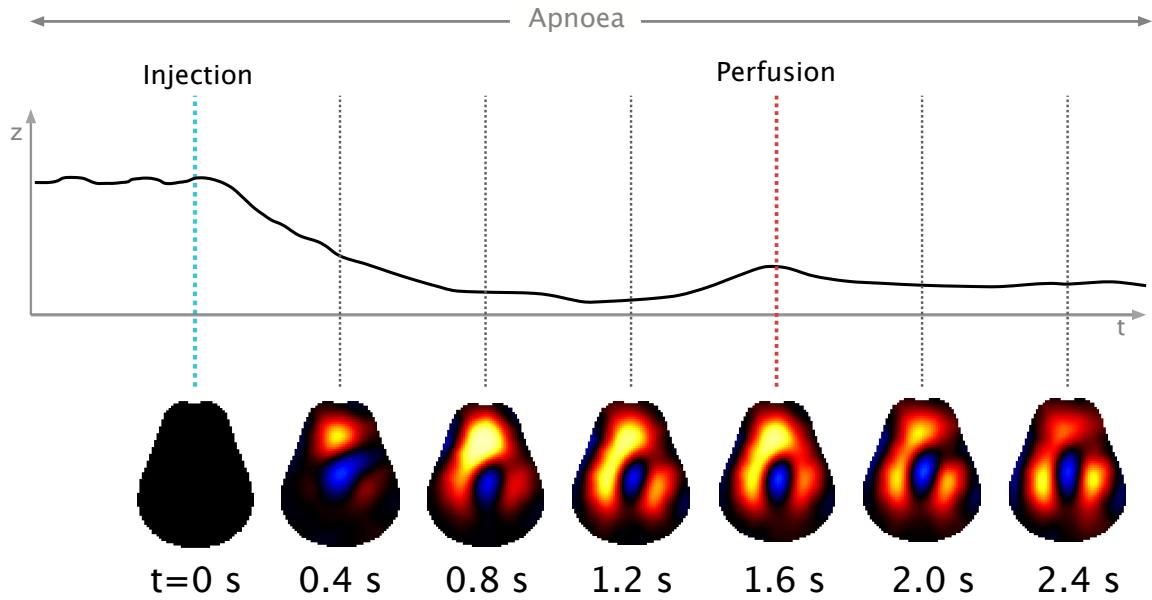


Figure 3.2: The method used to select the perfusion point from the bolus injection is shown in the figure above. The point with the widest spread of high conductivity was selected as the point of perfusion, shown here at 1.6 seconds after the contrast agent injection. The image series shows the conductivity contrast as the bolus injection travels through the thorax.

selected based on the methods presented by Frerichs *et al.* (2002). In figure 3.2 this was found at the point marked “perfusion”. This method was used as the standard perfusion measuring technique against which the other methods were compared.

3.2.4.2 Frequency-Filtering

Heart-frequency EIT images during the selected events were calculated by taking the FFT of the time-series image data after first applying a Blackman window: $w(n) = a_0 - a_1 \cos\left(\frac{2\pi n}{N-1}\right) + a_2 \cos\left(\frac{4\pi n}{N-1}\right)$ with $a_0 = 0.42$, $a_1 = 0.5$ and $a_2 = 0.08$, where N is the number of time-series EIT images in the selected event.

An FFT was calculated from a series of images restricted to pixels in the heart

region. From the FFT of all pixels the heart region, the heart frequency was selected as the largest peak between 3 and 4.5 Hz, representing a heart rate between 180 and 240 bpm (typical for a newborn lamb).

The identified heart rate was used to select changes at the heart-frequency in the frequency domain images of the entire thorax. Images at 3 frequencies on either side of the heart rate were also reconstructed to account for changes in heart rate over the course of the data collection. A Blackman window with a length of 7 was applied surrounding the heart frequency to generate a weighted mean of the images, resulting in a single perfusion image from the heart-frequency data.

The output of the frequency filtering method is an image with complex values assigned to each pixel.

Depending on the timing of the pulsatility-based changes within the selected signal the real component of frequency analysed image did not correspond to the maximum conductivity change in the lungs in every event. In order to correct this, each image was displayed along the axis that gave the maximum real component contained within the lung region to ensure the maximum change in impedance related to pulsatile activity in the lungs was calculated.

3.2.4.3 Ensemble Averaging

Time series data of the total impedance signal for each pixel in the heart region was filtered using a bandpass filter to eliminate noise and breathing changes, and allow the heartbeat to be seen clearly in the signal. Peak detection was used on this heart-region data to select the amplitude peaks in impedance change signal at the

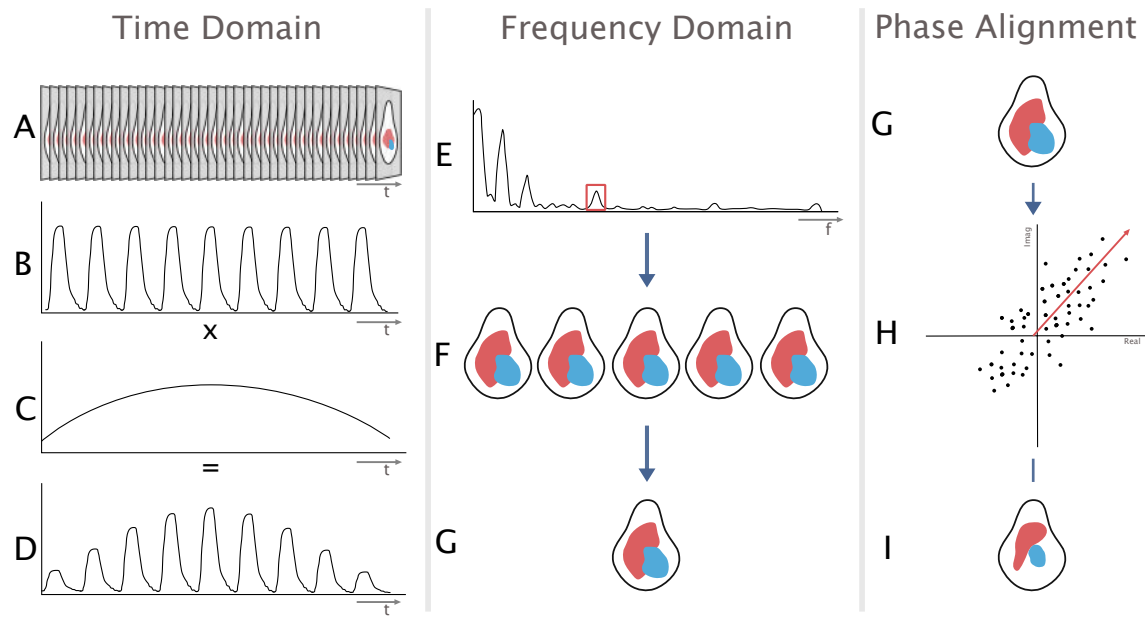


Figure 3.3: Frequency analysis methodology used for obtaining a perfusion image from the time series data. Steps are: A) to reconstruct the images from time series measurements; B) - D) window the time series data before performing a FFT on the data for each element; E) Select the dominant frequency between 3 and 4.5 Hz as the heart frequency; F) reconstruct the image at the heart frequency and selected nearby frequencies; G) take the mean of the images at the heart frequency using a Blackman window to give greater weight to those closer to the center; H) I) select the image that will give the maximum real component contained in the lung region.

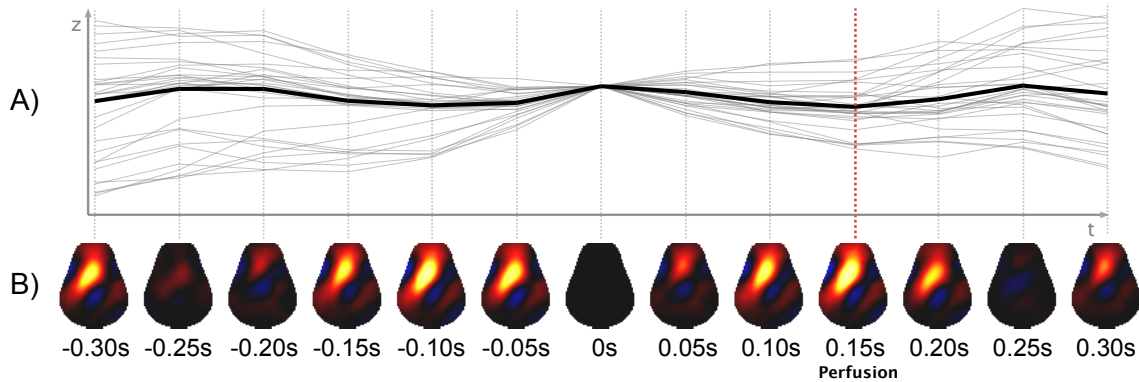


Figure 3.4: Illustration of the stages of the ensemble averaging process: A) an ensemble average of all heartbeats over the time frame is taken from the summed global signal; and B) shows reconstructed images corresponding to each time point in the global ensemble averaged signal above. The selected perfusion image is the image with the maximum impedance increase in the lung region.

heart frequency.

Using the identified time points, the global impedance change signal was ensemble averaged by overlaying all identified peaks to give an averaged heartbeat. 13 images were reconstructed over the course of the heart beat to select the image that resulted in the maximum positive increase impedance within the lung region. This process is outlined in figure 3.4.

3.2.5 Image Comparison

To compare the images the Jaccard distance between functional EIT images was calculated. Negative impedance changes were removed from the images and the images were normalized.

The Jaccard distance was calculated between the reference image calculated using the maximum increase in lung-region conductivity during bolus injection (b), and

the frequency-based method (f): $J(x, y) = \sum_i \frac{\min(b_i, f_i)}{\max(b_i, f_i)}$ representing the distance between the two images.

3.2.6 Statistical Analysis

To determine the significance of the change in bolus between postures and methods, the Cohen's d score was calculated to quantify the effect size of the change in the centre of mass of the perfusion image (Cohen, 1977). This was calculated as the difference between two means over the pooled standard deviation. Where the difference between the two means is: $\mu_1 - \mu_2$, and the pooled standard deviation is:

$$\sqrt{\frac{(n_1-1)s_1^2 + (n_2-1)s_2^2}{n_1+n_2-2}}.$$

3.3 Results

The Jaccard scores for each method were compared between ensemble averaging and frequency filtering methods to determine the regions where performance was best for each method. Figure 3.5 shows a comparison between Jaccard distance for each animal, connecting lines indicate different methods performed on the same data segment, while each marker shape denotes a separate posture.

On average frequency filtering outperforms ensemble averaging based methods of perfusion calculation ($p=0.04$), and there is no significant difference in performance of the heart-frequency based filtering techniques during periods of apnoea relative to periods of ventilation.

Of the 56 data regions that were analysed, the ensemble averaging performed bet-

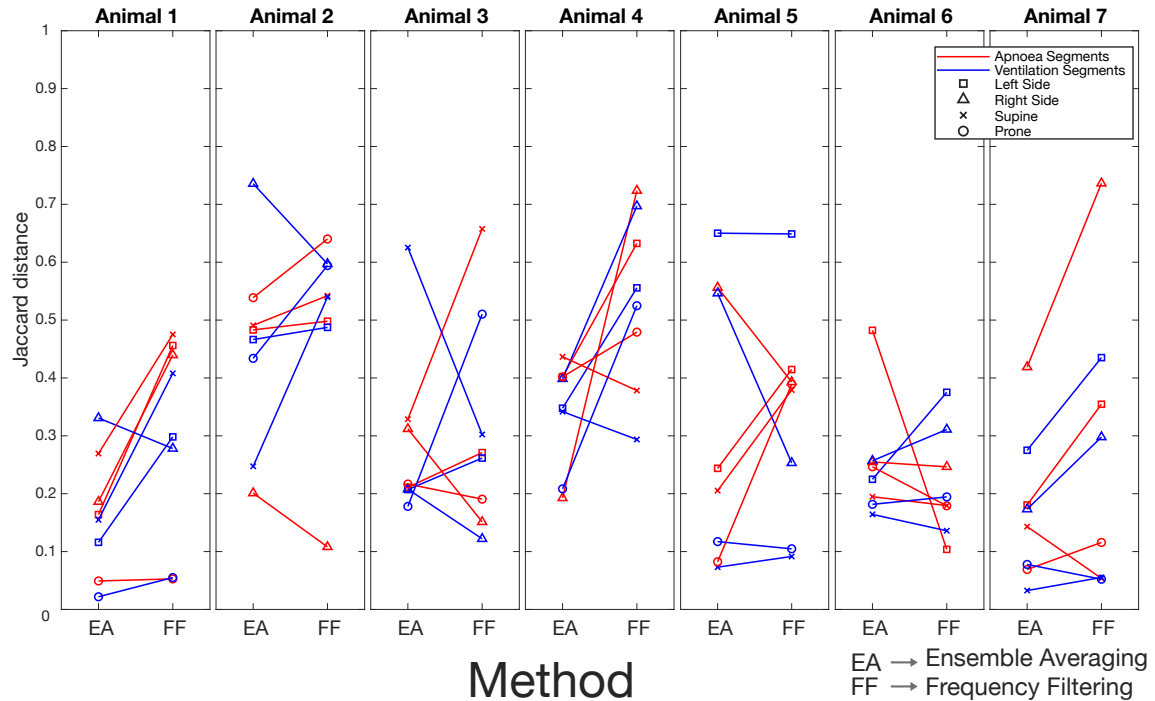


Figure 3.5: Jaccard scores for each method and animal in the comparison. Frequency filtering and ensemble averaging methods performed on the same data segment are connected by solid lines. Red lines and markers indicate apnoea data sections, while blue indicates ventilation data sections. Each posture is denoted by a different shaped marker in the figure.

ter in 12 cases and the frequency filtering achieved the best performance in 28 cases, there, were 16 additional cases where the difference in performance was negligible at less than 5%. On average, across all images, frequency filtering based methods scored 7% higher than ensemble averaging.

The center of mass of the perfusion measure images using the bolus injection method had a Cohen's d score of less than 0.1 between posture changes indicating that there is an insignificant or trivial difference in the means relative to the standard deviation (Cohen, 1977). To demonstrate the visually observable changes due to posture change and the high similarities that can be observed between filtering- and bolus-based perfusion estimates, frequency filtered images from animal 4 are compared to bolus based methods in figure 3.6.

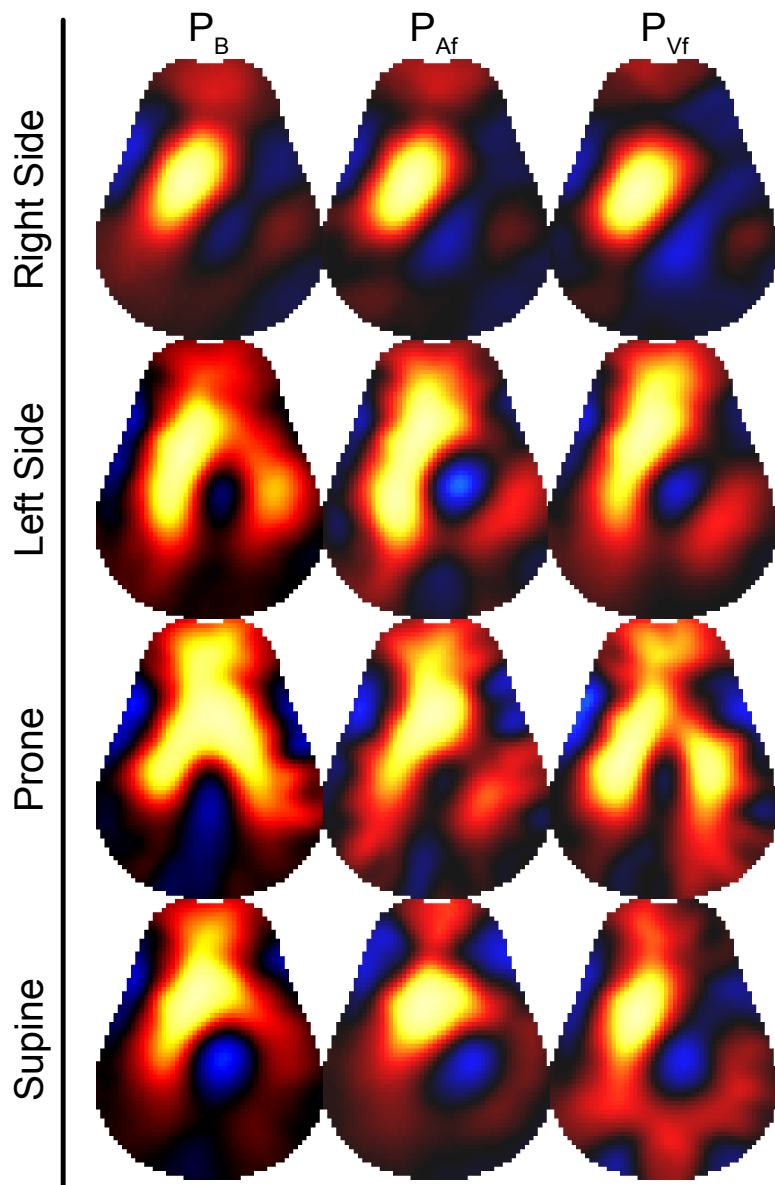


Figure 3.6: This figure shows the tracking of perfusion for frequency filtering measures of perfusion during apnoea and ventilation sections compared to bolus injection for animal 4. P_B is the bolus injection image, P_{Af} uses the frequency filtering method during apnoea and P_{Vf} is the frequency filtering method during ventilation.

3.4 Discussion

Two primary approaches of EIT perfusion calculation have been compared in this paper: injection of a bolus of contrast-agent resulting in EIT image changes which produce perfusion measures, and digital filtering of EIT image sequences to extract the heart-frequency components. Additionally, various algorithms have been evaluated for digital filtering-base approaches during mechanical ventilation and short apnoea sequences, using both frequency- and ensemble averaging-based techniques. There have been few comparisons of these techniques, and we set out to better understand the relationship between perfusion and heart-frequency measures, and between the various filtering approaches used to determine heart-frequency cardiac changes. We selected an experimental protocol using posture-change to alter the regional distribution of lung ventilation and perfusion in newborn lambs.

Our first question was “to what extent do heart-frequency filtering-based measures correspond to perfusion?”

The primary results (figure 3.5) use a Jaccard index of the similarity between functional images. Overall it was found that in healthy animals the Jaccard index indicated good agreement with our gold standard. While highly dependant on the data, it was found that there was a high degree of similarity between methods with respect to the overall shape of the perfusion. In both animals 2 and 4, where the signal required little preprocessing before analysis there is a higher Jaccard score across all cases.

The synchronisation box was attached to the EIT system but was not used for this experiment, an error in the connection caused brief periods of the signal (less

than 1 s) in some animals to be zeroed. Through careful processing of this signal only brief sections of data were lost and we do not feel this impacts the results.

During the experiment the order of posture change was not randomised. While changes in ventilation due to posture change are not understood to have long term physiological effects, if there is a longer term effect of change in posture the lack of randomisation will impact the results. Nguyen *et al.* (2015) were able to image perfusion changes due to induced pulmonary embolisms and using the peak impedance change on dilution curves, however our data presented insufficient variance in perfusion induced by posture change to complete a center of mass analysis. A higher statistical power could potentially be achieved through initiating posture changes with more dramatic results in perfusion, such as upright to supine (Nakazato *et al.*, 2010).

Throughout the experiment, the perfusion image was selected as the image containing the largest increase in conductivity in the sum of pixels in the lung region, which occurred at different relative times across animals and events. Many factors could affect this including belt positioning changes, and it could be a contributing factor to the inconsistent trends in amplitude changes in the global image across methods. Borges *et al.* (2012) compared EIT perfusion images using first-pass kinetics and heart-frequency filtering based methods to perfusion measures using SPECT, finding that heart-frequency filtering techniques made systemic errors when used to estimate the perfusion. They also determined that there was no discernible relationship between the magnitude of the SPECT images and the heart-frequency images. This was consistent with the findings of this study that image amplitude

of the bolus injection and heart-frequency filtering-based methods was not consistent in all animals. This methodology presented by Borges *et al.* (2012) was not part of the comparison in this study as the edentification of the perfusion signal due to the heart could not be consistently identified and removed across all animals. In two dimensions, heart-frequency and ventilation signals have been used to identify the location of the heart and lungs within the EIT electrode plane with known electrode locations and anatomy (Ferrario *et al.*, 2012), but in situations where the electrode location and anatomy is not precisely known EIT tends to perform poorly as a structural imaging modality (Adler and Boyle, 2017). These challenges suggest that configurations with multiple planes of electrodes may be better able to isolate and remove off-plane pulsatility signals related to the heart.

It was observed that the general shape of the perfusion was consistent across all methods despite amplitude variations. One reason for the difference in amplitude change across animals may be due to slight variations in the belt placement and electrode positioning on the animals. If the belt is closer to the heart, there will be a larger heart-frequency component to the signal and there may be a variance in the impedance change due to bolus injection.

Next, we asked “what are the advantages and disadvantages of different approaches to heart-frequency filtering of EIT data, and which techniques are recommended under which circumstances?”

Our overall recommendation is that, whenever possible, frequency filtering techniques should be used. This is largely because frequency filtering methods tend to be more stable in the presence of noise on the signal. Ensemble techniques are

advantageous in some circumstances, because they better use the heart-frequency variability to avoid interference from harmonics of the ventilation at the heart rate. For frequency-filtering techniques, it is necessary to widen the heart-frequency filters to account for such variability. On the other hand, it is sometimes not possible to accurately synchronize heartbeats, due to noise corruption in the signals or the very low amplitude of the heart-frequency signals relative to the ventilation signal. In cases where the signal of the heartbeat was not clearly identifiable through visual inspection of the signal, neither ensemble averaging nor frequency filtering was able to achieve good estimates of perfusion relative to the bolus injection event.

In summary, our goal was to understand the relationship between bolus- and filtering-based EIT measurements of lung perfusion, as well as the relationship between different filtering-based measures of perfusion. Our results indicate there is a common trend between the shape and perfusion estimates of both heart-frequency and bolus injection images despite the difference in physiological events behind each measure. Amongst filtering techniques, frequency filtering outperforms ensemble averaging across regions of data where there is noise present and the heart signal cannot be readily identified, and both methods were able to approximate the bolus injection measures equally well when applied to apnoea and ventilation regions of data.

3.5 Summary

Two main functional imaging approaches have been used to measure regional lung perfusion using Electrical Impedance Tomography (EIT): venous injection of a hy-

pertonic saline contrast agent and imaging of its passage through the heart and lungs, and digital filtering of heart-frequency impedance changes over sequences of EIT images. This paper systematically compares filtering-based perfusion estimates and bolus injection methods to determine to which degree they are related. EIT data was recorded on 7 mechanically ventilated newborn lambs in which ventilation distribution was varied through changes in posture between prone, supine, left- and right-lateral positions. Perfusion images were calculated using frequency filtering and ensemble averaging during both ventilation and apnoea time segments for each posture to compare against contrast agent-based methods using Jaccard distance score. Using bolus-based EIT measures of lung perfusion as the reference frequency filtering techniques performed better than ensemble averaging and both techniques performed equally well across apnoea and ventilation data segments. Our results indicate the potential for use of filtering-based EIT measures of heart-frequency activity as a non-invasive proxy for contrast agent injection-based measures of lung perfusion.

Chapter 4

FEM mesh refinement for 3D EIT

4.1 Motivation

This thesis proposes the use of novel 3D electrode configurations and internal electrodes to improve sensitivity to cardiosynchronous activity. Unlike surface electrode configurations, these models will have a very high sensitivity in the center of a model where mesh refinement can be challenging. In this chapter we explore the need for mesh refinement with regard to sensitivity accuracy.

4.2 Introduction

Electrical Impedance Tomography (EIT) reconstructs images of electrical tissue properties within a body from electrical transfer impedance measurements at surface electrodes. For biomedical imaging applications, it is being actively studied for monitoring the movement of air and blood in the thorax, and for imaging the head and

breast. Reconstruction of EIT images requires the solution of an inverse problem in soft field tomography. EIT image reconstruction requires calculation of a sensitivity matrix, \mathbf{J} , representing the relationship between internal changes and measurements. A pseudo-inverse of \mathbf{J} is used to update the image estimate over several iterations. EIT image reconstruction is ill-posed, since the physics of current propagation implies that sensitivity is largest near the electrodes and smallest in the body centre.

It is therefore clear that a precise calculation of \mathbf{J} is required for solution accuracy. Since it is generally not possible to use analytic solutions, because of the non-regular shapes of biological bodies and the boundary conditions on a conductive electrode, the finite element method (FEM) is typically used. One key advantage of the FEM is that element size can be selectively refined in regions to meet solution accuracy. The accuracy of the FEM solution will increase as more elements are added, so a high mesh density is often desired to achieve an accurate solution. In this paper we will use the term mesh to refer to a specific combination of nodes and elements in a finite element model. In EIT the sensitivity is nonuniform across the entire model. Thus it has generally been recommended in the EIT literature that meshes be refined near electrodes, where the electric field and sensitivity are largest (Adler and Boyle, 2017). This recommendation gives rise to two questions: 1) No thorough analysis has been made to determine how much refinement is required. Given a “mesh element budget”, what should balance of nodes be between the centre of the model and the electrodes? And 2) How do different freely available meshing tools that are commonly used with EIT compare when used to refine 3D meshes?

Previously with EIT, mesh refinement has primarily been either constant, or

based on the complexity of geometric surfaces and lines within a model (Grychtol and Adler, 2013). In EIDORS (Adler and Lionheart, 2006) meshes are generated using both Netgen (Schöberl, 1997) and Gmsh (Geuzaine and Remacle, 2009) for 2D and 3D models. Refinement around electrodes is commonly performed by setting a mesh density for the electrodes and allowing the mesh density to decay towards the maximum mesh size. This does not allow the user to specify the rate of decay or precisely control the mesh size.

A model that accurately represents the anatomy of the imaged region can greatly increase the quality of the reconstructed image (Grychtol *et al.*, 2012), but increasing the complexity of mesh surfaces presents additional challenges for mesh refinement. EIT reconstruction software EIDORS enables users to place electrodes on the surface of complex boundaries (Grychtol and Adler, 2013), but the current functionality does not enable control of the refinement around the electrodes or internal structures. Most commercially available FEM packages do not conveniently provide such capability either.

In this paper we investigate approaches to manage the tradeoff between refinement of the electrode regions versus the bulk volume. We present a comparison between Gmsh and Netgen based mesh refinement around electrodes, and evaluate the effect of mesh refinement techniques on error in the sensitivity matrix, \mathbf{J} .

4.3 METHODS

4.3.1 Overview

We built a cylindrical model in Gmsh and Netgen which was parameterized so that multiple different combinations of mesh refinement were possible. These results were compared to a very high density meshes which was considered the gold standard. The format of the geometry files used to generate these meshes can be seen in appendix A.

4.3.2 Mesh Generation

A cylinder ($\varnothing = 0.5$ m, height $h = 0.25$ m) with four square electrodes (5 cm edge length) placed equidistantly around the perimeter at mid-height was meshed with Netgen (version 5.3.1) (Schöberl, 1997) and Gmsh (version 4.7.0) (Geuzaine and Remacle, 2009) meshing software. Current was injected between adjacent electrodes and the voltage was measured between the remaining two electrodes. For 3D meshes an initial analysis was done building on work from Grychtol and Adler (Grychtol and Adler, 2013) where mesh density was set by specifying the maximum edge lengths permitted on electrode surfaces and in the volume of the FEM. Results were compared against those generated using ultra-fine meshes. Calculations were performed with EIDORS (version 3.10) (Adler and Lionheart, 2006) in Matlab 2019b (The Mathworks, Natick, MA, USA).

Meshes of different sizes were generated with Netgen and Gmsh by manipulating the desired maximum edge length (maxh parameter) for the entire domain and the electrodes. Two mesh analyses were performed. For the first mesh, maximum ele-

ment lengths were chosen such as to divide the electrode side of 5 cm into an integer number of segments of equal size. The maximum mesh element length ranged from 1 to 7 subdivisions of the electrode edge, while the maximum mesh element length in the ultra-fine reference mesh was 15 subdivisions per electrode edge. Independent reference meshes were generated for each software. Two types of models were generated this way. Constant models C1–C7, where the mesh size was constant, and refined models R1–R7 where the electrode mesh size was specified and dissipated towards an internal mesh element size of 5 cm. Additional refined meshes were generated with reduced mesh size in the internal mesh regions. R1-R7 is referred to as refinement A where the internal element max size was 5 cm. Refinement B had an internal mesh size of 4 cm, C was 3 cm and D was 2 cm. The numeric value in the mesh ID indicated the number of subdivisions per electrode edge. In Netgen the mesh decay was not easily controlled beyond selecting a refinement level from 1 to 5, but in Gmsh the size was set to increase evenly from the surface of the electrode to the centre of the model. It should be possible to replicate this mesh density distribution in Netgen by using a separate mesh density file that specifies the required density at each point in the geometry, but this technique is not widely used due to its complexity. Figure 4.1 shows example meshes of coarse, fine and refined meshes. Figure 4.2 shows the generated mesh structure for constant refinement meshes around the electrode for both Netgen and Gmsh.

For the second analysis, the distribution of nodes within the model was changed without altering the total number of nodes to give M1 – M17. Starting with the constant mesh C3 as M1, the maximum mesh element length on the electrode was

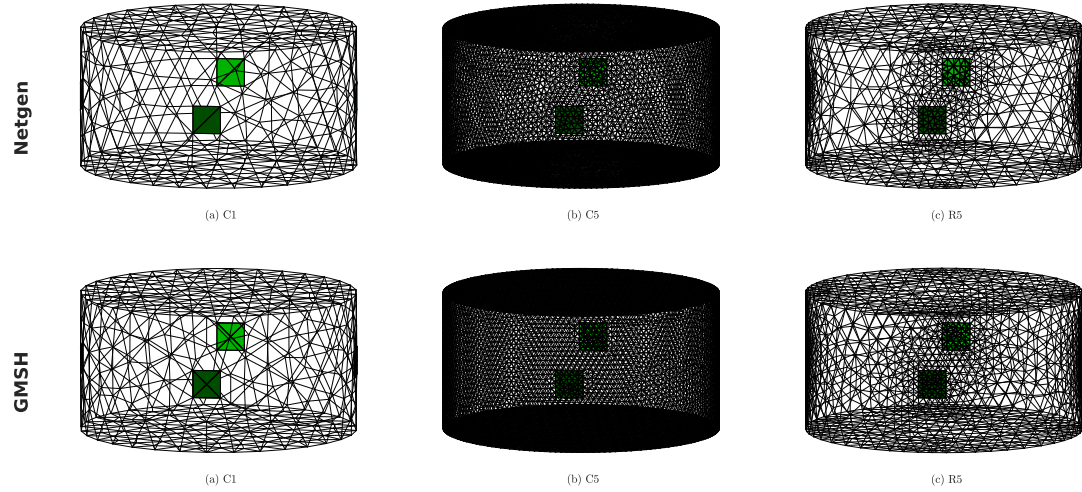


Figure 4.1: Sample meshes generated with Netgen (top row) and Gmsh (bottom row). From left to right: (C1) the coarsest constant mesh; (C5) a refined constant mesh; and (R5) a refined mesh with the same electrode mesh density as C5 but lower internal mesh density.

decreased by 10% and the maximum mesh size in the centre was increased so that the total number of elements in the mesh was within 10% of the original mesh. C3 was chosen as the starting point because several steps of mesh refinement could be generated before the electrode mesh density surpassed the reference meshes. For mesh M17 the specified electrode refinement was equal to the reference mesh. In Netgen the mesh dissipation rate was not further controlled, and in Gmsh the mesh density decreased evenly from the electrode surface to the centre of the model. To compare these meshes a section of the model was selected encompassing all points between the centre of the model and a selected electrode face. The average distance, or balance point, along the x-axis of the selected points was expressed as a percentage of the tank radius. This process is illustrated in figure 4.3.

When generating meshes to compare across several mesh density profiles as the

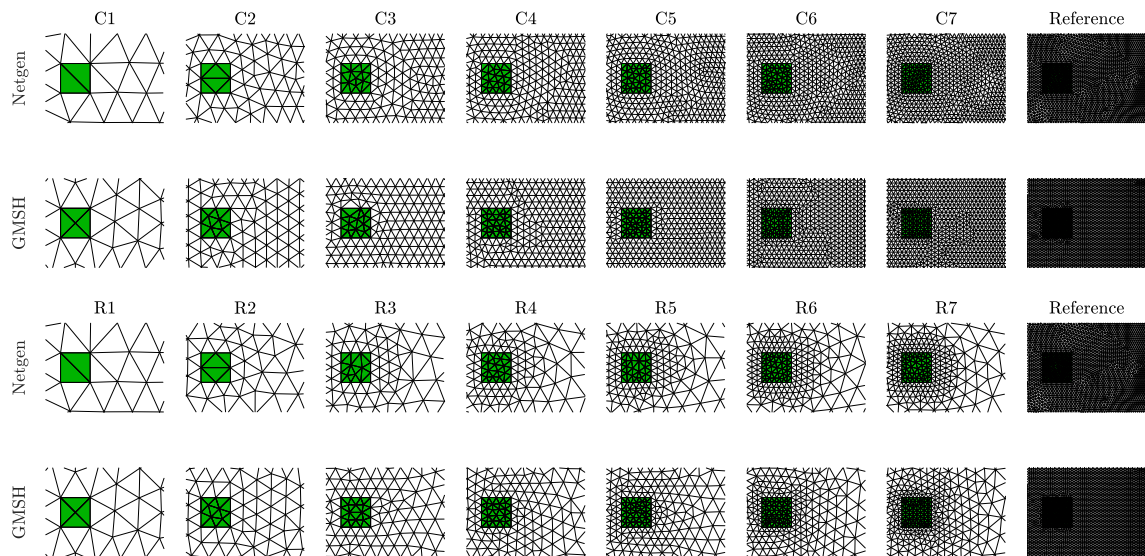


Figure 4.2: A view of the electrode meshing for all constant-density meshes in Netgen and Gmsh. The top two rows show all electrode faces and immediate surroundings from coarsest (C1) to finest (C7). C represents the constant mesh refinement and the number represents the specified mesh subdivisions per electrode edge. The reference mesh is equivalent to C15. The bottom two rows show refined meshes R1 to R7 with both Netgen and Gmsh and shows the rate of mesh dissipation away from the electrodes.

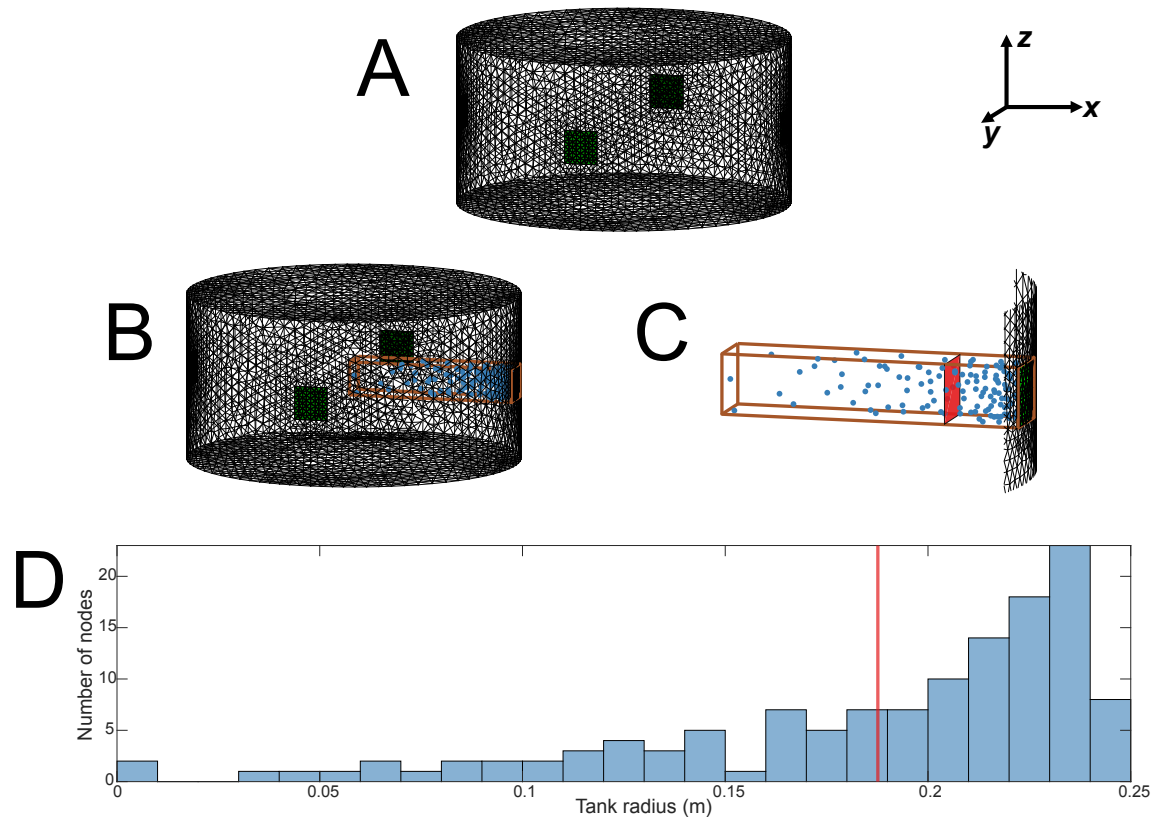


Figure 4.3: A sketch of the process to determine the balance point of generated meshes. A) the starting mesh; B) nodes between the electrode surface and the centre of the model are identified; C) the balance point of the nodes along the x-axis is calculated and indicated by the red plane; D) a histogram showing an example distribution and balance point (red) for the selected model.

balance of the nodes was shifted towards the electrodes, 19 meshes were generated for each software including 2 reference meshes. table 4.1 shows the parameters of the resulting odd numbered meshes.

4.3.3 Simulation

The potential at each node \mathbf{V} of the mesh was calculated using the finite element method (FEM) using the linearization

$$\mathbf{V} = \mathbf{Y}^{-1} \mathbf{C} \quad (4.1)$$

where \mathbf{Y} is the admittance matrix of the FEM (and a function of conductivity distribution) and \mathbf{C} is a matrix representing the current injection pattern, such that \mathbf{C}_{ij} represents the current injected in electrode i during the j -th stimulation. Here, we drive current of 1 A between two adjacent electrodes in a single stimulation, so $\mathbf{C} = [0|0|1|-1]^T$. We pick a node in the centre of the FEM as ground, since it is necessary to assume the potential on one node for \mathbf{Y} to be invertible. We use the complete electrode model and assume contact impedance of 0.01 Ω in the calculation of the admittance matrix (Polydorides and McCann, 2002).

We calculate the sensitivity (or Jacobian) matrix \mathbf{J} of measurements \mathbf{v} to changes in the conductivity σ of individual elements as $\mathbf{J}_{ij} = \frac{\partial v_j}{\partial \sigma_i}$ using the adjoint method (Polydorides and McCann, 2002). Again, since we only have one measurement, \mathbf{J} is in fact a vector. We construct a sensitivity image by assigning each element i of the FEM the value of \mathbf{J}_i divided by the element's volume. Mean sensitivity in

Table 4.1: Mesh parameters for odd numbered meshes generated by Netgen (A) and Gmsh (B) to determine the optimal node balance. Parameters global maxh and electrode maxh refer to the specified input parameters; the remaining columns give parameters from the resulting meshes.

Mesh ID		lbl.	elec.	# elem.	# nodes	# elec. elem.	minEL ^a [mm]	maxEL ^b [mm]	minEV ^c [mm ³]	maxEV ^d [mm ³]
M-01	A	16.67	16.67	31347	7095	22	9.80	49.45	254.76	6851.01
	B	16.67	16.67	49210	9615	25	10.32	50.00	222.87	2898.59
M-03	A	18.33	15.00	29639	6482	22	10.75	50.41	289.80	5826.14
	B	18.33	15.00	49247	9680	40	7.36	37.11	172.78	2814.55
M-05	A	18.33	13.33	29814	6589	28	9.39	49.91	162.26	5648.41
	B	20.00	13.33	50749	9930	42	7.80	37.93	134.41	3233.59
M-07	A	18.33	11.67	30581	6723	36	8.77	47.88	141.74	6252.36
	B	21.67	11.67	53002	10429	60	6.17	40.84	63.22	4077.18
M-09	A	18.33	10.00	30690	6755	42	7.86	49.18	115.45	5496.39
	B	23.33	10.00	56237	11008	68	5.82	43.81	62.88	4962.89
M-11	A	18.33	8.33	31575	7030	74	6.05	50.99	60.06	6086.88
	B	26.67	8.33	55545	10886	96	5.51	49.72	36.84	7424.70
M-13	A	20.00	6.67	28589	6447	92	4.65	51.85	20.68	6664.11
	B	30.83	6.67	54993	10825	148	4.51	55.36	20.63	10453.90
M-15	A	21.67	5.00	27775	6245	158	3.46	52.60	11.13	9097.30
	B	36.67	5.00	55331	11000	250	3.51	61.66	7.99	15838.09
M-17	A	30.00	3.33	39116	7590	320	1.75	72.83	1.13	23783.17
	B	48.33	3.33	52947	10798	548	2.32	86.60	2.72	32287.34
REF	A	3.33	3.33	6661789	1173243	510	1.75	9.49	1.01	46.09
	B	3.33	3.33	5871464	976558	554	2.10	7.59	1.58	21.65

a: minimum mesh edge length, *b*: maximum mesh edge length

c: minimum mesh element volume, *d*: maximum mesh element volume

the plane of electrodes is then calculated by averaging the sensitivity in fifteen planes parallel to the plane of electrodes and spanning the height of 5 cm. The sensitivity was projected onto a 512×512 array and divided into regions of interest for the centre (C), at the electrode (E) and between the centre and electrode (I). The resulting sensitivity for the reference mesh calculated with Gmsh and the selected regions of interest is presented in figure 4.5.

The sensitivity error is the absolute difference in total sensitivity for the selected region with reference to the ultra-fine model.

4.3.4 Electrode refinement for arbitrary FEMs

Our approach for refinement around electrodes in Gmsh with external electrodes also allows for the refinement of arbitrary models with complex structures such as internal electrodes and tissue boundaries. A scenario depicting an approximation of a probe entering a bone with different layers of conductivity. The resulting mesh pictured in figure 4.7 highlights the ability of this technique to be used for refinement around electrodes and the control of mesh density surrounding internal structures which was previously very challenging in EIT software.

4.4 Results

Two analyses of mesh refinement were completed. The first comparing sensitivity error between meshes with constant refinement and refinement only at the electrodes, and the second comparing meshes with different levels of electrode refinement and

the same number of nodes.

When comparing constant meshes to meshes with refinement at the electrodes, sensitivity error was decreased as more nodes were added to the mesh and to the electrodes. The sensitivity error was lowest in the constant meshes across both Netgen and Gmsh software. Meshes generated using Netgen provided a slightly lower sensitivity error relative to the respective reference mesh compared to Gmsh, and resulted in meshes with fewer nodes per electrode given the same input parameters. figure 4.4 shows the sensitivity error between constant and refined meshes with respect to the number of nodes per electrode.

Example sensitivity profiles for the M-series meshes are shown in figure 4.5. The resulting sensitivity profile near the electrodes more closely matched the reference case when refinement at the electrodes was higher.

The total sensitivity error across all meshes is plotted vs. the balance point in figure 4.6. For meshes generated with Gmsh the minimum error was achieved when the node balance point was approximately 85% of the model radius corresponding to model M15-B, and for Netgen generated meshes the minimum sensitivity was achieved in model M13-A at a balance point of approximately 70%. Gmsh achieved a lower sensitivity error measured against the respective reference mesh. For meshes using Netgen refinement, the balance point did not increase evenly as the electrode density was increased and the internal density decreased. To maintain the same number of nodes within the model, Gmsh required a larger internal maxh than Netgen. Gmsh generated meshes with more nodes for the same input parameters, but generally the resulting mesh sizes were closer to those specified. The resulting

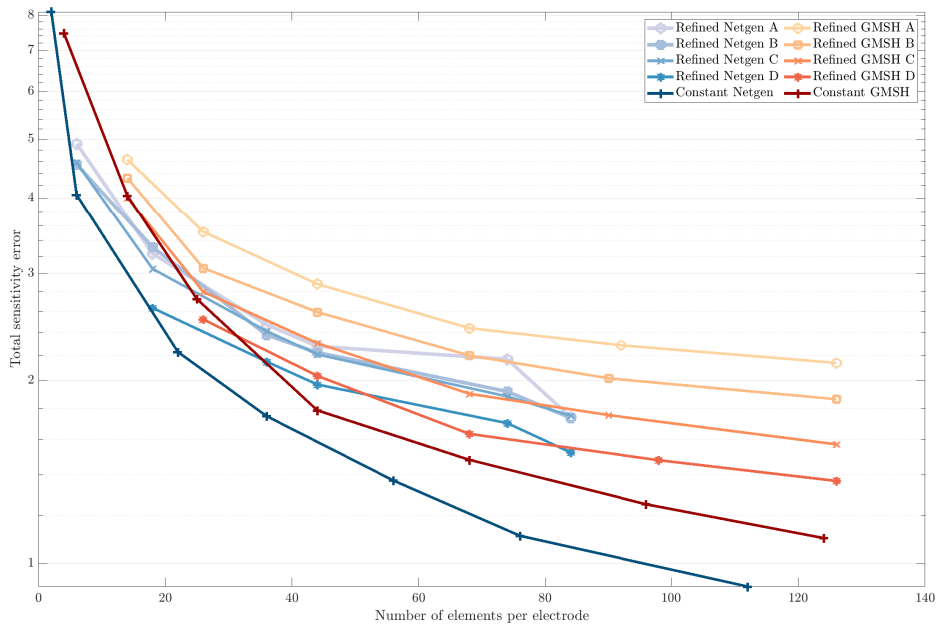


Figure 4.4: Sensitivity error of each mesh as a function of the number of elements per electrode for both Netgen and Gmsh. The darkest lines indicate the constant mesh refinement, lighter lines indicate a larger maximum internal mesh size. The maximum internal mesh sizes are as follows: refinement A - 5 cm; refinement B - 4 cm; refinement C - 3 cm; refinement D - 2 cm.

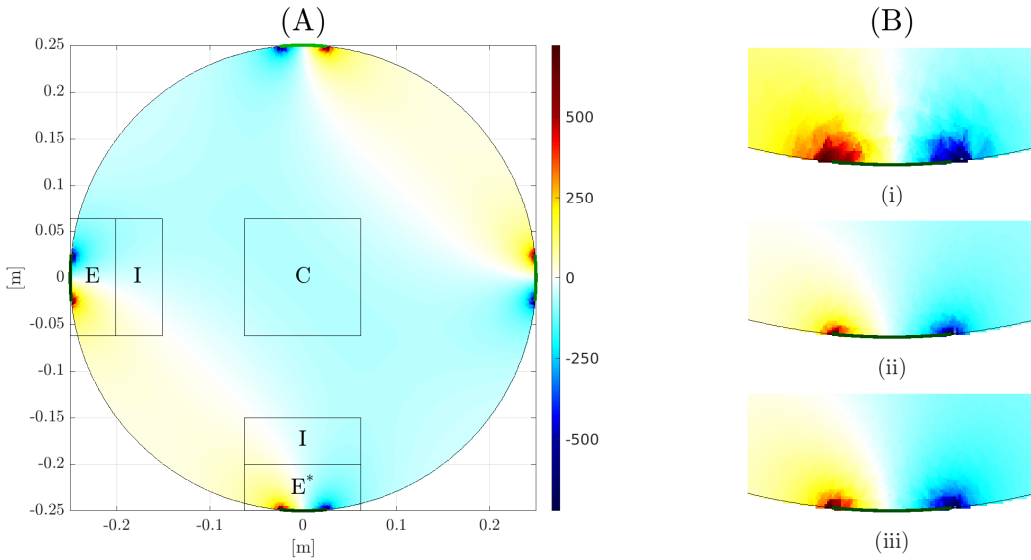


Figure 4.5: (A) Sensitivity distribution for the reference mesh (C15) generated in Gmsh with regions of interest used to compare between models. (B) 3 sensitivity distributions in region E^* next to the electrodes: (i) Constant mesh M1 (ii) refined mesh M15 with a balance point of 82% (iii) reference mesh from (A).

mesh parameters for odd numbered meshes can be seen in table 4.1. Across all meshes the measurement error when computing the voltage measurements was insignificant at less than 0.2%.

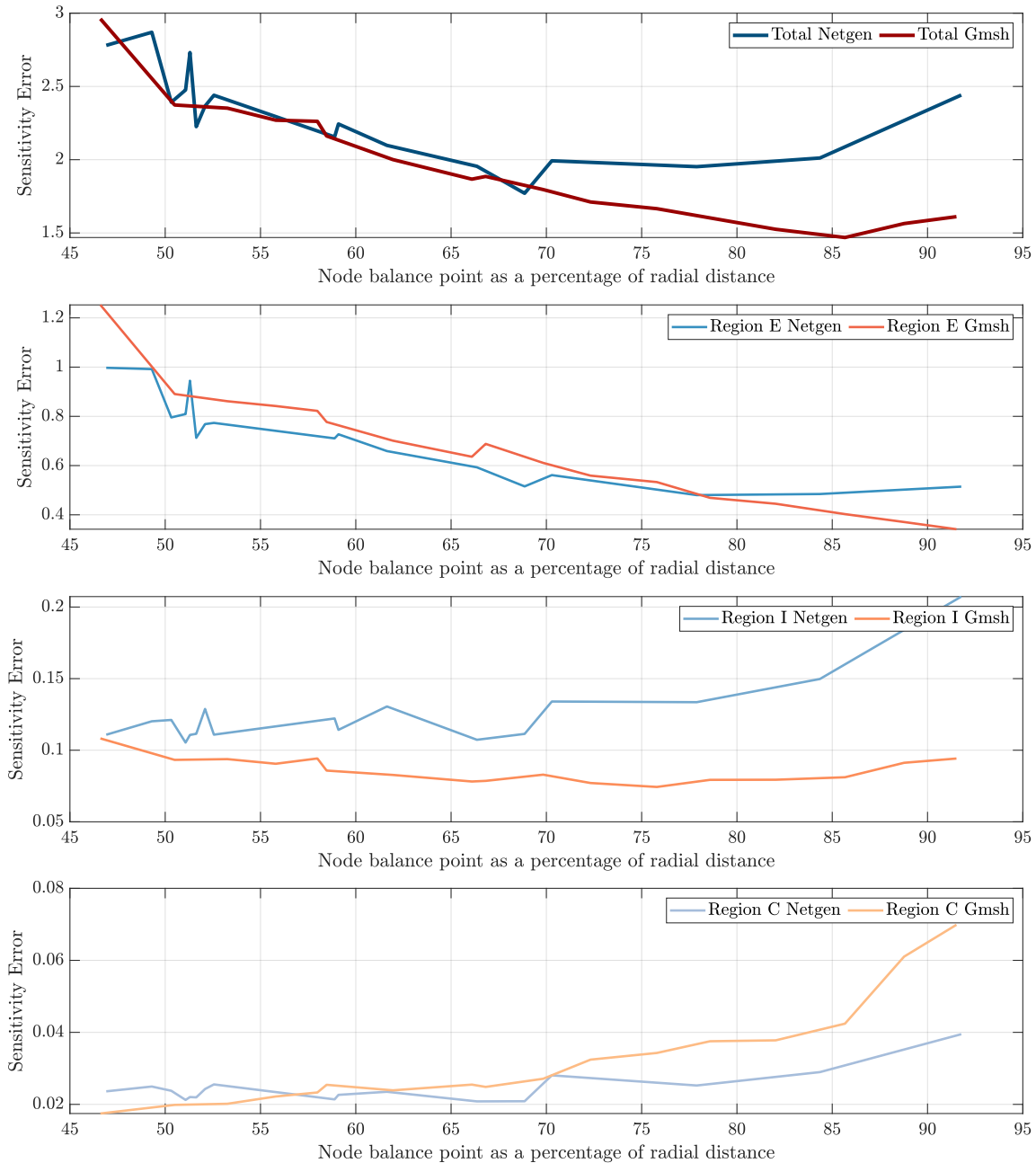


Figure 4.6: Resulting sensitivity error for Netgen (blue) and Gmsh (red) as the balance of the nodes was shifted towards the electrodes. From top to bottom: total sensitivity error, the sum of sensitivity error in region E, the sum of sensitivity error in region I and the sum of sensitivity error in region C. The regions are described in figure 4.5.

4.5 Discussion

We consider several questions on the requirement of FEM refinement in the neighbourhood of electrodes and the available tools for mesh refinement in EIT. 1) Given a “FEM element budget”, what should balance of nodes be between the centre of the model and the electrodes? 2) How do different freely available meshing tools that are commonly used with EIT compare when used to refine 3D meshes?

While refining meshes surrounding the electrodes is agreed to be useful, there is a lack of systematic analysis of the required refinement level, and controlling such refinement is difficult. Automatic mesh refinement is an area of active work and there are a number of commercial and free products available. We compare two programs used widely in EIT. Our results show that Netgen and Gmsh control mesh refinement differently and the same input parameters result in meshes with different numbers of nodes. figure 4.2, depicts the difference in mesh dissipation rates between Netgen and Gmsh. The mesh size in Gmsh increased gradually from the surface of the electrode towards the centre of the model, where the mesh size in Netgen increased much more quickly from the edges of the electrode. While we attempted to control the dissipation rate in Netgen by manipulating the mesh density in the centre of the model, we were unable to achieve a smooth transition between the electrode and internal regions of the mesh.

To analyze the benefit of electrode refinement and the difference between Netgen and Gmsh refinement techniques we consider a sequence of refined meshes compared to a “gold standard”, uniformly fine FEM solution. The models were refined either globally or in the electrode neighbourhood, and the error in the sensitivity matrix

\mathbf{J} was compared. figure 4.4 displays the difference in sensitivity between constant meshes and meshes with refinement at the electrodes. The sensitivity error was lower in Netgen across all constant refinement meshes, in part because there were more total nodes than Gmsh meshes with the same number of nodes on the electrode. Refinement around the electrode decreased the total sensitivity error, but still had larger error than meshes with constant refinement due to the smaller number of nodes in the model.

Using the balance point analysis, we were able to determine the optimal distribution of nodes to minimize sensitivity in both Gmsh and Netgen. The minimum total sensitivity from figure 4.6 was approximately 70% for Netgen. This was mainly due to the rapid dissipation of node density away from the electrodes. Increasing the refinement near the electrode reduced error in region E, but in region I there were insufficient nodes to reduce the sensitivity error. As the balance of refinement approached 90% the error in region E also started to increase as the node density did not remain fine throughout the entire region. This effect can also be seen in figure 4.2. In Gmsh the optimal balance for refinement was at approximately 85% of the radial distance. Since mesh density was set to reduce evenly between the electrode surface and the centre of the model, there was a higher density of nodes that was maintained in regions E and I as the electrode refinement increased. The error in the centre of the model was higher in Gmsh meshes, but since this is where the sensitivity is lowest the total sensitivity error was much lower.

The ability to selectively control the mesh refinement in regions in Gmsh also allows users to generate complex meshes and control mesh density surrounding internal

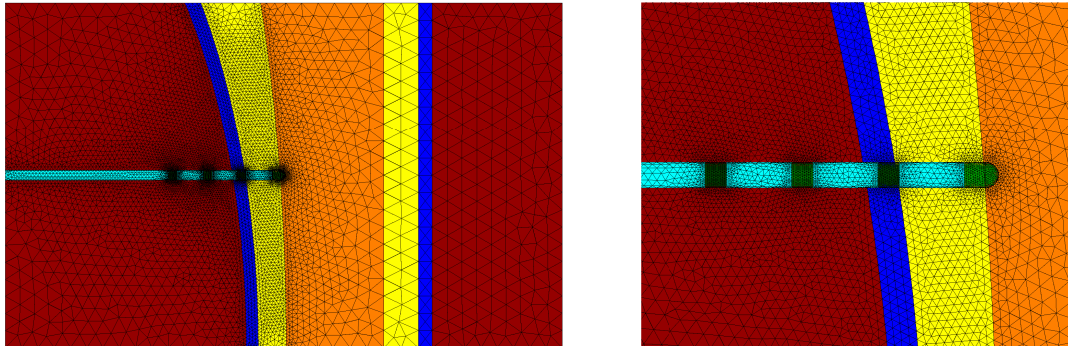


Figure 4.7: Example FEMs of a probe entering a bone from the surrounding tissue. Refinement is specified around the electrodes and tissue interfaces near the probe.

structures and electrodes an example mesh is shown in figure 4.7 where a model was created of a probe entering a bone from the surrounding tissue. These additions fill an important need in EIT to allow for more accurate models of regions surrounding internal structures and electrodes, and

Despite the increased ability to control refinement, the results still show that there are discrepancies between the specified parameters and the resulting meshes. The data in table 4.1 show that the maximum element lengths specified for each mesh were different from the actual maximum edge lengths. As the node density was increased near the electrodes, in Netgen the balance point did not always shift towards the electrode as the maximum node density was not always higher despite specifying a smaller mesh size. In Gmsh the mesh density was closer to the specified values, typically resulting in more nodes in the refined meshes.

Across both analyses errors away from the refined areas may be higher, but the ability to refine meshes selectively near regions where high sensitivity is required may allow for reduced measurement error while still allowing for quicker meshing

times. As more electrodes are added and the model complexity is increased, we expect that refinement around the electrodes will continue to reduce total sensitivity error. However the node balance analysis will not be possible for irregularly shaped models. The node balance analysis provides a straightforward method to determine the ideal placement of a given number of nodes to reduce model errors.

4.6 Summary

In this paper we examine the requirement for mesh refinement around electrodes in Electrical Impedance Tomography (EIT). While it has been recommended that models be refined around the electrodes, where current density and sensitivity are highest, the level of refinement required is poorly understood. Using a set number of nodes, we investigate the optimal distribution between the electrodes and the volume of a model. A balance point is used to measure the difference in distribution between the electrode and the centre of the model. To calculate this, all nodes contained between the surface of a selected electrode and the centre of the model were identified and the mean position of nodes along the container axis was computed. We compare refinement strategies across commonly used meshing software in EIT and compare the model sensitivity error to an ultra-fine reference mesh. In a tank model, for a fixed number of nodes, error in the sensitivity calculation is minimized when the balance point of the nodes is at 85% of the tank radius and the node density dissipates evenly from the electrode surface to the centre of the model. Using this method sensitivity error was decreased in all regions with high sensitivity. This node

distribution technique enables the generation of accurate meshes with fewer nodes that can reduce measurement error and computing time.

Chapter 5

Custom EIT Meshes

This work has been presented in part at: the 21st International Conference on Biomedical Applications of Electrical Impedance Tomography (EIT 2021) (Stowe et al., 2021b).

Acknowledgement

Tidal Medical funded the work presented in this chapter.

5.1 Introduction

Acute respiratory distress syndrome ARDS is a form of respiratory failure caused by widespread swelling and accompanied by an accumulation of fluid in the lungs. ARDS is a challenging disease to diagnose and treat. No gold standard test exists for diagnosis, and few treatments are effective (Pham and Rubenfeld, 2017).

The mortality rate is estimated to be as high as 40% (Abe *et al.*, 2018). Early studies on the pathology of ARDS identified the effectiveness of adjusting positive end-expiratory pressure PEEP to improve oxygenation in patients (Ashbaugh *et al.*, 1967; Petty, 2001), and recent research suggests that treatment strategies to reduce lung injury during ventilation outperform pharmacological interventions (Duggal *et al.*, 2015). Monitoring ARDS patients during ventilation is vital to ensure that ventilator-induced lung injury is avoided (Bates and Smith, 2018), but few appropriate techniques are available. Computed tomography (CT) images used for diagnosis are inappropriate for continuous use due to ionizing radiation exposure, and other global parameters of lung function may not give an accurate estimate of lung homogeneity (Zhao *et al.*, 2009).

Electrical impedance tomography EIT was proposed as a monitoring technique for ARDS patients since it is non-invasive and can safely monitor and image the lungs in real time (Denaï *et al.*, 2010; Frerichs *et al.*, 2017). One of the most useful parameters to classify lung ventilation with EIT has been global inhomogeneity GI (Hochhausen *et al.*, 2019; Hough *et al.*, 2016; Hsu *et al.*, 2017; Humphreys *et al.*, 2011; Šribar *et al.*, 2020; Zhao *et al.*, 2012). GI has been identified as a clinically useful parameter to monitor ventilation (Frerichs and Becher, 2019).

The largest issue with using EIT for regional ventilation monitoring is that incorrectly modelling the boundary can introduce a large artefact in reconstructed images (Grychtol *et al.*, 2012). The correct lung boundary is also required to calculate the GI metric (Zhao *et al.*, 2009). Incorrectly modelling the boundary and lung area when investigating regional homogeneity can lead to an incorrect GI es-

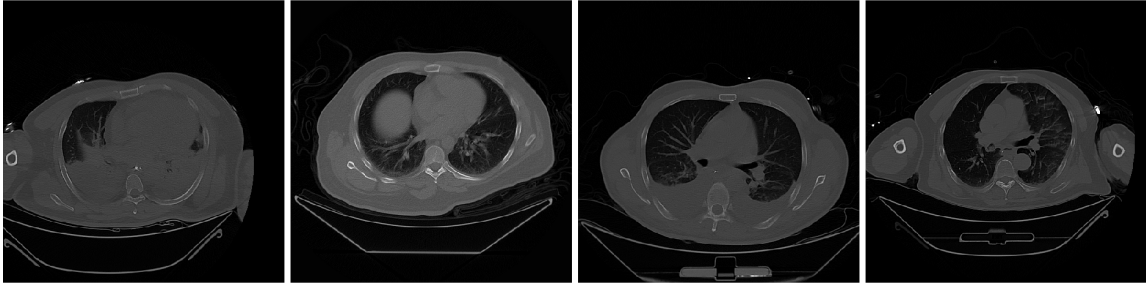


Figure 5.1: Raw CT data from 4 subjects taken at the 4th intercostal space. This image highlights the challenges with automatic segmentation of the lung and external boundary. In some subjects the external boundary is obscured by the arms, and in other subjects the true lung boundary is masked by occlusions.

timate (Yang *et al.*, 2021). Yang *et al.* (2021) found that a model with custom segmented external and lung boundaries was more sensitivite to changes in lung condition using GI compared with generic models. This suggests a custom mesh with more defined lung regions may also improve sensitivity to lung-based pulsatility and improve measures of perfusion.

Custom meshes have been created by segmenting the boundaries of lungs and organs to monitor ARDS (Yang *et al.*, 2021), but automatic segmentation of the lung region for a range of ARDS patients is a challenging problem. Typically ARDS patients will have a combination of swelling, fluid and lung collapse obscuring the true boundary of the lungs. Figure 5.1 depicts unprocessed CT slices of the 4th intercostal space from 4 subjects with ARDS. This figure highlights the challenges of automatically segmenting lung tissue across several subjects. In some CT images, the arms obscure the external boundary, and in other CT images partial or total occlusions mask the true lung boundary.

This chapter introduces a tool that enables quick segmentation of the lungs and exterior boundary to facilitate individualized bedside monitoring and guide treatment

of ARDS. This tool processes and automatically segments the external and lung boundaries in diagnostic CT images, then presents them for manual correction to create custom EIT models. The goal of this chapter is to generate custom models that improve sensitivity in the lung regions and produce custom, accurate meshes to facilitate real time, individualized ventilation monitoring for ARDS patients.

5.2 Methods

This section presents the methodology for:

- Automatic segmentation of diagnostic CT images (section 5.2.1)
- Design of a manual segmentation correction tool (section 5.2.2)
- Mesh generation (section 5.2.3)
- Comparison of GI index between generic and custom EIT models (section 5.2.4)

Figure 5.2 shows a summary of the mesh generation process from raw diagnostic CT data to a custom mesh based on the geometry of the patient.

For image segmentation and the manual correction interface Matlab 2021a (Mathworks, USA) with the image processing toolbox was used. Mesh generation and reconstruction was performed with EIDORS 3.10 (Adler *et al.*, 2017a) using Matlab 2019b. At the time of writing Matlab 2019b was required to use some EIDORS functionality, but Matlab 2021a provided some additional features that improved responsiveness of the graphical user interface GUI.

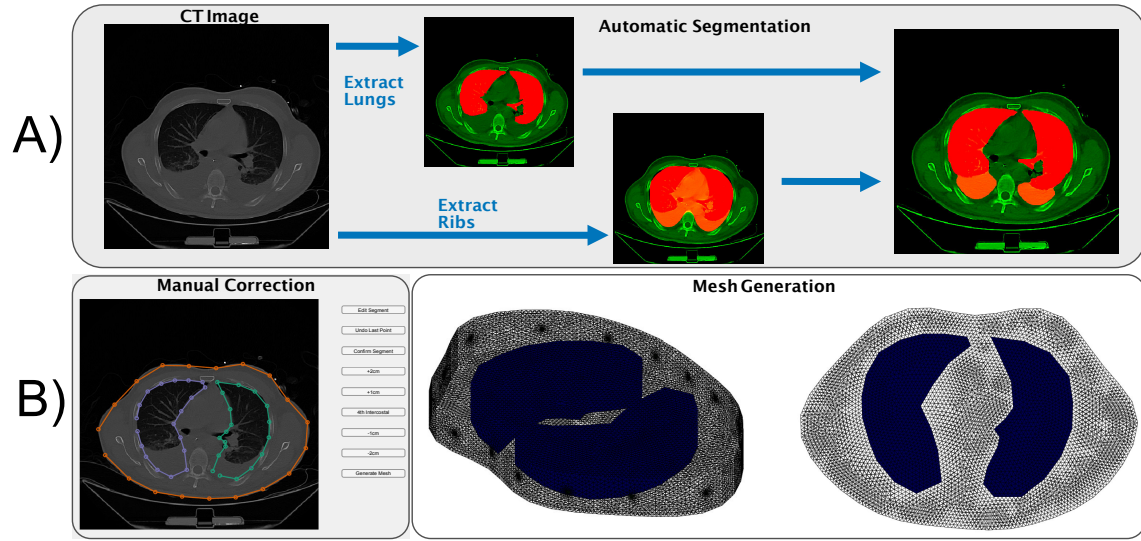


Figure 5.2: An overview of the segmentation and editing process showing: A) A sample raw CT which was thresholded, scaled and adjusted over several adjacent slices to identify the lung regions and an enclosed rib area, and the resulting lung estimate; and B) A screen capture of the manual mesh correction process and 2 views of the generated mesh.

5.2.1 Automatic segmentation of the thorax

Automatic segmentation of lung regions in ARDS patients is challenging due to the variability in lung tissue intensity, and the presence of fluid or collapsed lung regions. In some patients the lung regions were not visible in the image and even manual correction of the segmentation required estimation. This automatic technique identifies the chest cavity using several adjacent slices to locate the ribs. Even when no lung is visible in the image, this produces a starting point close to the expected boundary to reduce correction time. This tool is designed to segment the true lung boundary as closely as possible to simplify manual correction. If no ribs or lung are detected, ellipses are placed within the boundary close to the expected lung location that can be corrected manually.

The automatic segmentation uses a diagnostic CT image with the slice corresponding to the 4th intercostal space identified. To begin segmentation, the user must select the series of CT images they wish to segment, and the frame number that corresponds to the 4th intercostal space. For the 4 test subjects, the 4th intercostal space was identified manually using 3D Slicer 4 (Fedorov *et al.*, 2012), as the space between the 4th and 5th ribs underneath the arm. This location corresponded to the electrode belt placement for EIT measurements.

A detailed algorithmic outline of the automatic segmentation process is presented in appendix B.

5.2.1.1 External boundary

The boundary segmentation steps are shown in figure 5.3. To segment the boundary, the selected raw CT slice (A in figure 5.3) was adjusted so that the intensity of the lung tissue was 0 and the maximum image value was 1 (B in figure 5.3). Next the image was eroded and reconstructed to remove small features and retain large structures (C in figure 5.3). Finally, the image was binarized (D in figure 5.3), and holes were filled (E in figure 5.3), to give the final boundary (F in figure 5.3).

5.2.1.2 Chest cavity

To segment the chest cavity 7 slices above and below the 4th intercostal space were used giving 15 slices to segment. To begin, the external boundary of the selected slice was used (segmented using the method in section 5.2.1.1). The initial boundary (A in figure 5.4) was eroded to form a mask from the shrunken boundary shape (B

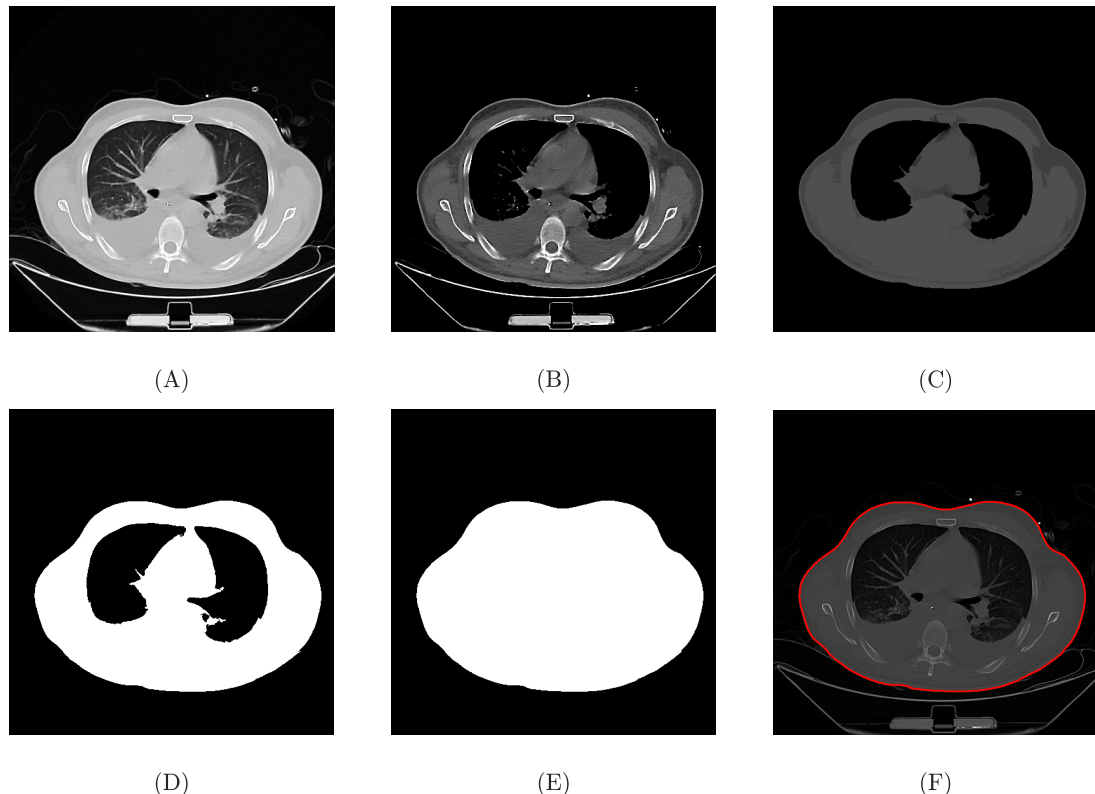


Figure 5.3: A raw CT image of the 4th intercostal slice (A) was adjusted based on the lung density (B), eroded and reconstructed (C), then binarized (D) and filled to give the final boundary (F).

in figure 5.4). This mask was used on a binarized image to extract bones and bright objects from within the thorax (C in figure 5.4). The image was closed to fill holes and identify bones (D in figure 5.4). Next all 15 adjacent slices were superimposed to combine all rib locations that occurred in more than one slice (E in figure 5.4). To fill holes in the ribcage, a rectangular element with a height of 5 and width of 50 was used to close the top half of the image (F in figure 5.4). A final thickening operation was performed to ensure continuity (G in figure 5.4). All objects connected to the boundary were removed to give the final chest cavity segmentation (H in figure 5.4).

5.2.1.3 Lungs

The lung segmentation was required to work in patients with ARDS and give an approximate lung boundary when the lungs were potentially collapsed or filled with fluid. To achieve this, a rough lung estimate based on the chest cavity was used together with a segmentation of the ventilated lung. The ventilated and non-ventilated regions of the lung were segmented based on the chest cavity segmentation (A in figure 5.5). First an estimation of the lung region was made by placing an ellipse in the centre of the chest cavity segmentation at the thinnest central point (B in figure 5.5). Next a ventilated lung estimate (C in figure 5.5) was made by inverting the binarized image from the external boundary segmentation (D in figure 5.3). Finally, a complete lung segmentation was generated by removing any part of the simple lung estimate (B in figure 5.5) that was within 5 pixels of the ventilated lung region, and combining the two lung estimates with a closing operation. This was able to give a close estimate of the lung boundary even in cases where little or no lung tissue was

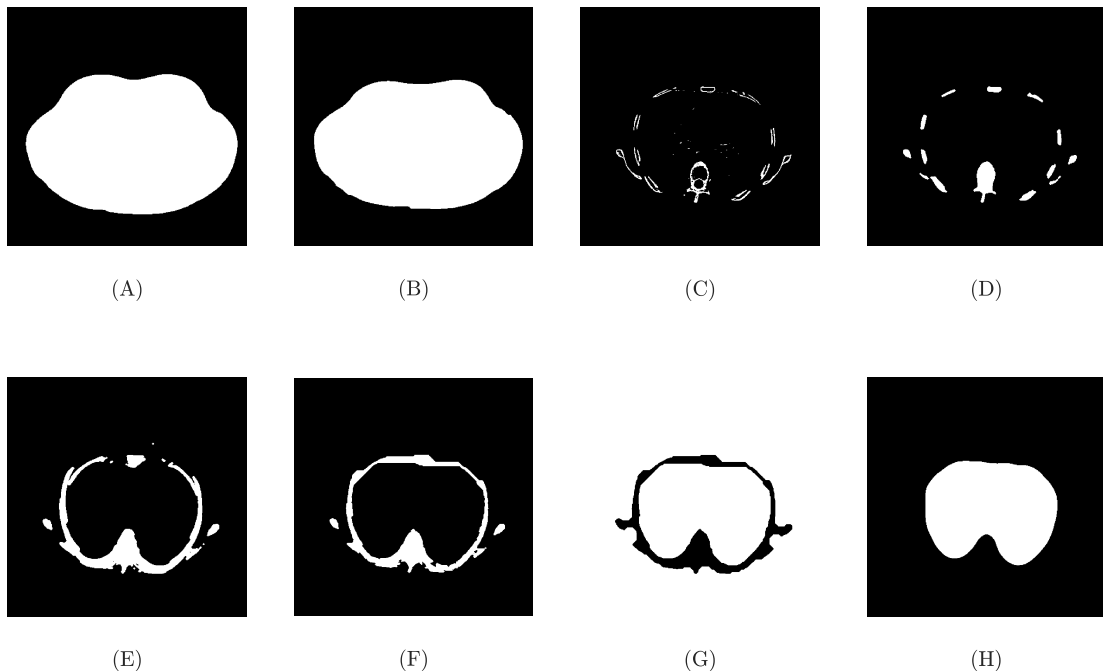


Figure 5.4: For each of the 15 selected slices the initial external boundary (A) was eroded to form a mask from the shrunken boundary shape (B). This mask was used on a binarized image to extract bones and bright objects from within the thorax (C). The image was closed to fill holes and identify bones (D). Next all 15 adjacent slices were superimposed to combine all rib locations that occurred in more than one slice (E). To fill holes, a rectangular element with a height of 5 and width of 50 was used to close the top half of the image (F). A final thickening operation was performed to ensure continuity (G). All objects connected to the boundary were removed to give the final chest cavity segmentation (H).

visually distinguishable.

5.2.2 Manual segmentation correction

Although the automatic segmentation was carefully designed to accurately segment the lungs, there were often cases where manual correction was required. To ensure accurate models were generated, an interface for manual correction was created. This tool allowed the user to correct the boundary for a selected CT slice. 20 points for each of the lungs and the external boundary were used for correction and placed over the corresponding CT image slice.

The segmentation correction tool was designed to save the segmentation with information on the selected image sequence and frame of the 4th intercostal space for reference. The segmentation correction also allowed users to load and correct previously saved segmentations, or overwrite them completely. An example of the setup, and available input for the segmentation correction GUI is shown in figure 5.6. To make segmentation simpler, all data such as the frame of the 4th intercostal space was saved after the initial data loading stage. Even if the segmentation was not completed, the user did not have to re-enter patient details when the CT was next loaded. An option was also added to manually input an adjustment value for the automatic segmentation of the ribs. If no ribs were detected during automatic segmentation, this could be used to adjust the threshold. This was not needed as the ribs were successfully identified in all test patients. The software was also designed to give informative error messages to enable troubleshooting, letting the user know if no ribs or no lungs were detected.

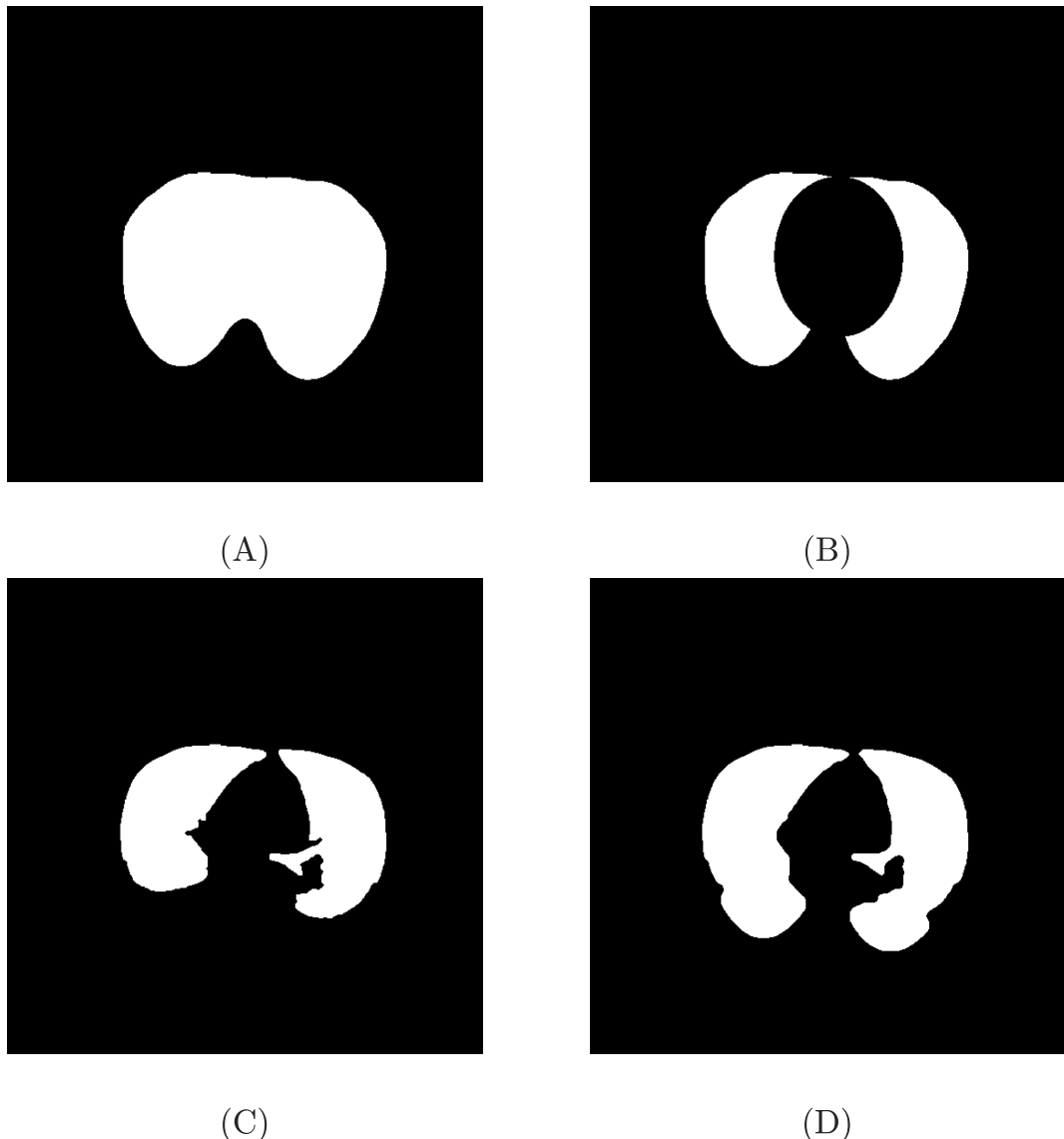


Figure 5.5: An approximation of the lung boundary was generated using the chest cavity segmentation (A) with an ellipse to remove the heart region (B). This was combined with a segmentation of the ventilated lung region (C) to give a total lung estimate (D).

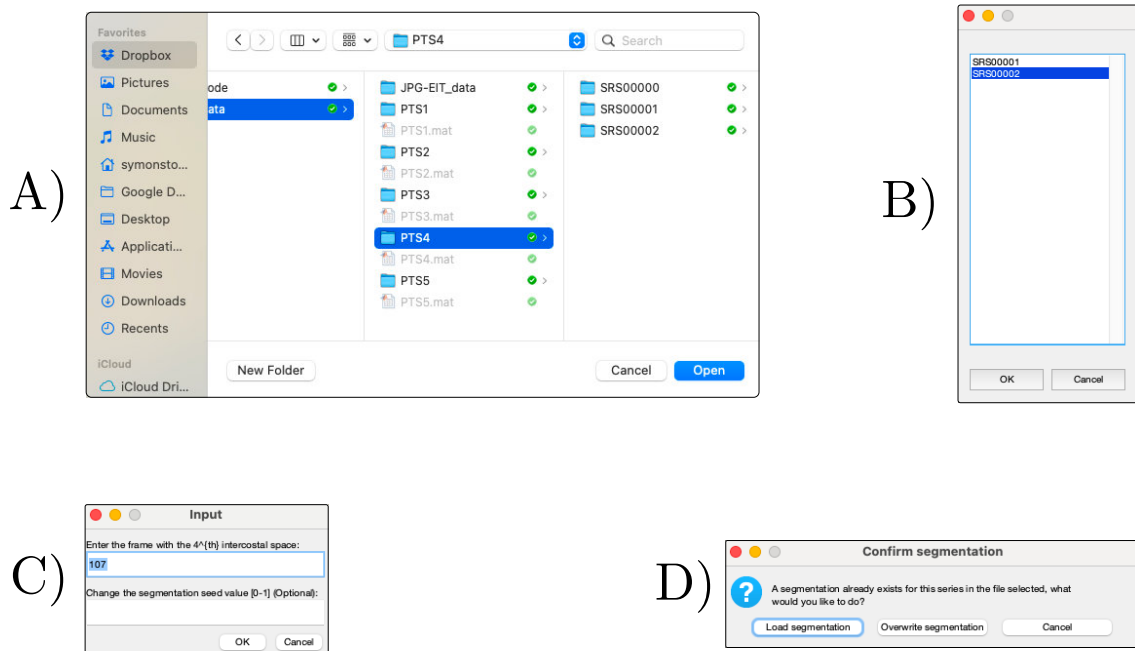


Figure 5.6: The data loading stages for the manual segmentation program are shown. A) A folder of patient data is selected. B) The desired CT data series is selected. C) The initial segmentation frame of the 4th intercostal space is loaded from the patient settings file or input by the user. Optionally, an adjustment to the initial segmentation thresholding value can be input if the segmentation steps failed to locate ribs in the CT image. D) If an existing segmentation was saved, the user is asked before a new segmentation is made.



Figure 5.7: An example of a segmentation after being loaded into the segment editor program. The buttons on the right show the options available to the user, and the left shows the CT image for the corresponding slice with the automatic segmentation overlaid.

If an error was made during manual correction, the user could undo the last change or revert the selected point to the original location. Keyboard shortcuts were assigned to each of the functions to reduce the time required to segment each slice.

Figure 5.7 shows an example of the Matlab GUI for manually correcting the automatic segmentation. To segment, the user would click *Edit Segment* then select and move each point that required correction. The first click by the user selected the nearest point, and the subsequent click placed the point at the new location. Buttons on the side allowed the user to select the CT slice for correction, save the segmentation, and generate a mesh.

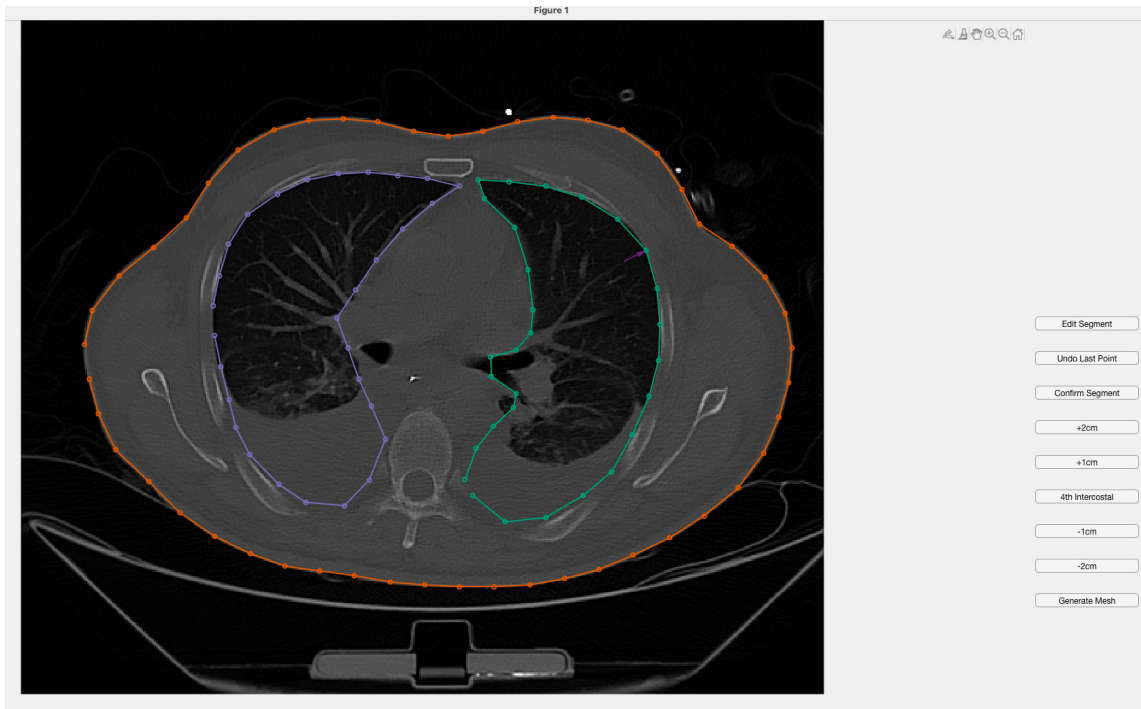


Figure 5.8: An example of a manually corrected segmentation with the arrow indicating the initial and new location of the last moved point. The selected point was moved for illustrative purposes and was not based on the initial segmentation.

After moving each point, an arrow was drawn between the original and new location of the point last moved to indicate the change and allow the user to see if the placement was correct. An example of a corrected slice showing the indicating arrow is shown in figure 5.8.

The end result was a GUI that allowed for quick correction of the automatic segmentation results. Spatial information from the DICOM image was also saved so that meshes could be designed to have the correct diameter and be correctly configured to the patient size.

5.2.3 Mesh generation

There is currently no available tool to automatically generate 3D meshes for EIT image reconstruction from a set of points, so the model was simplified using an extrusion technique. The `mk_extruded_model` function (Grychtol and Adler, 2013) in EIDORS v3.10 (Adler *et al.*, 2017a) was used to extrude the boundary of a single segmentation to a height of 20 cm. The 4th intercostal space segmentation was used for extrusion. The lungs were specified 2 ways, the first method extruded 2D lungs, from the selected segmentation, and the second generated a 3D lung from all corrected slices of the lungs. To select a 3D lung, we selected all elements of the extruded mesh contained within an alpha shape representation of the lung segmentation with an alpha value of 2 cm.

To generate a generic mesh for comparison the `mk_library_model` function in EIDORS was used which has available geometry for a cylindrical model with lung regions and a generic model of a human thorax. The conductivity of the lung regions was set to 0.7 of the background model conductivity.

All images were reconstructed using GREIT for 2D imaging (Adler *et al.*, 2009). For the GREIT reconstructions the noise figure was set to 0.5, 500 targets with a radius of 5 cm were used for training.

5.2.4 Evaluation on ARDS patients

Diagnostic CT data was acquired from 4 male patients aged 39–74. All patients were diagnosed with ARDS. EIT data were recorded using the Draeger EIT system on all patients with a 2D arrangement of 16 electrodes placed at the 4th intercostal space.

All patients were mechanically ventilated at the time of recordings, but the exact ventilation parameters were unknown.

To evaluate the effect of the custom models on lung sensitivity, the centre of mass was computed for both the ventilation region detected in CT images, and the breath volume reconstructed in CT images. The centre of mass was calculated from EIT images by removing all positive changes in the image, then locating the centre of mass of all pixels that were over 50% of the ventilation signal amplitude. The breath used for calculation was an ensemble average representative breath of all breaths in the signal. The error in the centre of mass was calculated between the EIT reconstructed breath and the CT segmentation in the number of pixels.

5.3 Results

The goal of the automatic segmentation algorithm was to generate segmentations that were accurate for quick and easy manual correction. Figure 5.9 shows the result of the automatic segmentation regions. The red overlay indicates the healthy lung segmentation, and the orange overlay indicated regions that were added using the estimation method. The lungs were examined visually to determine how much manual correction was required. During testing we found that the level of accuracy was sufficient to complete segmentation correction for each subject in under 1 minute.

The segmentation results show that there is good identification of the ventilated lung region from the automatic segmentation. The estimated lung regions also helped to give starting approximations for the lungs and decrease required manual correction

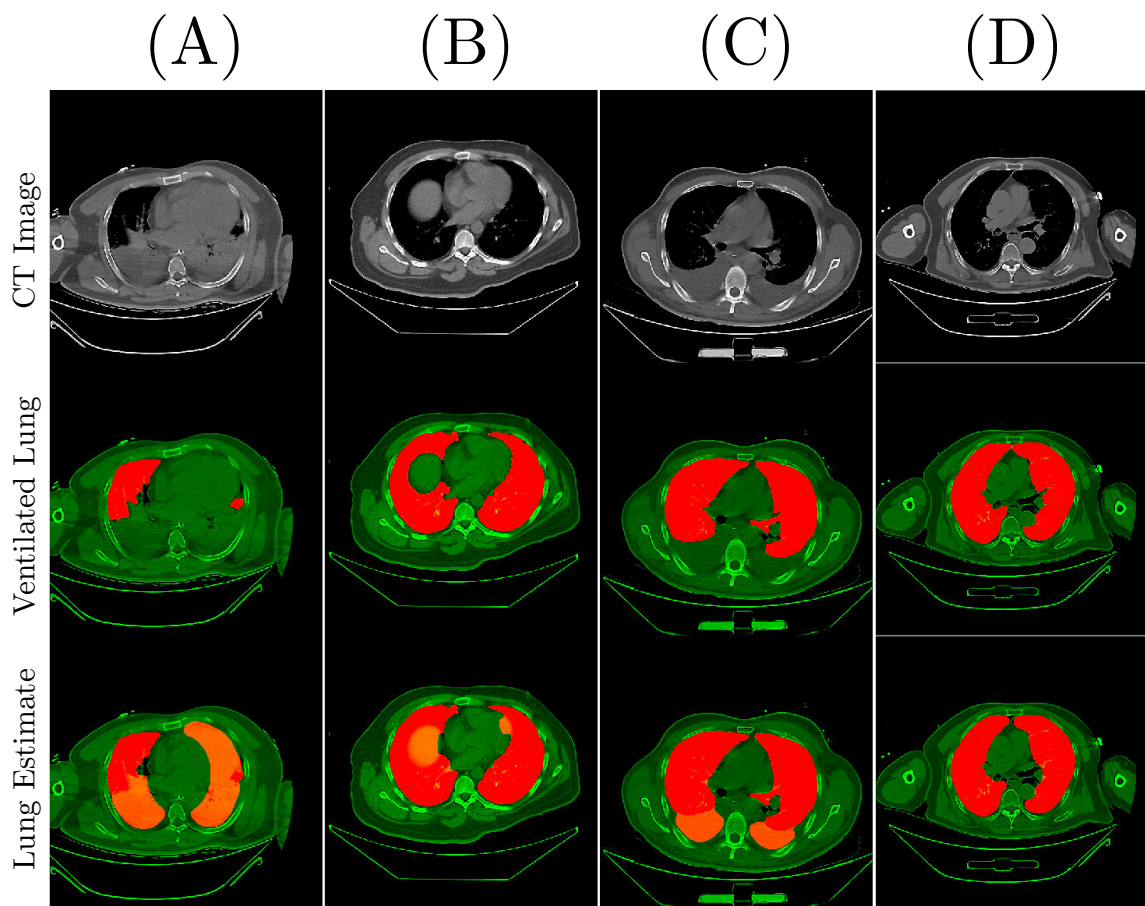


Figure 5.9: This figure shows the results of the automatic segmentation algorithm. The letters A–D represent the 4 patients. Patient A had a significant portion of the lung that was not ventilated, so an estimate was required to obtain lung regions. The ventilated lung estimate is shown in red on the 2nd and 3rd columns. The total lung area using the chest cavity and ventilated lung area is shown in the bottom row.

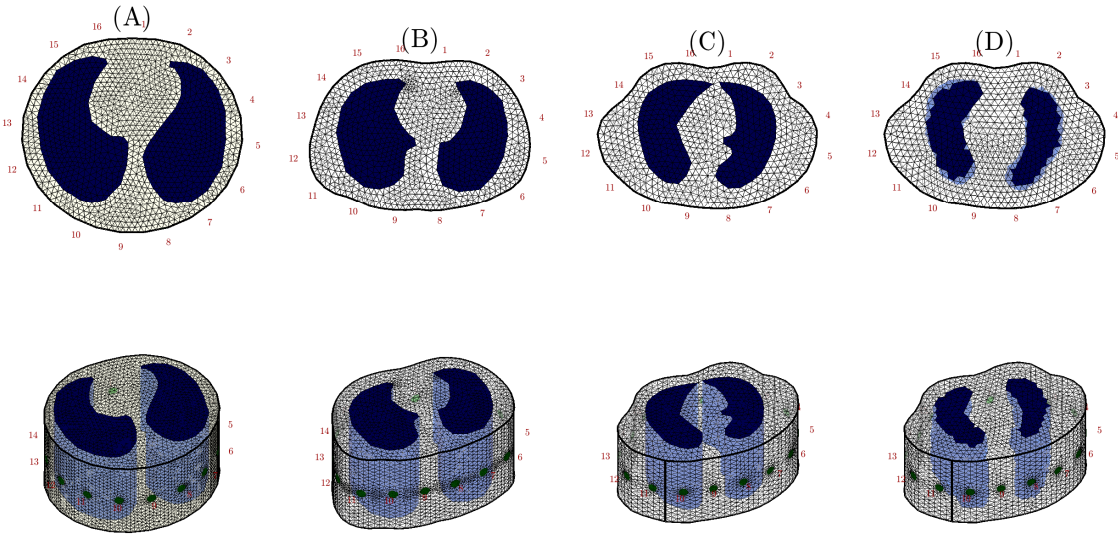


Figure 5.10: Example meshes and electrode locations for subject C (from figure 5.9). Model (A) is circular with lung regions. Model (B) uses the generic chest model from EIDORS and models (C) and (D) use the custom segmentation boundaries. Model (C) uses 2D lung boundaries from the 4th intercostal space extruded for the model height. Model (D) selects all elements are within the 3D lung boundary identified by the segmentation results.

time when there was limited ventilated lung in the available CT image. Sample meshes generated from the segmented images are shown in figure 5.10 for subject C (in figure 5.9).

For each patient there was a single EIT recording ranging from 30 – 60 seconds in length. To determine the improvement for the new customized meshes the ventilation pattern from the CT image was compared to the reconstructed ventilation on 4 types of models. The 4 types of meshes compared are pictured in figure 5.10: The first mesh was cylindrical with approximate lung regions, the second mesh was a generic model for an adult thorax, and the final two meshes were created from the segmentations. To compare the performance across all models, the centre of mass was compared

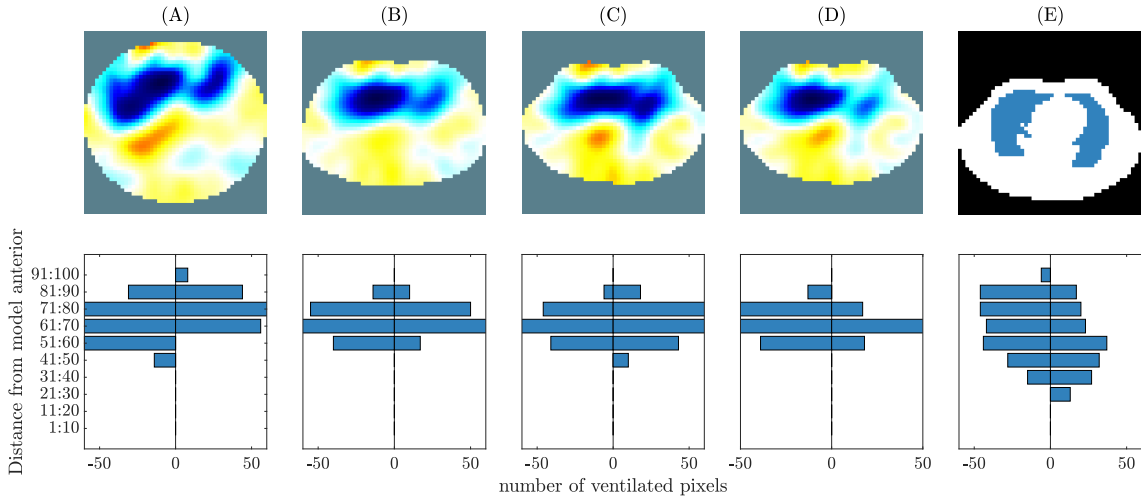


Figure 5.11: Example ventilation distribution for subject C (from figure 5.9). Column A and B are the generic models from the EIDORS library. Columns C and D show the custom models with 2D lungs (C) and 3D lung regions (D). Column E shows the distribution of the ventilated lung as segmented from the CT image.

between the CT imaged ventilation and the EIT imaged ventilation.

Reconstructed images in figure 5.11 show a very limited difference in ventilated regions and centre of mass between custom and generic models. There is a noticeable change in ventilation distribution using the circular model, but the generic thorax model and the custom models show very similar results. There is a slight shape difference in the ventilation distribution between the generic thorax model and custom models, but there is very little measurable difference.

Error in the centre of mass across all models for all subjects was calculated and is shown in figure 5.12. The error is estimated as the distance in pixels between the venter of mass of the ventilated lung from the CT estimate and the centre of mass of the reconstructed breath.

The centre of mass error was not significantly different across all models for each

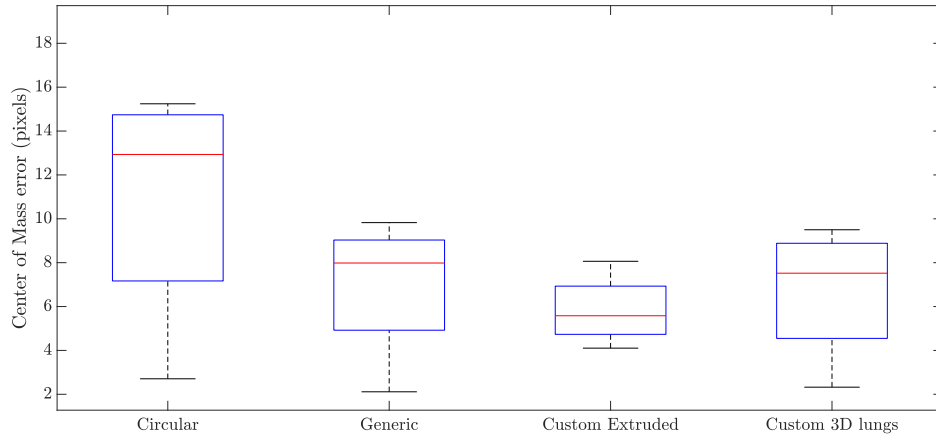


Figure 5.12: Example ventilation distribution for subject C (from figure 5.9). Column A and B are the generic models from the EIDORS library. Columns C and D show the custom models with 2D lungs (C) and 3D lung regions (D). Column E shows the distribution of the ventilated lung as segmented from the CT image.

of the subjects. The average error for the circular model was slightly higher than the customized geometry, but for all models the centre of mass, and shape of the ventilation distribution was similar. It is not clear that custom models improved reconstruction accuracy of breath reconstructions in the EIT images. There are several factors that may contribute to this.

5.4 Discussion

The goal of this chapter was to create a tool to automatically segment CT images from ARDS patients to improve lung sensitivity to improve individualized ventilation monitoring. An automatic segmentation algorithm was developed to give a baseline segmentation of the lungs which gave an accurate starting point of the true lung

boundary. A tool for manual correction was designed that enabled quick, accurate corrections of automatically generated CT images. Segmented images were used to generate meshes with accurate boundary shapes and lung outlines.

Although it has been shown that accurate models of the boundary and lung improve measures of GI index (Yang *et al.*, 2021), the models with improved boundary accuracy in this chapter did not show this improvement. One factor that was different between the two studies was the value of lung conductivity. Yang *et al.* (2021) used a conductivity value of 1.3 for the lung tissue relative to the model background. This is atypical since the conductivity of lung tissue is considerably lower than other tissues in the body. In this chapter using a value of 1.3 times the background conductivity did not improve the centre of mass error across custom models.

There are several other factors that may contribute to the mismatch between the CT ventilation and the EIT imaged ventilation. First, the difference in posture and condition between the CT and the EIT image was not known. The EIT belt was not in position during the CT scan, so there was potential that the patient position and posture were slightly changed. Although this may contribute to a slightly different shape of the thorax, it is not likely to drastically change the boundary of the chest cavity. One of the larger factors is likely the unknown locations of the electrodes. Since the exact location of the electrode is unknown, the 16 electrodes were placed evenly around the thorax. Incorrect electrode locations can have a large impact on the resulting EIT image, resulting in artefact and lower reconstruction accuracy (Boyle and Adler, 2011). Since the CT images acquired contain spatial information, there is potential to improve accuracy of the electrode placement on the models.

The EIT system used has several available belts with different electrode spacing and points of attachment. If the user was able to select the belt used and the attachment point or tightness in the software, the electrode locations could be more easily approximated. Alternatively, an image or CT with the electrode belt in place could allow precise estimation of the electrode location and spacing. It may also be feasible to reconstruct the electrode location partially using a movement jacobian (Soleimani *et al.*, 2006), although it is not currently possible to do this with the GREIT algorithm.

On top of improving the accuracy of the electrode placement in the meshes there is still future development planned for the segment editor and automatic segmentation. Initial tests were done on the CT and EIT data from 4 patients, and validation across a wider dataset is required to ensure stability of the automatic segmentation and ease of editing. Improvements to the appearance of the interface and documentation must also be added before the software is easy to use in a clinical setting. Work is currently underway to obtain several more sets of CT and EIT data to validate the automatic segmentation and manual correction steps.

It was noted in the reconstructions that when using the 3D lung region model there was a slight reduction in the amplitude of a conductive artefact that appeared in the center of the iamges. It is possible that the the 3D aspect of the model allows the 3D path of the current to be modelled more accurately (Adler and Boyle, 2017), but the extent of the benefit is limited when using a 2D arrangement of electrodes (Grychtol *et al.*, 2016).

When creating meshes using the `ng_mk_extruded_model` in EIDORS (Grychtol

and Adler, 2013), accurate models with a good representation of the boundary are created, but Netgen occasionally fails to mesh the electrodes on models. We presume this is due to irregular and concave curves. This occurred several times on the segmented data, and a more robust meshing or electrode placement technique will be required. Placing 3D lung boundaries helped to reduce errors that were introduced by tight corners on lung segmentations, but electrode and boundary meshing errors were still present in this model.

5.5 Summary

The diagnostic CT images required for ARDS diagnosis are an excellent source of spatial information about the size and location of organs in a subject. A segmentation and boundary editing tool was developed to generate accurate meshes of the external and lung boundaries from CT images. In ARDS patients with very poor lung health segmentation of the actual lung boundary is challenging, but with a multi-step process including chest cavity segmentation and manual verification, we generated accurate, custom meshes for a small number of ARDS patients. The benefits of custom meshes were not clear on this small sample size, although additional steps to improve electrode localization may improve results. Work is currently underway to validate and improve the segmentation tool on a larger dataset of ARDS patients. Methods to reduce the impact of sensitivity to electrode location error on reconstructions, or correctly identify correct electrode locations could help make this technique more viable.

Chapter 6

Internal Electrode Sensitivity

This sensitivity analysis work has been presented in part at: the 42nd Annual International Conference of the IEEE Engineering in Medicine & Biology Society (EMBC 2020) (Stowe and Adler, 2020).

6.1 Introduction

Currently the most common implementations of EIT in biomedical applications measure voltages and inject currents from the body surface using one or two planes of electrodes. Internal electrodes are not used clinically despite promising simulation studies that have shown large improvements in reconstruction accuracy and internal sensitivity in 2D (Nasehi Tehrani *et al.*, 2012a; Nasehi Tehrani *et al.*, 2012b). In practice, EIT images with internal electrodes are challenging to interpret as the measurements are prone to significant differences due to probe positioning (Czaplik *et al.*, 2014).

As discussed in chapter 3, one of the main challenges in perfusion imaging is the large difference in amplitude between the ventilation and cardiac signals. When using external electrodes, the respiratory amplitude is significantly larger than the cardiac component. Techniques such as breath holds, induced apnoea (Leathard *et al.*, 1994; Stowe *et al.*, 2019), or injection of a contrast agent (Frerichs *et al.*, 2002) can reduce the impact of the respiratory signal, but they are not feasible for long-term or continuous monitoring. Other methods such as averaging a large number of signals together have been used (Eyüboğlu *et al.*, 1989; Vonk-Noordegraaf *et al.*, 1998), but as discussed by Deibele *et al.* (2008) these do not allow real-time monitoring and may miss sudden changes in perfusion that are of interest. Filtering techniques have been implemented to help isolate the cardiac component of the signal, but there is also occasionally overlap between the carsiosynchronous component and harmonics of the ventilation signal which makes signal separation more challenging (Leathard *et al.*, 1994; Zadehkoochak *et al.*, 1992).

Low sensitivity in central regions relative to the boundary limits the clinical applications of EIT, reducing the ability to accurately reconstruct and identify impedance changes due to the heart.

Internal electrodes have been proposed several times as a method to sustainably increase sensitivity in central regions of the chest and improve EIT reconstruction accuracy (Czaplik *et al.*, 2014; Nasehi Tehrani *et al.*, 2012b; Nguyen *et al.*, 2020; Pilkington *et al.*, 1989; Schuessler and Bates, 1995). Past research in 2D identified a sixfold increase in the cardiac frequency component of the EIT signal when 2 of 16 total electrodes were placed in the esophagus or trachea (Czaplik *et al.*, 2014).

It is not clear whether the identified increase in cardiac-frequency amplitude stems from pulsatile (motion-based), changes or whether these changes represent perfusion, however internal electrodes in 2D have been shown to increase sensitivity to these cardiosynchronous signals.

There is potential for clinical use of internal electrodes to monitor ventilation, perfusion and hemodynamic changes in the intensive-care unit (ICU), where patients typically have breathing and feeding tubes in place.

EIT applications in development include mechanical ventilation guidance and monitoring (Frerichs *et al.*, 2017), perfusion monitoring (Frerichs *et al.*, 2002; Smit *et al.*, 2003), blood pressure monitoring (Proen  a *et al.*, 2017; Sol  a *et al.*, 2011), and cardiovascular output (Braun *et al.*, 2018a). For all of these uses of EIT, internal sensitivity in the centre of a model could provide increased accuracy. In an intensive-care environment where feeding and breathing tubes are used internal electrodes could provide several advantages without additional invasiveness. It has also been suggested that internal electrodes may replace electrodes on the back, which are challenging to place in critically ill patients that cannot be safely or easily moved (Czaplik *et al.*, 2014).

Especially while monitoring perfusion where the main challenge has been the small amplitude of the cardiac signal from the surface electrodes (Nguyen *et al.*, 2012), internal electrodes offer potential for significant improvement. This chapter presents a 3D EIT configuration with internal electrodes that can be used to maintain a high sensitivity in regions with large pulsatile components in the centre of a model. An electrode injection pattern to increase internal sensitivity is also compared to the

standard measurement and injection pattern used in 3D.

The sensitivity benefits of internal electrode imaging in 3D are assessed in simulation to determine the feasibility of using internal electrodes to improve perfusion monitoring. This chapter provides proof of principle for internal electrode configurations in 3D to improve EIT sensitivity.

6.2 Methods

6.2.1 Tank model

To analyze the sensitivity changes due to different electrode configurations finite element models (FEMs) of a cylindrical tank were created with each of the tested electrode configurations. Figure 6.1 shows the four different configurations that were tested: a 2D electrode ring of 32 electrodes; a 3D configuration of 2 layers of 16 electrodes (3D(a)); a second 3D configuration of 2 layers of 15 electrodes plus 2 central internal electrodes inline with the electrode planes (3D(b)); and a final 3D configuration of 2 layers of 14 electrodes with 4 central internal electrodes evenly spaced between the electrode planes (3D(c)).

The tank in the simulations has a height of 2 m, radius of 1 m, and the electrode radius is 0.05 m for both the round external electrodes and the spherical internal electrodes. In the 3D configurations, the plane separation is 0.5 m and in all configurations the radial spacing between electrodes is equal. The background conductivity of the tank was 1 S/m and the conductivity of the target was 10 S/m.

When reconstructing images a conductive target was added to the tank centred

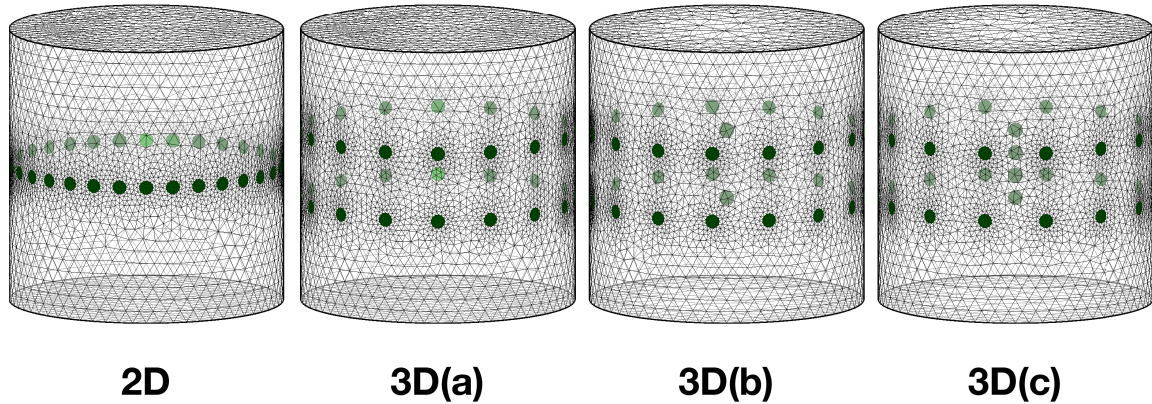


Figure 6.1: 4 configurations of electrodes were tested: 2D) a single ring of 32 electrodes; 3D(a) 2 rows of 16 external electrodes; 3D(b) 2 rows of 15 external electrodes with 2 internal electrodes; and 3D(c) 2 rows of 14 external electrodes and 4 internal electrodes.

at a height of 1 m at the midpoint of the tank radius. The target object radius is 0.4 m.

6.2.2 Image reconstruction

To generate EIT images from voltage measurements, the 3D GREIT reconstruction algorithm was used (Grychtol *et al.*, 2016). A spherical conductive target with a radius of 20 percent of the tank radius was placed midway between the centre and boundary of the tank, in a region with typically low sensitivity. The inverse problem hyperparameter was selected so that in all instances the amount of measurement noise that propagated from the measurements into the final images was equal.

6.2.3 Sensitivity calculation

The sensitivity is then calculated from the jacobian (J) of the reconstruction matrix as:

$$S = \frac{\sqrt{\sum_i J_{ij}^2}}{V_i} \quad (6.1)$$

where V_i is the volume of each respective voxel.

6.2.4 Current injection and measurement

For this analysis external electrodes are placed in a “square” pattern (Grychtol *et al.*, 2016) and the internal electrodes are placed from top to bottom.

The current injection pattern used in this analysis was the typical “skip 4” injection pattern that has been shown to yield a good sensitivity distribution in 3D EIT (Grychtol *et al.*, 2016). A new stimulation and measurement pattern is also used in a model with two internal electrodes that increases the number of measurements on the internal probe. The stimulation pattern is consistent with the skip 4 pattern, but for the measurements alternating stimulations and measurements are replaced with measurements to the internal probe.

This results in the same number of measurements, but many more measurements use the internal probe. This new stimulation pattern is described in figure 6.2. All measurements are made between the top and bottom plane of electrodes.

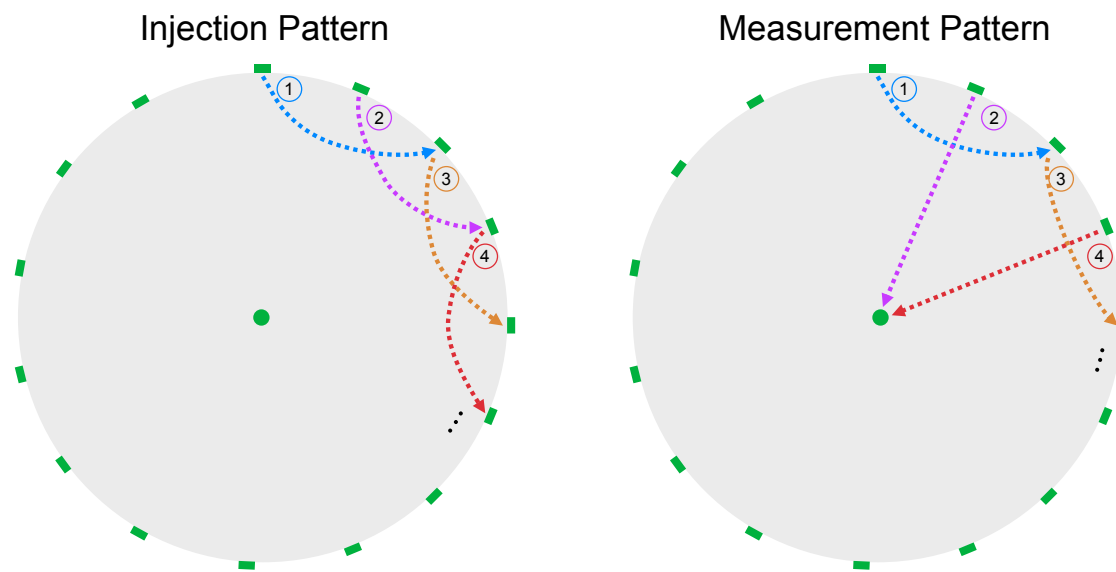


Figure 6.2: A proposed current injection and measurement pattern for EIT imaging with 2 internal electrodes. The injection pattern is a typical “skip 4” pattern injecting between every 5th electrode in a square electrode layout and the measurement pattern replaces every 2nd measurement in the typical method with a measurement between the internal probe and external rings. Note: this figure does not differentiate between upper and lower electrode planes, but all injections and measurements are done between the 2 planes.

6.3 Results

Reconstructions of the conductive object with and without additive noise are shown in figure 6.3. With and without additive measurement noise, all models are able to reconstruct the target object accurately. Measurements with internal electrodes appear to reconstruct the target closer to the actual size.

Figure 6.4 show internal sensitivity distribution changes when using two and four internal electrodes compared to the typical 2D and 3D configurations with only external electrodes. The highest central sensitivity can be seen when using four internal electrodes. This electrode configuration also gives a higher sensitivity in between the internal electrodes and the tank boundary.

These results show the expected increased sensitivity in the central regions of the model. To further improve internal sensitivity a new measurement pattern is proposed that uses more measurements between the internal probe and peripheral electrodes. The sensitivity of the proposed pattern was compared to the sensitivity profile of the same configuration using the basic “skip 4” injection pattern. Using this injection pattern results show a further increase in sensitivity in the internal regions without increasing the measurement acquisition time. The sensitivity distribution for the new injection pattern is pictured in Figure 6.5.

6.3.1 Sensitivity in an ovine model

A sensitivity comparison was also computed for an ovine model with different electrode configurations and is shown below in figure 6.6. Due to the location of the

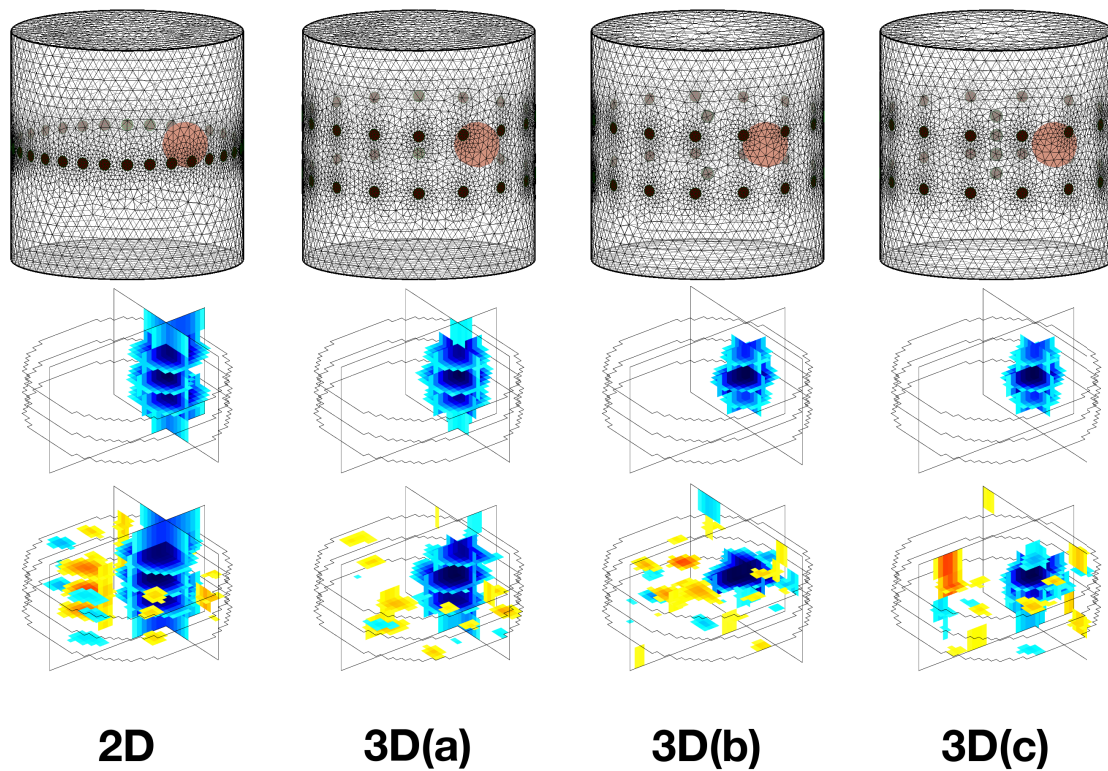


Figure 6.3: The top row shows reconstructions with no additive noise, and the second row shows reconstructions on measurements with 5dB of additive noise.

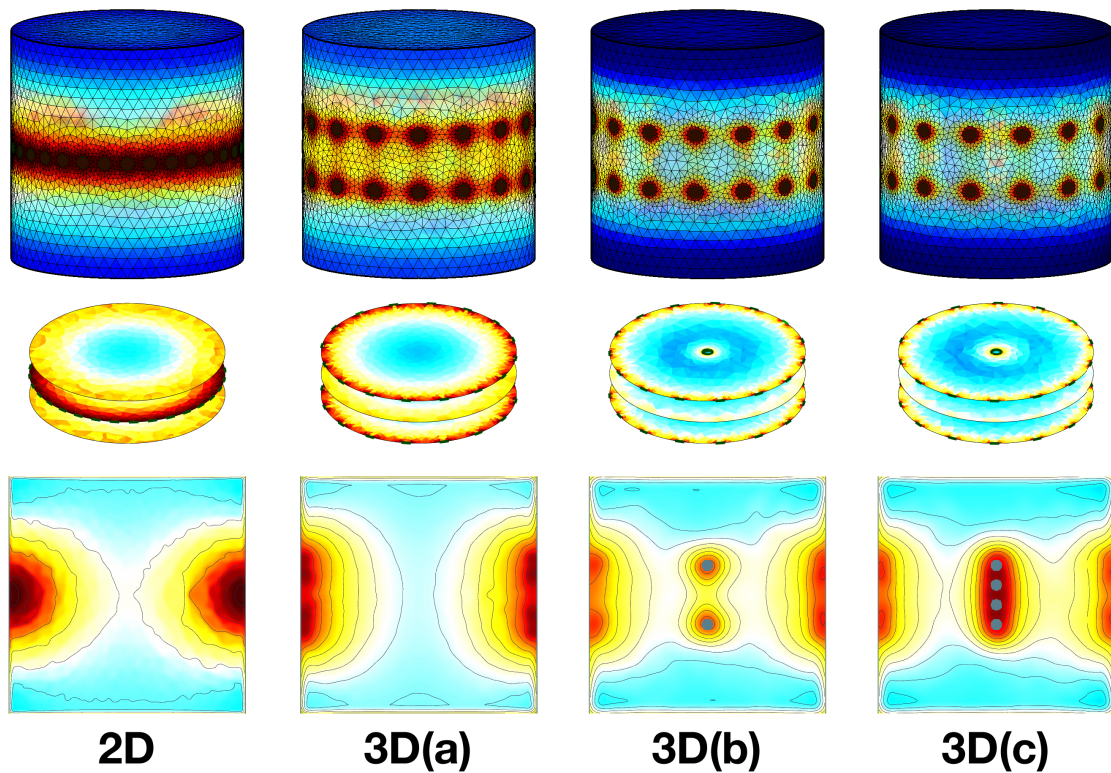


Figure 6.4: Sensitivity distributions for electrode patterns from left to right: A single 2D electrode plane; 2 electrode planes of 16 electrodes each; 2 internal electrodes and 2 external electrode rings of 15 electrodes; 4 internal electrodes arranged between 2 planes of 14 external electrodes

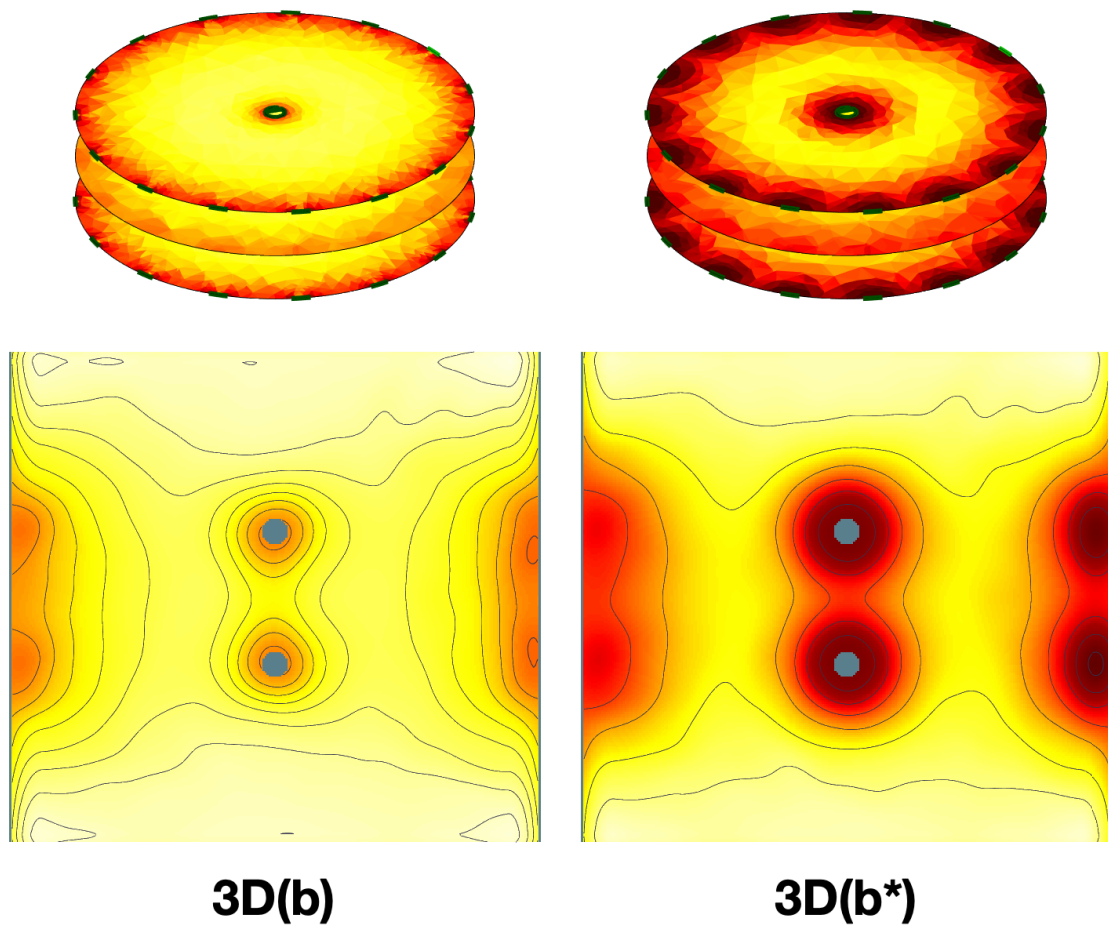


Figure 6.5: A comparison between the sensitivity distributions for a typical “skip 4” injection pattern pictured on the left (3D(b)) and the modified injection and measurement pattern on the right (3D(b*)).

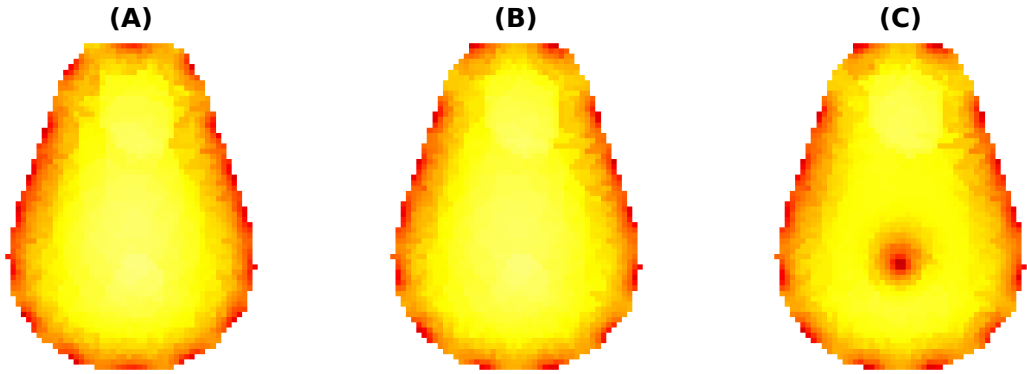


Figure 6.6: Sensitivity distribution averaged across 10 evenly spaced layers between the electrode planes in the lamb model for: A) 32 external electrodes B) 28 external electrodes c) 28 external electrodes and 4 internal electrodes.

esophagus in adult sheep and the distance from the heart adding internal electrodes resulted in a minimal sensitivity decrease in the heart region of the model (<1%), but there is a significant sensitivity increase in the area immediately surrounding the probe.

6.4 Discussion

Based on the simulations presented in this chapter internal electrodes were able to increase the sensitivity in the central regions of the model significantly. Reconstruction in 3D with GREIT was able to accurately reconstruct the location of an object in 3D with both two and four internal electrodes in the presence of 5 dB measurement noise.

These results align with findings from Nasehi Tehrani *et al.* (2012) who demonstrated that internal electrodes in 2D result in a higher reconstruction accuracy and a much higher internal sensitivity relative to external configurations.

The presented data validates that the benefits of internal electrodes seen in 2D are also realizable in 3D, but there is more work required to quantify and validate the improvements in real-world settings. Additionally reconstructions on a static target with a static electrode probe are relatively simple. It has been shown that electrode motion and boundary deformation are major contributing factors to error in EIT recordings (Boyle and Adler, 2011; Grychtol *et al.*, 2012), and this has been presented as an additional concern when using internal electrodes that there is currently no solution for (Nguyen *et al.*, 2020). The following chapter explores this source of error in more detail and provides a solution to correct for internal motion.

While the modified current injection pattern increased sensitivity in central regions of the model, it is not likely feasible for real-world use. The majority of commercially available EIT systems use fixed stimulation and measurement spacing and would not be able to accommodate this type of measurement. Additionally if movement of the internal probe is one of the main sources of artefacts when using internal electrodes, it is possible that using the probe for more measurements will not improve the reconstructed image.

Sensitively modelling in an ovine model showed a large increase in sensitivity surrounding the internal probe, but no improvement in sensitivity in the heart region. The ovine model is very different to the human model where the heart is much closer to the esophagus. The ovine model may be sufficient to analyze the feasibility of internal electrodes for ventilation and lung perfusion imaging, but may not be comparable to data collected in humans due to the difference in physiology.

These results serve as a starting point for 3D EIT, demonstrating that sensitivity

increases in the centre of the model when using internal electrodes. Four internal electrodes gave the largest increase in internal sensitivity. The next chapter elaborates on the benefit of internal electrodes demonstrating reconstruction accuracy in simulations.

6.5 Summary

Reconstructions using the GREIT algorithm with internal electrodes on an esophageal probe were able to give increased sensitivity in internal regions. This shows promise for increased sensitivity to cardiosynchronous signals and may allow better isolation of pulsatile motion related to perfusion. The following chapter further investigates the impact of motion on internal electrodes.

Chapter 7

Internal Electrode Motion

Preliminary animal reconstructions have been presented in part at: the 21st International Conference on Biomedical Applications of Electrical Impedance Tomography (EIT 2021) (Stowe et al., 2021a).

7.1 Introduction

As discussed in section 2.2, several factors contribute towards the cardiosynchronous signal in EIT. One of the largest contributions is movement; both the movement of body structures and the movement of electrodes contribute significantly to the measured impedance and the resulting reconstructed image (Adler *et al.*, 2017b; Proen  a *et al.*, 2015). The previous chapters support that more accurate meshing and internal electrodes may help to identify the movement of structures and organs, isolating their impact on the reconstructed images, but the problem of electrode motion is amplified when internal electrodes are used. Internal electrodes placed on a

probe are challenging to locate within a subject due to variation in individual geometries. Incorrectly modelling the electrode locations can introduce an artefact in the image (Boyle and Adler, 2011), but in time difference EIT these effects are minimized (Adler and Boyle, 2017). The larger problem appears to be the movement of the internal probe relative to the external electrodes between measurements. Recent work by Nguyen *et al.* (2020) reviewed the potential application of internal electrodes in cardio radiofrequency ablation and discussed the need for an analysis of the effect of heart motion on the internal electrode, and a solution to correct for its impact on EIT reconstructions.

Movement correction algorithms using the movement jacobian have been designed in 2D and 3D (Gómez-Laberge and Adler, 2007; Gómez-Laberge and Adler, 2008; Soleimani *et al.*, 2006) and used to reconstruct electrode movement on 3D models with a 2D arrangement of electrodes (Boyle, 2016). There are several available methods to calculate the movement jacobian (Boyle *et al.*, 2017), the simplest of which, the naïve perturbation method (Gómez-Laberge and Adler, 2008), has been used in this chapter as a proof of concept. A more detailed explanation of this jacobian calculation method is presented in section 2.4.6.1 of the background. As an internal probe moves towards one side of a model the distance between the probe and the external electrodes changes. This results in less impedance where the distance has decreased, and a higher impedance where the distance has increased. Without knowing the new probe location we can minimize the effect of this error, but there still remains a mismatch between the modelled and actual probe locations. The artefact that is reconstructed can give hints regarding the motion of electrodes, although it can

be difficult to separate the effect of electrode movement from biological impedance changes of interest (Boyle, 2016).

This chapter presents a method that builds on current algorithms available, to create a new, corrected model that helps to compensate for the effect of electrode movement. The known shape of the artefact due to movement of the probe is used to derive the probe location, and create a corrected model to improve reconstruction accuracy in the presence of probe motion.

The goal of this chapter is to establish a technique to reduce the impact of probe movement on image reconstructions, and then to use this technique in an animal model. Although simulations in 2D and now in 3D show that internal electrodes can provide a desirable increase in sensitivity, the benefit has not been realized in real-world recordings. This chapter presents a novel method to correct for electrode displacement artefacts, and compares established techniques for 3D EIT image reconstruction to reconstructions with the novel internal electrode approach in a limited number of subjects.

7.2 Methods

This chapter consists of two experiments: a simulation study correcting for probe motion in a tank model, and preliminary *in-vivo* recordings that were conducted as an addition to another experimental protocol.

7.2.1 Simulations

Simulations were done using EIDORS (v3.10) (Adler *et al.*, 2017a) using Matlab 2019b (Matworks, Natick, MA, USA). Within EIDORS, meshes were generated using Netgen (version 5.3.1) (Schöberl, 1997).

7.2.1.1 Tank models

A model of a tank with 28 external electrodes placed in two planes of 14 evenly around the exterior and 4 internal electrodes was created. The tank radius and height were 1 m, and the external electrode radius was 5 cm. The external electrode planes were placed at a height of 0.3 m and 0.7 m on the tank. The internal electrodes were spaced evenly between the external electrode planes at 0.3 m, 0.433 m, 0.567 m and 0.7 m. The internal electrodes were specified in two different ways. The first used spheres with a radius of 2.5 cm, and the second used a hollow cylinder with a radius of 2.5 cm containing cylindrical electrodes with a radius of 2.5 cm and a height of 5 cm. External electrodes were placed in a “square” electrode configuration (Grychtol *et al.*, 2016). Both models are shown in figure 7.1.

These models were compared to confirm that both performed adequately with motion correction, as internal electrodes are challenging to model and many different techniques are used. When using internal electrodes on a complex model, it is currently easiest to add electrodes along a hollow tube cut through the centre.

To specify a conductive region elements within a radius were assigned a conductivity of twice the background conductivity of the tank model. The conductive target was placed midway between the centre of the tank and the boundary. The radius

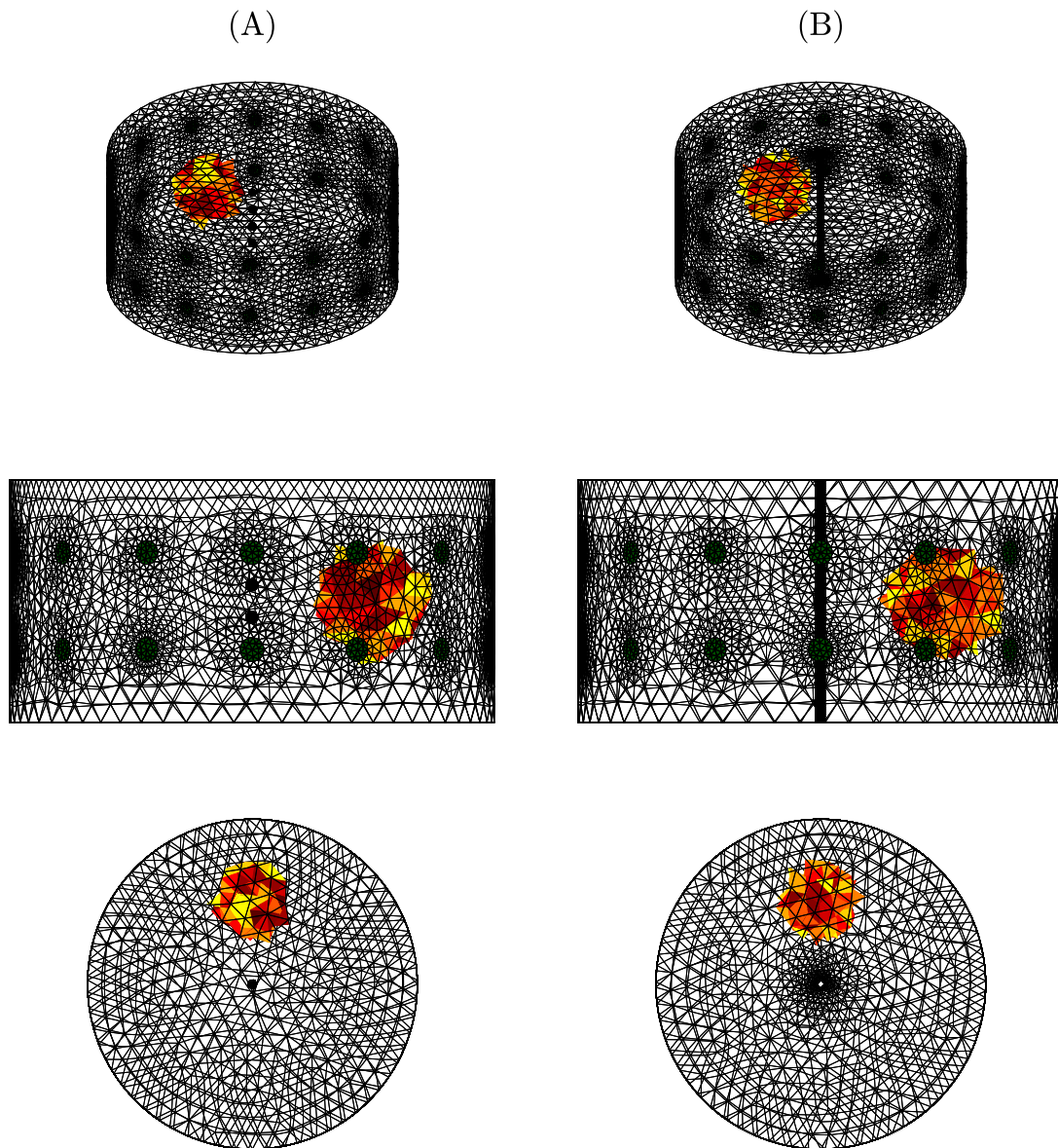


Figure 7.1: On the left (A) internal electrodes were modelled as 4 spherical electrodes between the external electrode planes. On the right (B) the internal electrodes were created using a hole through the centre of the model and using cylindrical electrodes on the inner surface of the model. The conductive region was specified by setting the conductivity of all elements contained in the target to be twice the background conductivity.

of the target was 20 cm. Figure 7.1 shows the conductive target for both internal probe types.

7.2.1.2 Measurements

Despite sensitivity advantages ascribed to custom injection and measurement patterns, the skip 4 pattern was used as it is straight forward to implement with currently available EIT systems.

Reference measurements were made with no conductive object and electrodes in the centre of the model. Measurements with a conductive object were made with the probe centred, then with the probe was shifted by 1, 5, and 10 percent of the tank radius in a randomized direction. The direction was randomized between trials but was consistent for each of the 1, 5 and 10 percent probe error models that were compared.

7.2.2 Movement correction

The movement correction jacobian was calculated using the methods presented by Gómez-Laberge and Adler (2008). In a model with a centred electrode probe and uniform conductivity, each of the four electrodes on the probe was perturbed by 0.001 m in each of the **x**, **y**, and **z** directions. A measurement was made for each electrode and each of the three dimensions of movement. The resulting measurements were divided by the perturbation amount. The measurements on each electrode (V_j) and from each direction of movement (**x**, **y**, and **z**) were combined to form the movement

jacobian (J_M) using the following equation from Gómez-Laberge and Adler (2008):

$$J_M = \left[\frac{\partial \mathbf{V}_j}{\partial \mathbf{x}}, \frac{\partial \mathbf{V}_j}{\partial \mathbf{y}}, \frac{\partial \mathbf{V}_j}{\partial \mathbf{z}} \dots \frac{\partial \mathbf{V}_n}{\partial \mathbf{x}}, \frac{\partial \mathbf{V}_n}{\partial \mathbf{y}}, \frac{\partial \mathbf{V}_n}{\partial \mathbf{z}} \right] \quad (7.1)$$

This movement jacobian was used in conjunction with the following single-step formulation for a reconstruction matrix presented by Adler *et al.* (1994). The regular impedance based reconstruction matrix is denoted by R_C and the jacobian for impedance based reconstruction is denoted by J_C .

$$R_C = \frac{[J_C]^T [W]}{[J_C][W][J_C]^T + [W]} \quad (7.2)$$

W in the above equation represents the Laplace prior (Soleimani *et al.*, 2006). Combining this formulation with the movement jacobian yields the following equation for the reconstruction matrix (R_M) (Soleimani *et al.*, 2006) where R_M denotes the reconstruction matrix for motion correction.

$$R_M = \frac{[J_C]^T [W]}{[J_C][W][J_C]^T + \mu[J_M][J_M]^T + [W]} \quad (7.3)$$

In the above equation μ represents the weighting of the motion correction. In this experiment the motion correction weighting was set to 100.

Combining equation (7.2) and equation (7.3) a reconstruction matrix to reconstruct exclusively the noise due to movement (R_N) in an image can be generated.

$$R_N = R_M - R_C \quad (7.4)$$

An image (X) is reconstructed using the measurements (b) and reconstruction matrix (R) as follows:

$$X = bR \quad (7.5)$$

Three images: X_C , X_M and X_N were reconstructed from their respective reconstruction matrix.

A new movement correction strategy had been built around the reconstructed image X_N . The noise due to exclusively motion is reconstructed into a 3D image, and the centre of mass of the positive change is located. This is assumed to be the direction of the motion. The amplitude of the electrode motion is estimated as half of the distance between the conductive artefact and the probe. This method is illustrated in figure 7.2. Images were reconstructed and displayed on a 64 by 64 grid to give a more accurate representation of the electrode position in the reconstructed image.

Using the probe location estimate calculated from X_N a new model was reconstructed with the probe repositioned to the reconstructed location. This model was then used to calculate a new reconstruction matrix using equation (7.3) with an updated jacobian based on the new probe location.

7.2.3 Image comparison

To simplify processing of the reconstructions, 10 images between the external electrode planes were averaged together to generate a 2D representation of the 3D data. This did not allow for analysis of movement in the vertical direction, but we did not

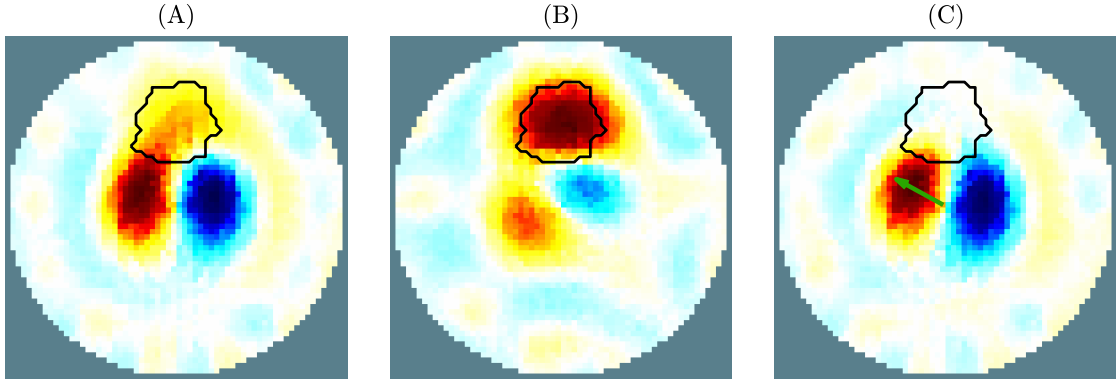


Figure 7.2: Three image reconstruction matrices were generated: one to calculate an image based only on the measurements (A), one that is able to reduce the impact of noise using a movement jacobian (B) and finally a reconstruction that reconstructs only the noise due to motion of the probe (C). The centre of mass of the conductive object is used to estimate the probe location and direction of movement. The green arrow indicates the calculated direction of movement (multiplied by 5 for visibility). The black line indicates the outline of the region of conductivity at the imaged plane. The images depict an average of 10 slices between the external electrode planes.

expect this to be a major contribution in real-world data. The reconstructed images were compared in two ways. First the accuracy of the reconstruction was evaluated by computing the Jaccard index between the actual and imaged boundaries of the conductive target. The imaged boundary was drawn at half the maximum value of the brightest object in the image. The second metric computed was a noise estimate. This was calculated as the amplitude of the imaged object relative to the amplitude of the entire image through the following equation:

$$N = 1 - \frac{A_{\text{object}}}{A_{\text{image}}} \quad (7.6)$$

Where A_{object} is the amplitude of the object, A_{image} is the amplitude of the image, and it is subtracted from 1 so that a noise estimate of 0 corresponds with all of the

image signal corresponding to the conductive target.

7.2.4 *In-vivo* recordings

Data were collected in three ewes during ventilation under general anesthetic using the SenTec EIT Pioneer Set. A skip 4 measurement pattern was used with an injection current of 3 mA at 30 kHz. Electrodes 29 to 32 were connected to the internal electrode probe.

7.2.4.1 Internal electrode probe design

The internal electrode probe consisted of four brass electrodes on a flexible tube. Each electrode was 1 cm in length and the spacing between electrodes was 2 cm. The electrodes were created from a brass sheet with a thickness of 2 mm that was bent to the shape of the flexible tubing and soldered to achieve a smooth surface. The electrodes were glued in place on the tube protruding 2 mm from probe surface. The tube radius was 0.5 cm. The constructed probe is shown in figure 7.3.

7.2.4.2 Electrode placment

The ewes were shaved and 28 silver-silver chloride electrodes were placed in 2 rows immedeately behind the front legs with 10 cm seperation and equal spacing around the thorax. The esophageal probe was alligned with the electrodes externally and the required depth was marked. The electrode probe was then coated in a conductive gel for lubraction and inserted in the esophagus up to the marked point.



Figure 7.3: A prototype of an internal electrode probe for esophageal use in an ovine model. Four brass electrodes are bent around the outside of a flexible tube designed for esophageal use. Edges of the electrodes are soldered and filed to be smooth. The electrodes are glued in place and wires run down the hollow centre of the tube to connect to the EIT system.

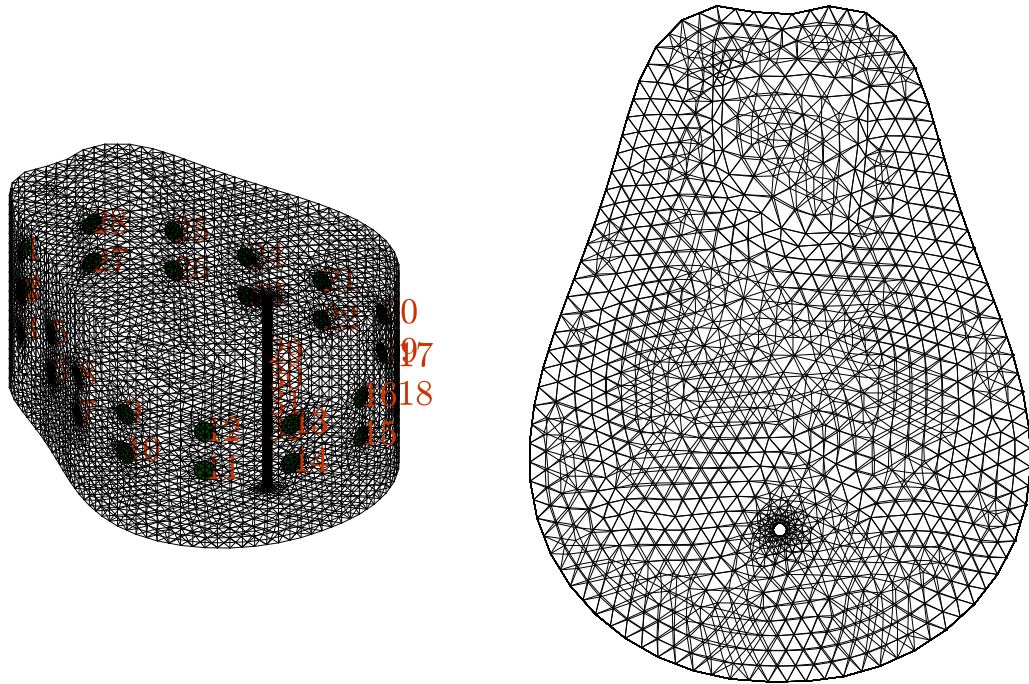


Figure 7.4: An internal electrode was added to an ovine model by creating a hole at desired probe location and added cylindrical electrodes at the desired heights. External electrodes were placed in a “square” electrode configuration on the boundary. Electrodes 1 to 28 were external and 29 to 32 were internal.

7.2.4.3 Ovine model

An internal probe was added to an ovine model by adapting the `mk_library_model` function in EIDORS (Adler *et al.*, 2017a). A circular region was added to the library geometry, and was extruded upwards to make a hole at the probe location. External electrodes were placed in a square pattern on the boundary, and internal electrodes were added as cylindrical objects in the central hole of the model. The resulting model is shown in figure 7.4.

7.2.4.4 Reconstruction

Images were reconstructed with 4 methods. The 3 methods discussed in section 7.2.2, and GREIT (Grychtol *et al.*, 2016).

7.2.4.5 Pulsatile amplitude

To measure the advantage provided by internal electrodes with regard to cardiosynchronous signal detection, a fast Fourier transform (FFT) of each signal was calculated. The cardiosynchronous component was selected as the highest amplitude near the recorded heart rate range of 65–80 bpm. This was divided by the amplitude of the ventilation frequency, which was the largest low-frequency amplitude in the FFT of the detrended signal. This was repeated for all 12 recordings across 3 animals.

7.3 Results

The following section presents the results for both simulation and *in-vivo* work.

7.3.1 Simulation

It was found that there was no measurable difference between simulations of models using spherical internal electrodes relative to the cylindrical electrodes. The results are presented using the cylindrical model to be consistent with the lamb models. The probe was moved in the $-y$ direction for figures and calculations in the results.

Figure 7.5 shows the result of the three reconstruction methods. The boundaries of the reconstructed and actual targets are outlined to highlight the performance.

Table 7.1: The jaccard index was calculated for each of the reconstructions in figure 7.5. Method A does not use any motion correction. Method B incorporates the movement jacobian, and method C uses the new probe location correction technique. For jaccard index, a score closer to one is better.

Movement (% of radius)	Method A	Method B	Method C
1	0.732	0.809	0.802
5	0.038	0.654	0.808
10	0.003	0.227	0.577

Table 7.2: Noise estimate values calculated for each of the reconstructions in figure 7.5. Method A does not use any motion correction. Method B incorporates the movement jacobian, and method C uses the new probe location correction technique. For the noise estimates a lower score is better, a score of zero indicates all image changes occur within the target boundary, and a score less than one indicates most of the changes in the image are due to the identified target.

Movement (% of radius)	Method A	Method B	Method C
1	0.588	0.537	0.529
5	0.781	0.669	0.618
10	0.777	0.747	0.718

The new method is able to reconstruct the correct location with motion of up to 10 % of the tank boundary between measurements. The jaccard index and noise estimate for each method are presented below in table 7.1 and table 7.2.

For movement of one percent of the tank boundary motion correction using only the movement jacobian was roughly equivalent to the probe location correction algorithm. Across all other scenarios, the probe location correction algorithm achieved a higher jaccard score. Across all scenarios the new technique to correct for motion had the lowest noise estimate score.

When looking at the reconstructions using the three methods, the new probe correction technique reconstructed the target as the brightest object in all scenarios. With no motion correction, the target was identified correctly only in the first

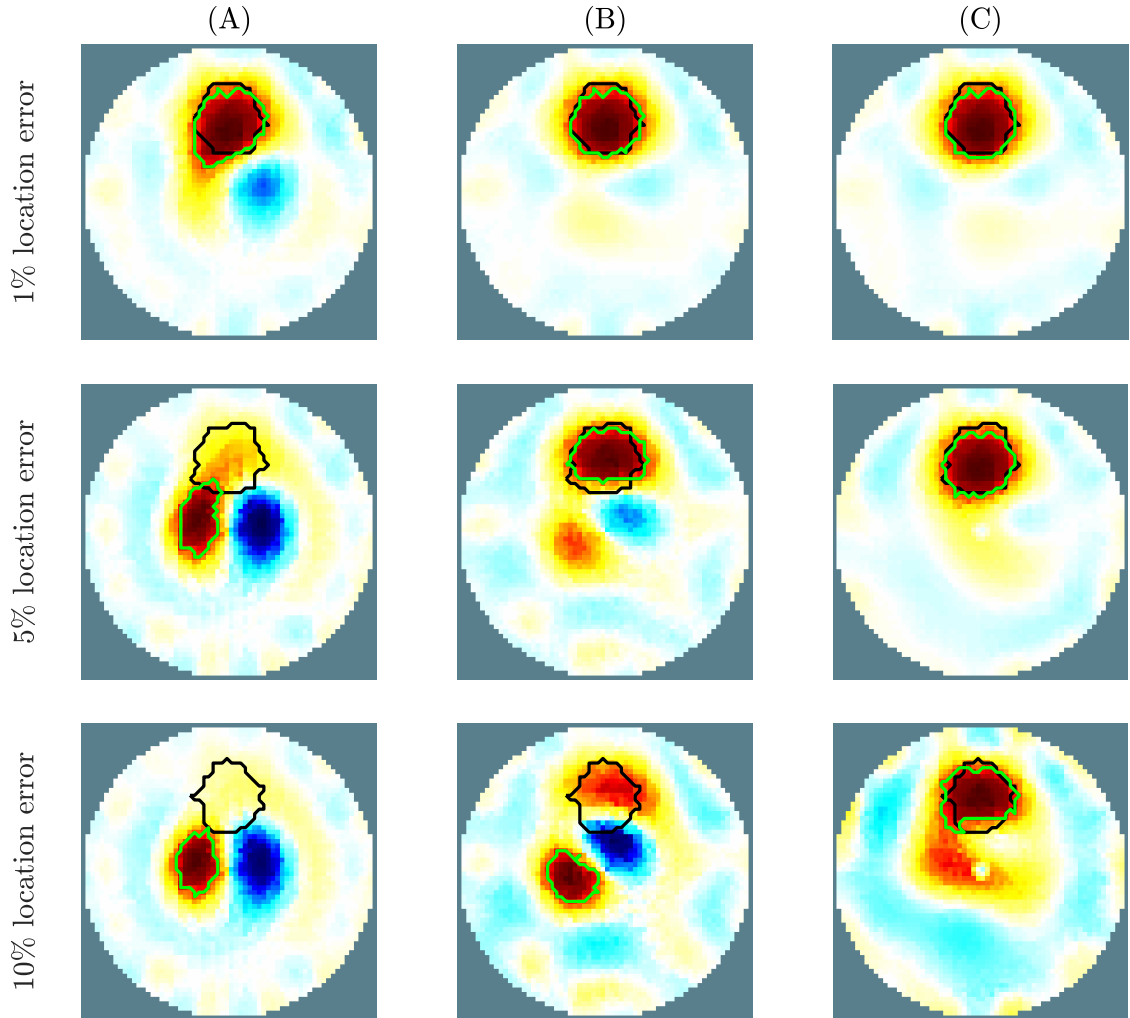


Figure 7.5: The results of the probe location correction are presented. The rows from top to bottom show results with 1, 5, and 10% shifts in probe location relative to the tank radius. Column (A) shows the results of the reconstruction with no motion correction, column (B) shows the method using the movement jacobian, and column (C) shows the results of the new probe location correction method. The green outline indicates the reconstructed boundary of the conductive target, and the black outline is the actual boundary.

scenario. Using the movement jacobian reconstruction method, the target was correctly identified when the probe was moved one or five percent of the tank radius.

7.3.2 *In-vivo*

Recordings in each of the three ewes are presented in this section. Reconstructions with internal electrodes are shown in figure 7.6 for a selected breath during a baseline recording in each subject.

Reconstructions with movement correction applied to the internal electrodes appear to show a slight improvement in lung distinguishability and a slight reduction in noise surrounding the probe. There is limited difference between the two methods accounting for motion on the electrode.

The ratio of cardiosynchronous to respiratory rate impedance signals is shown below in figure 7.7. The results show a higher amplitude of the cardiopulmonary signal relative to ventilation when internal electrodes are used.

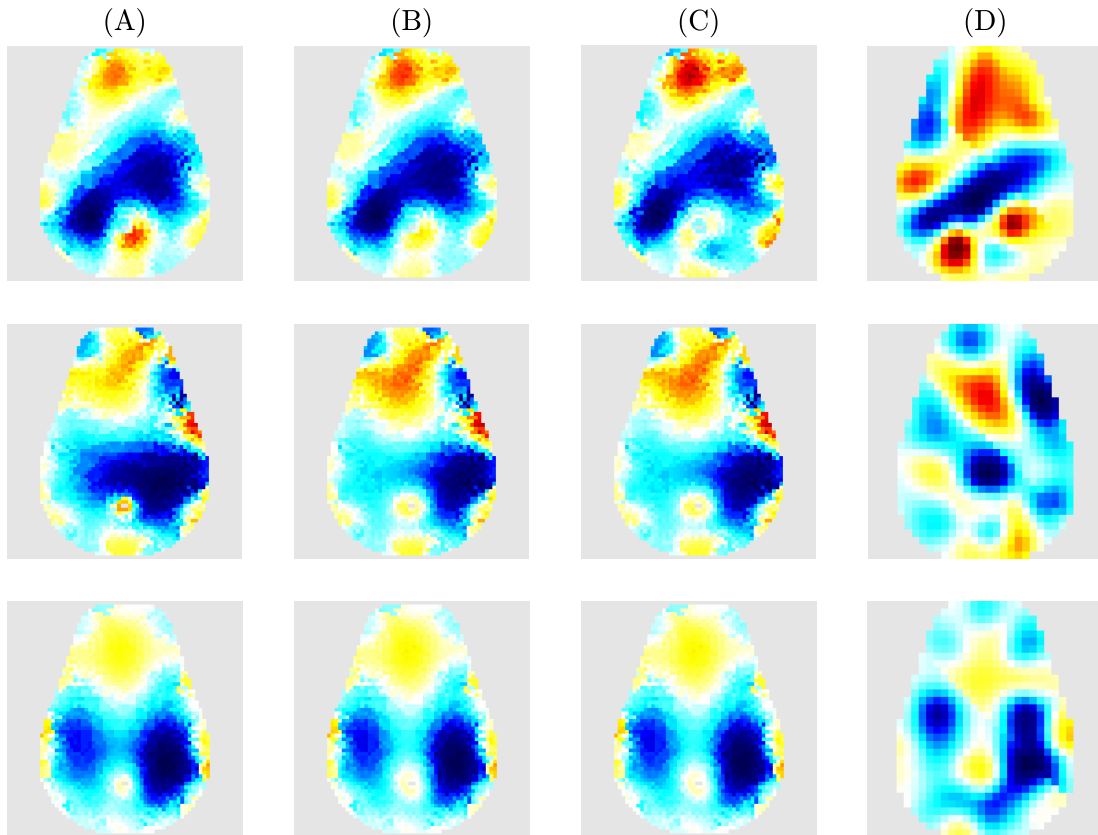


Figure 7.6: Preliminary results on 3 ewes reconstructed from a single, selected breath. Each column represents a reconstruction method. Column (A) uses no motion correction, column (B) uses the movement jacobian and column (C) uses the new method for electrode location correction. Column (D) contains reconstructions using the GREIT 3D algorithm. The number of pixels is different between images due to the methodology of probe localization and the limitations of GREIT.

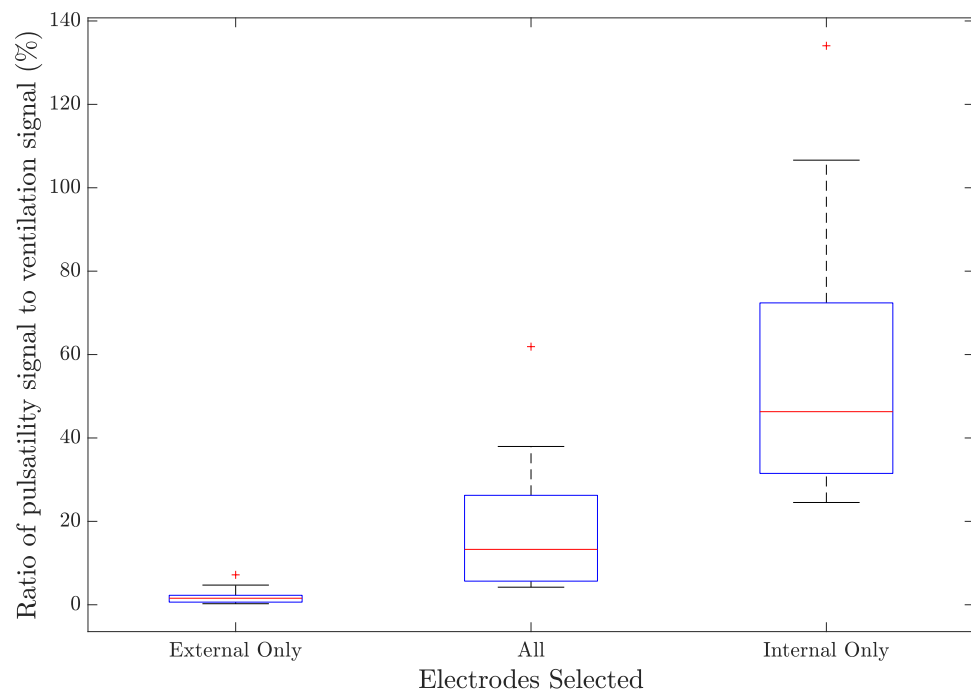


Figure 7.7: The cardiosynchronous signal component was divided by the ventilation frequency component to compare the detectability of the pulsatile changes. The ratio was compared for measurements using only external electrodes, all electrodes, and internal electrodes only.

7.4 Discussion

This chapter aimed to provide a technique to reduce noise due to motion on internal electrodes when reconstructing images in 3D and demonstrate the noise reduction technique *in-vivo*. The new technique to reconstruct images in the presence of motion on internal electrodes reconstructed an image of a conductive target more accurately and with less noise in the surrounding image. *In-vivo* reconstructions showed a slight improvement in lung distinguishability when correcting for motion artefacts on internal electrodes compared to methods without this correction including GREIT. Results in 3D also confirmed results from a 2D study in a porcine model showing an increased cardiosynchronous component on the internal electrode measurements (Czaplik *et al.*, 2014).

It was found that GREIT performed poorly when reconstructing data with internal electrodes. The figures of merit for GREIT designed and optimized to work with external electrodes where sensitivity is low in the centre of the model and high at the edges (Adler *et al.*, 2009). An adaptation to GREIT that is able to account for internal electrodes and motion of an internal probe is planned as a continuation of this project.

Two types of internal electrodes were modelled in this chapter. One with spherical internal electrodes and one with a hollow probe and cylindrical electrodes. Meshing and creating internal electrodes can be challenging due to limited meshing tools for using internal electrodes with EIT and the method of adding internal probes to anatomical models using a hollow region in the centre of the model was created for this project. Code to generate this model with internal electrodes is planned to be

included in a future release of EIDORS.

The noise estimate score calculations were not perfect representations of the noise in the images due to the way the reconstructed object was identified. Since the brightest object was always identified as the object, the noise estimate was artificially low in some cases. Comparing the amplitude of changes contained within the true object boundaries could be a better metric of the noise present in the image, but this would also be dependent on the accuracy of reconstruction and would have favoured the method that reconstructed the object most accurately. The boundary of the true target also changes due to differences in element locations as the probe is moved, so the comparison would not be consistent across all probe movement states. Despite this limitation, the noise estimate does help to quantify noise seen in the images for each technique. The new method performed better than existing techniques across all situations according to the computed noise metrics.

In simulated cases of less than one percent error in probe location, very little difference in reconstruction accuracy between the two motion correction algorithms was detected. Despite this, a slight reduction in background noise in the image was observed.

Despite the improvements to reconstruction accuracy and noise reduction using the new method, there are several limitations to its use. The most significant is the increased modelling time required. This method required an extra model, and inverse solution compared to the single step solutions. For simple models such as a tank the added time difference is small, but for complex models this could increase reconstruction time drastically. When several frames are reconstructed each

requires a unique model with a modified probe location increasing the time required significantly. To reduce the reconstruction time, correcting the model only when the probe location error is greater than one percent of the model radius may be helpful. At this level of movement, the benefits of the probe localization technique are not substantial. Additionally in the images presented probe movement did not appear to be significant. It is not yet clear what the typical movement of the electrode probe is expected to be in the esophagus.

Previous research has also reconstructed for motion direction directly using the movement jacobian (Boyle, 2016; Gómez-Laberge and Adler, 2008; Soleimani *et al.*, 2006). This technique for electrode estimation has not been implemented using internal electrodes for this research, but a comparison between the two electrode position estimation techniques it required for complete validation of the demonstrated method.

Previous studies with internal electrodes showed cases where contact impedance of the probe was inadequate for electrodes placed on the breathing and feeding tubes (Czaplik *et al.*, 2014). The electrodes used were shown to have a good contact impedance on the SenTec Pioneer Set interface, but the current design protrudes slightly from the tube and may be challenging to integrate into a clinical esophageal or tracheal tube.

Sanchez *et al.* (2013) used an array of internal electrodes in the lung during biopsy procedures, and suggested that the increased proximity to the tissue could allow more physiological information to be obtained. A more complete evaluation is required to measure the benefits of internal electrodes in 3D compared to typi-

cal external configurations. The previously seen lung distinguishability and larger cardiosynchronous signal amplitude found in 2D (Czaplik *et al.*, 2014) have been repeated with this 3D configuration, but it is still unclear to what degree these signal changes may be useful.

Increased lung separability may be useful for determining the difference between right and left lung ventilation, which can be used to quantify ventilation performance (Sage *et al.*, 2018) and is an important step in detecting ventilation and perfusion mismatch (Kircher *et al.*, 2021; Leonhardt and Lachmann, 2012; Stowe *et al.*, 2019). Increased sensitivity to pulsatile flow may also help to improve measures of cardiopulmonary activity where detecting pulsatile flow and motion in specific regions of a model is desired (Braun *et al.*, 2018a; Proen  a *et al.*, 2020).

7.5 Summary

Probe displacement introduces significant errors when using reconstruction algorithms that do not account for movement. This chapter presents a new technique designed to reduce the effect of probe motion. This new method was found to outperform existing methods with regards to reconstruction accuracy and background noise in simulations on a tank model. Internal electrodes in conjunction with a 3D external configuration were also used *in-vivo* to measure ventilation. Images of breaths across three subjects showed an improvement to lung distinguishability when correcting for motion, and the average ratio of cardiosynchronous to pulmonary signal was increased when using internal electrodes.

Chapter 8

Conclusion

8.1 Summary of Findings

Note - it is possible that measurements on the internal electrode probe should be used only for identification of the pulsatile component and not as part of the reconstructed images

Limitations of the lamb model hear tlocation and whatnoT

8.2 Future Work

Bibliography

- Abe, T., Madotto, F., Pham, T., Nagata, I., Uchida, M., Tamiya, N., Kurahashi, K., Bellani, G., & Laffey, J. G. (2018). Epidemiology and patterns of tracheostomy practice in patients with acute respiratory distress syndrome in ICUs across 50 countries. *Critical Care*, 22(1).
- Adler, A., Boyle, A., Crabb, M. G., Grychtol, B. L., Lionheart, W. R. B., Tregidgo, H. F. J., & Yerworth, R. (2017a). EIDORS version 3.9. *Proc. 18th Int. Conf. on Biomed. Applications of EIT*.
- Adler, A., & Guardo, R. (1996). Electrical impedance tomography: Regularized imaging and contrast detection. *IEEE Transactions on Medical Imaging*, 15(2), 170–179.
- Adler, A., Guardo, R., & Berthiaume, Y. (1994). Impedance imaging of lung ventilation: Do we need to account for chest expansion? *Proceedings of 16th Annual International Conference of the IEEE Engineering in Medicine and Biology Society*, 1, 534–535 vol.1.
- Adler, A., Amato, M. B., Arnold, J. H., Bayford, R., Bodenstein, M., Böhm, S. H., Brown, B. H., Frerichs, I., Stenqvist, O., Weiler, N., & Wolf, G. K. (2012).

- Whither lung EIT: Where are we, where do we want to go and what do we need to get there? *Physiol. Meas.*, 33(5), 679–694.
- Adler, A., Arnold, J. H., Bayford, R., Borsic, A., Brown, B., Dixon, P., Faes, T. J. C., Frerichs, I., Gagnon, H., Gärber, Y., Grychtol, B., Hahn, G., Lionheart, W. R. B., Malik, A., Patterson, R. P., Stocks, J., Tizzard, A., Weiler, N., & Wolf, G. K. (2009). GREIT: A unified approach to 2d linear EIT reconstruction of lung images. *Physiol. Meas.*, 30(6), S35–S55.
- Adler, A., & Boyle, A. (2017). Electrical impedance tomography: Tissue properties to image measures. *IEEE Transactions on Biomedical Engineering*, 64(11), 2494–2504.
- Adler, A., Grychtol, B., & Bayford, R. (2015). Why is EIT so hard, and what are we doing about it? *Physiol. Meas.*, 36(6), 1067–1073.
- Adler, A., & Lionheart, W. R. B. (2006). Uses and abuses of EIDORS: An extensible software base for EIT. *Physiol. Meas.*, 27(5), S25–S42.
- Adler, A., Proença, M., Braun, F., & Solà, J. (2017b). Origins of cardiosynchronous signals in EIT. *EIT 2017*.
- Aljizeeri, A., Cocker, M. S., & Chow, B. J. W. (2013). CT vs SPECT: CT is the first-line test for the diagnosis and prognosis of stable coronary artery disease. *J. Nucl. Cardiol.*, 20(3), 465–472.
- Allaud, L., & Martin, M. (1977). *Schlumberger: The history of a technique*. Wiley.
- Ashbaugh, D. G., Bigelow, D. B., Petty, T. L., & Levine, B. E. (1967). Acute respiratory distress in adults. *Lancet*, 2(7511), 319–323.

- Axel, L. (1980). Cerebral blood flow determination by rapid-sequence computed tomography: Theoretical analysis. *Radiology*, 137(3), 679–686.
- Barber, D. C., & Brown, B. H. (1984). Applied potential tomography. *J. Phys. E: Sci. Instrum.*, 17(9), 723–733.
- Barker, R., Ashby, E. L., Wellington, D., Barrow, V. M., Palmer, J. C., Kehoe, P. G., Esiri, M. M., & Love, S. (2014). Pathophysiology of white matter perfusion in alzheimer's disease and vascular dementia. *Brain*, 137(5), 1524–1532.
- Bartocci, M., Serra, G., Basano, L., Canepa, F., & Ottonello, P. (1999). Cerebral blood-flow monitor for use in neonatal intensive care units. *Computer Methods and Programs in Biomedicine*, 59(1), 61–73.
- Bates, J. H. T., & Smith, B. J. (2018). Ventilator-induced lung injury and lung mechanics. *Ann Transl Med*, 6(19), 378.
- Bhuyan, U., Peters, A. M., Gordon, I., Davies, H., & Helms, P. (1989). Effects of posture on the distribution of pulmonary ventilation and perfusion in children and adults. *Thorax*, 44(6), 480–484.
- Borges, J. B., Suarez-Sipmann, F., Bohm, S. H., Tusman, G., Melo, A., Maripuu, E., Sandström, M., Park, M., Costa, E. L. V., Hedenstierna, G., & Amato, M. (2012). Regional lung perfusion estimated by electrical impedance tomography in a piglet model of lung collapse. *Journal of Applied Physiology*, 112(1), 225–236.

- Boyle, A., Crabb, M. G., Jehl, M., Lionheart, W. R. B., & Adler, A. (2017). Methods for calculating the electrode position jacobian for impedance imaging. *Physiol. Meas.*, 38(3), 555–574.
- Boyle, A. (2016). *Geophysical applications of electrical impedance tomography* (Doctoral dissertation). Carleton University. Ottawa, Canada.
- Boyle, A., & Adler, A. (2011). The impact of electrode area, contact impedance and boundary shape on EIT images. *Physiol. Meas.*, 32(7), 745–754.
- Braun, F., Proen  a, M., Adler, A., Riedel, T., Thiran, J.-P., & Sol  , J. (2018a). Accuracy and reliability of noninvasive stroke volume monitoring via ECG-gated 3d electrical impedance tomography in healthy volunteers. *PLoS One*, 13(1), e0191870.
- Braun, F., Proen  a, M., Lemay, M., Bertschi, M., Adler, A., Thiran, J.-P., & Sol  , J. (2018b). Limitations and challenges of EIT-based monitoring of stroke volume and pulmonary artery pressure. *Physiol. Meas.*, 39(1), 014003.
- Brown, B. H. (2003). Electrical impedance tomography (EIT): A review. *J Med Eng Technol*, 27(3), 97–108.
- Brown, B. H., Leathard, A., Sinton, A., McArdle, F. J., Smith, R. W. M., & Barber, D. C. (1992). Blood flow imaging using electrical impedance tomography. *Clin. Phys. Physiol. Meas.*, 13, 175–179.
- Cheney, M., Isaacson, D., Newell, J. C., Simske, S., & Goble, J. (1990). NOSER: An algorithm for solving the inverse conductivity problem. *International Journal of Imaging Systems and Technology*, 2(2), 66–75.

- Cohen, J. (1977). *Statistical power analysis for the behavioral sciences* (Revised edition.). Academic Press.
- Coulombe, N., Gagnon, H., Marquis, F., Skrobik, Y., & Guardo, R. (2005). A parametric model of the relationship between EIT and total lung volume. *Physiol. Meas.*, 26(4), 401–411.
- Czaplik, M., Antink, C. H., Rossaint, R., & Leonhardt, S. (2014). Application of internal electrodes to the oesophageal and tracheal tube in an animal trial: Evaluation of its clinical and technical potentiality in electrical impedance tomography. *Journal of Clinical Monitoring and Computing*, 28(3), 299–308.
- Deibele, J. M., Luepschen, H., & Leonhardt, S. (2008). Dynamic separation of pulmonary and cardiac changes in electrical impedance tomography. *Physiol. Meas.*, 29(6), S1–S14.
- Denaï, M. A., Mahfouf, M., Mohamad-Samuri, S., Panoutsos, G., Brown, B. H., & Mills, G. H. (2010). Absolute electrical impedance tomography (aEIT) guided ventilation therapy in critical care patients: Simulations and future trends. *IEEE Transactions on Information Technology in Biomedicine*, 14(3), 641–649.
- Dougall, N. J., Bruggink, S., & Ebmeier, K. P. (2004). Systematic review of the diagnostic accuracy of 99mtc-HMPAO-SPECT in dementia. *The American journal of geriatric psychiatry*, 12(6), 554–570.

- Duggal, A., Ganapathy, A., Ratnapalan, M., & Adhikari, N. K. (2015). Pharmacological treatments for acute respiratory distress syndrome: Systematic review. *Minerva Anestesiol*, 81(5), 567–588.
- Ericsson, E., Tesselaar, E., & Sjöberg, F. (2016). Effect of electrode belt and body positions on regional pulmonary ventilation- and perfusion-related impedance changes measured by electric impedance tomography. *PLoS One*, 11(6), e0155913.
- Essig, M., Shiroishi, M. S., Nguyen, T. B., Saake, M., Provenzale, J. M., Enterline, D., Anzalone, N., Dörfler, A., Rovira, Å., Wintermark, M., & Law, M. (2013). Perfusion MRI: The five most frequently asked technical questions. *AJR Am J Roentgenol*, 200(1), 24–34.
- Eyüboğlu, B. M., Brown, B. H., Barber, D. C., & Seager, A. D. (1987). Localisation of cardiac related impedance changes in the thorax. *Clin. Phys. Physiol. Meas.*, 8(4), 167–173.
- Eyüboğlu, B., Brown, B., & Barber, D. (1989). In vivo imaging of cardiac related impedance changes. *IEEE Engineering in Medicine and Biology Magazine*, 8(1), 39–45.
- Fagerberg, A., Stenqvist, O., & Åneman, A. (2009). Electrical impedance tomography applied to assess matching of pulmonary ventilation and perfusion in a porcine experimental model. *Critical Care*, 13(2), R34.
- Fedorov, A., Beichel, R., Kalpathy-Cramer, J., Finet, J., Fillion-Robin, J.-C., Pujol, S., Bauer, C., Jennings, D., Fennessy, F., Sonka, M., Buatti, J., Aylward, S.,

- Miller, J. V., Pieper, S., & Kikinis, R. (2012). 3d slicer as an image computing platform for the quantitative imaging network. *Magn Reson Imaging*, 30(9), 1323–1341.
- Ferrario, D., Grychtol, B., Adler, A., Sola, J., Bohm, S. H., & Bodenstein, M. (2012). Toward morphological thoracic EIT: Major signal sources correspond to respective organ locations in CT. *IEEE Transactions on Biomedical Engineering*, 59(11), 3000–3008.
- Foster, K. R., & Lukaski, H. C. (1996). Whole-body impedance—what does it measure? *The American Journal of Clinical Nutrition*, 64(3), 388S–396S.
- Frerichs, I., Hinz, J., Herrmann, P., Weisser, G., Hahn, G., Quintel, M., & Hellige, G. (2002). Regional lung perfusion as determined by electrical impedance tomography in comparison with electron beam CT imaging. *IEEE Transactions on Medical Imaging*, 21(6), 646–652.
- Frerichs, I., Amato, M. B. P., Kaam, A. H. v., Tingay, D. G., Zhao, Z., Grychtol, B., Bodenstein, M., Gagnon, H., Böhm, S. H., Teschner, E., Stenqvist, O., Mauri, T., Torsani, V., Camporota, L., Schibler, A., Wolf, G. K., Gommers, D., Leonhardt, S., Adler, A., & Group, T. s. (2017). Chest electrical impedance tomography examination, data analysis, terminology, clinical use and recommendations: Consensus statement of the TRanslational EIT development stuDy group. *Thorax*, 72(1), 83–93.

- Frerichs, I., & Becher, T. (2019). Chest electrical impedance tomography measures in neonatology and paediatrics—a survey on clinical usefulness. *Physiol. Meas.*, *40*(5), 054001.
- Fu, S. X., Lai, K. L., Si, Y. T., Xu, L., Xiao, M. D., & Gang, A. (1996). Study of the safe threshold of apneic period in children during anesthesia induction. *Journal of Clinical Anesthesia*, *8*(7), 568–574.
- Gandev, G., Rao, H., Rashid, S., Kanagarajan, K., & Gupta, K. (2005). Comparison between perfusion lung scan and ventilation-perfusion lung scan in patients with pulmonary embolism. *Chest*, *128*(4), 406S–406S.
- Gaw, R. L. (2010). *The effect of red blood cell orientation on the electrical impedance of pulsatile blood with implications for impedance cardiography* (Doctoral dissertation). Queensland University of Technology.
- Geddes, L. A., & Baker, L. E. (1967). The specific resistance of biological material—a compendium of data for the biomedical engineer and physiologist. *Med. & biol. Engng.*, *5*(3), 271–293.
- Geuzaine, C., & Remacle, J.-F. (2009). Gmsh: A 3-d finite element mesh generator with built-in pre- and post-processing facilities. *International Journal for Numerical Methods in Engineering*, *79*(11), 1309–1331.
- Gómez-Laberge, C., & Adler, A. (2007). Direct calculation of the electrode movement jacobian for 3d EIT. In H. Scharfetter & R. Merwa (Eds.), *13th international conference on electrical bioimpedance and the 8th conference on electrical impedance tomography* (pp. 364–367). Springer.

- Gómez-Laberge, C., & Adler, A. (2008). Direct EIT jacobian calculations for conductivity change and electrode movement. *Physiol. Meas.*, 29(6), S89–S99.
- Gordon, J. W. (1877). Certain molar movements of the human body produced by the circulation of the blood. *J Anat Physiol*, 11, 533–536.
- Grychtol, B., & Adler, A. (2013). FEM electrode refinement for electrical impedance tomography. *2013 35th Annual International Conference of the IEEE Engineering in Medicine and Biology Society (EMBC)*, 6429–6432.
- Grychtol, B., Lionheart, W. R. B., Bodenstein, M., Wolf, G. K., & Adler, A. (2012). Impact of model shape mismatch on reconstruction quality in electrical impedance tomography. *IEEE Transactions on Medical Imaging*, 31(9), 1754–1760.
- Grychtol, B., Müller, B., & Adler, A. (2016). 3d EIT image reconstruction with GREIT. *Physiol. Meas.*, 37(6), 785–800.
- Halter, R., Hartov, A., & Paulsen, K. (2008). Imaging forearm blood flow with pulse-ox gated electrical impedance tomography. *2008 30th Annual International Conference of the IEEE Engineering in Medicine and Biology Society*, 1192–1195.
- Hochhausen, N., Orschulik, J., Follmann, A., Santos, S. A., Dohmeier, H., Leonhardt, S., Rossaint, R., & Czaplik, M. (2019). Comparison of two experimental ARDS models in pigs using electrical impedance tomography. *PLoS ONE*, 14(11), e0225218.

- Holder, D. S. (1992). Electrical impedance tomography (EIT) of brain function. *Brain Topogr*, 5(2), 87–93.
- Holder, D. (Ed.). (2004). *Electrical impedance tomography: Methods, history and applications*. CRC Press.
- Hough, J., Trojman, A., & Schibler, A. (2016). Effect of time and body position on ventilation in premature infants. *Pediatr Res*, 80(4), 499–504.
- Hsu, Y.-L., Tien, A.-J., Chang, M.-Y., Chang, H.-T., Möller, K., Frerichs, I., & Zhao, Z. (2017). Regional ventilation redistribution measured by electrical impedance tomography during spontaneous breathing trial with automatic tube compensation. *Physiol. Meas.*, 38(6), 1193–1203.
- Humphreys, S., Pham, T. M., Stocker, C., & Schibler, A. (2011). The effect of induction of anesthesia and intubation on end-expiratory lung level and regional ventilation distribution in cardiac children. *Pediatric Anesthesia*, 21(8), 887–893.
- Hur, S., Bauer, A., McMillan, N., Krupinski, E. A., & Kuo, P. H. (2014). Optimizing the ventilation–perfusion lung scan for image quality and radiation exposure. *Journal of Nuclear Medicine Technology*, 42(1), 51–54.
- International Electrotechnical Commission, (2021). *IEC 60601-1*. International Electrotechnical Commission.
- Jackson, A., Buckley, D. L., & Parker, G. J. M. (2005). *Dynamic contrast-enhanced magnetic resonance imaging in oncology* (1st ed. 2005.). Springer Berlin Heidelberg.

- Kim, C.-S., Ober, S. L., McMurtry, M. S., Finegan, B. A., Inan, O. T., Mukkamala, R., & Hahn, J.-O. (2016). Ballistocardiogram: Mechanism and potential for unobtrusive cardiovascular health monitoring. *Sci Rep*, 6, 31297.
- Kircher, M., Elke, G., Stender, B., Hernández Mesa, M., Schuderer, F., Dössel, O., Fuld, M. K., Halaweish, A. F., Hoffman, E. A., Weiler, N., & Frerichs, I. (2021). Regional lung perfusion analysis in experimental ARDS by electrical impedance and computed tomography. *IEEE Transactions on Medical Imaging*, 40(1), 251–261.
- Koenig, M., Klotz, E., Luka, B., Venderink, D. J., Spittler, J. F., & Heuser, L. (1998). Perfusion CT of the brain: Diagnostic approach for early detection of ischemic stroke. *Radiology*, 209(1), 85–93.
- Konstas, A. A., Goldmakher, G. V., Lee, T.-Y., & Lev, M. H. (2009). Theoretic basis and technical implementations of CT perfusion in acute ischemic stroke, part 1: Theoretic basis. *American Journal of Neuroradiology*, 30(4), 662–668.
- Koretsky, A. P. (2012). Early development of arterial spin labeling to measure regional brain blood flow by MRI. *NeuroImage*, 62(2), 602–607.
- Larsson, J. (2007). Electromagnetics from a quasistatic perspective. *American Journal of Physics*, 75(3), 230–239.
- Leathard, A. D., Brown, B. H., Campbell, J., Zhang, F., Morice, A. H., & Tayler, D. (1994). A comparison of ventilatory and cardiac related changes in EIT images of normal human lungs and of lungs with pulmonary emboli. *Physiol. Meas.*, 15(2), A137–A146.

- Leonhardt, S., & Lachmann, B. (2012). Electrical impedance tomography: The holy grail of ventilation and perfusion monitoring? *Intensive Care Med*, 38(12), 1917–1929.
- Lozano, A., Rosell, J., & Pallas-Areny, R. (1995). Errors in prolonged electrical impedance measurements due to electrode repositioning and postural changes. *Physiol. Meas.*, 16(2), 121–130.
- McAdams, E. T., & Jossinet, J. (1995). Tissue impedance: A historical overview. *Physiol. Meas.*, 16(3), A1–A13.
- Mendis, S., Puska, P., & Norrving, B. (2011). *Global atlas on cardiovascular disease prevention and control*. World Health Organization.
- Mettler, F. A., & Guiberteau, M. J. (2006). *Essentials of nuclear medicine imaging* (5th ed.). Saunders/Elsevier.
- Miles, K. A., Hayball, M., Dixon, A. K., Miles, K. A., Hayball, M., & Dixon, A. K. (1991). Colour perfusion imaging: A new application of computed tomography. *The Lancet*, 337(8742), 643–645.
- Moens, Y., Schramel, J. P., Tusman, G., Ambrisko, T. D., Solà, J., Brunner, J. X., Kowalczyk, L., & Böhm, S. H. (2014). Variety of non-invasive continuous monitoring methodologies including electrical impedance tomography provides novel insights into the physiology of lung collapse and recruitment – case report of an anaesthetized horse. *Veterinary Anaesthesia and Analgesia*, 41(2), 196–204.

- Mortensen, J., & Berg, R. M. G. (2019). Lung scintigraphy in COPD. *Seminars in Nuclear Medicine*, 49(1), 16–21.
- Nakazato, R., Tamarappoo, B. K., Kang, X., Wolak, A., Kite, F., Hayes, S. W., Thomson, L. E. J., Friedman, J. D., Berman, D. S., & Slomka, P. J. (2010). Quantitative upright-supine high-speed SPECT myocardial perfusion imaging for detection of coronary artery disease: Correlation with invasive coronary angiography. *The Journal of Nuclear Medicine*, 51(11), 1724–31.
- Nasehi Tehrani, J., Jin, C., & McEwan, A. L. (2012a). Modelling of an oesophageal electrode for cardiac function tomography. *Computational and Mathematical Methods in Medicine*, 2012, e585786.
- Nasehi Tehrani, J., Oh, T. I., Jin, C., Thiagalingam, A., & McEwan, A. (2012b). Evaluation of different stimulation and measurement patterns based on internal electrode: Application in cardiac impedance tomography. *Computers in Biology and Medicine*, 42(11), 1122.
- Nguyen, D. T., Bhaskaran, A., Chik, W., Barry, M. A., Pouliopoulos, J., Kosobrodov, R., Jin, C., Oh, T. I., Thiagalingam, A., & McEwan, A. L. (2015). Perfusion redistribution after a pulmonary-embolism-like event with contrast enhanced EIT. *Physiol. Meas.*, 36(6), 1297–1309.
- Nguyen, D. T., Jin, C., Thiagalingam, A., & McEwan, A. L. (2012). A review on electrical impedance tomography for pulmonary perfusion imaging. *Physiol. Meas.*, 33(5), 695–706.

- Nguyen, D. M., Andersen, T., Qian, P., Barry, T., & McEwan, A. (2020). Electrical impedance tomography for monitoring cardiac radiofrequency ablation: A scoping review of an emerging technology. *Medical Engineering & Physics*, 84, 36–50.
- Nissinen, A., Heikkinen, L. M., Kolehmainen, V., & Kaipio, J. P. (2009). Compensation of errors due to discretization, domain truncation and unknown contact impedances in electrical impedance tomography. *Meas. Sci. Technol.*, 20(10), 105504.
- Nyboer, J., Bagno, S., Barnett, A., & Halsey, R. H. (1970). Impedance cardiograms and differentiated-impedance cardiograms—the electrical impedance changes of the heart in relation to electrocardiograms and heart sounds*. *Annals of the New York Academy of Sciences*, 170(2), 421–436.
- Osteebe, A. (1998). Rank-deficient and discrete ill-posed problems: Numerical aspects of linear inversion. *The American Mathematical Monthly*, 105(5), 491.
- Pappano, A. J., & Wier, W. G. (2019). *Cardiovascular physiology* (11th ed.). Elsevier.
- Patterson, R. P. (2010). Impedance cardiography: What is the source of the signal? *J. Phys.: Conf. Ser.*, 224, 012118.
- Patterson, R. P., Zhang, J., Mason, L. I., & Jerosch-Herold, M. (2001). Variability in the cardiac EIT image as a function of electrode position, lung volume and body position. *Physiol. Meas.*, 22(1), 159–166.
- Petty, T. L. (2001). In the cards was ARDS. *Am J Respir Crit Care Med*, 163(3), 602–603.

- Pham, T., & Rubenfeld, G. D. (2017). Fifty years of research in ARDS. the epidemiology of acute respiratory distress syndrome. a 50th birthday review. *Am J Respir Crit Care Med, 195*(7), 860–870.
- Pilkington, T., Eyüboğlu, M., & Wolf, P. (1989). Utilization of esophageal reference electrode to enhance impedance imaging. *Images of the Twenty-First Century. Proceedings of the Annual International Engineering in Medicine and Biology Society, 482* vol.2—.
- PIOPED-Investigators. (1990). Value of the ventilation/perfusion scan in acute pulmonary embolism: Results of the prospective investigation of pulmonary embolism diagnosis (PIOPED). *JAMA, 263*(20), 2753–2759.
- Pollock, J. D., & Makaryus, A. N. (2021). Physiology, cardiac cycle. *Physiology, cardiac cycle*. StatPearls Publishing.
- Polydorides, N., & McCann, H. (2002). Electrode configurations for improved spatial resolution in electrical impedance tomography. *Meas. Sci. Technol., 13*(12), 1862–1870.
- Proença, M., Braun, F., Lemay, M., Solà, J., Adler, A., Riedel, T., Messerli, F. H., Thiran, J.-P., Rimoldi, S. F., & Rexhaj, E. (2020). Non-invasive pulmonary artery pressure estimation by electrical impedance tomography in a controlled hypoxemia study in healthy subjects. *Sci Rep, 10*(1), 21462.
- Proença, M., Braun, F., Rapin, M., Solà, J., Adler, A., Grychtol, B., Bohm, S. H., Lemay, M., & Thiran, J.-P. (2015). Influence of heart motion on cardiac out-

- put estimation by means of electrical impedance tomography: A case study. *Physiol. Meas.*, 36(6), 1075–1091.
- Proença, M., Braun, F., Solà, J., Thiran, J.-p., & Lemay, M. (2017). Noninvasive pulmonary artery pressure monitoring by EIT: A model-based feasibility study. *Medical and Biological Engineering and Computing*, 55(6), 949–963.
- Prvulovich, E. M., & Bomanji, J. B. (1998). The role of nuclear medicine in clinical investigation. *BMJ*, 316(7138), 1140–1146.
- Reifferscheid, F., Elke, G., Pulletz, S., Gawelczyk, B., Lautenschläger, I., Steinfath, M., Weiler, N., & Frerichs, I. (2011). Regional ventilation distribution determined by electrical impedance tomography: Reproducibility and effects of posture and chest plane. *Respirology*, 16(3), 523–531.
- Sage, M., Nadeau, M., Forand-Choinière, C., Mousseau, J., Vandamme, J., Berger, C., Tremblay-Roy, J.-S., Tissier, R., Micheau, P., & Fortin-Pellerin, É. (2018). Assessing the impacts of total liquid ventilation on left ventricular diastolic function in a model of neonatal respiratory distress syndrome. *PLoS One*, 13(1), e0191885.
- Sanchez, B., Vandersteen, G., Martin, I., Castillo, D., Torrego, A., Riu, P. J., Schoukens, J., & Bragos, R. (2013). In vivo electrical bioimpedance characterization of human lung tissue during the bronchoscopy procedure. a feasibility study. *Medical Engineering & Physics*, 35(7), 949–957.
- Schöberl, J. (1997). NETGEN an advancing front 2d/3d-mesh generator based on abstract rules. *Comput Visual Sci*, 1(1), 41–52.

- Schuessler, T., & Bates, J. (1995). Utility of an esophageal reference electrode for thoracic electrical impedance tomography. *Proceedings of 17th International Conference of the Engineering in Medicine and Biology Society*, 1, 559–560 vol.1.
- Smit, H. J., Handoko, M. L., Noordegraaf, A. V., Faes, T. J. C., Postmus, P. E., Vries, P. M. J. M. d., & Boonstra, A. (2003). Electrical impedance tomography to measure pulmonary perfusion: Is the reproducibility high enough for clinical practice? *Physiol. Meas.*, 24(2), 491–499.
- Solà, J., Adler, A., Santos, A., Tusman, G., Sipmann, F. S., & Bohm, S. H. (2011). Non-invasive monitoring of central blood pressure by electrical impedance tomography: First experimental evidence. *Medical and Biological Engineering and Computing*, 49(4), 409–15.
- Soleimani, M., Gómez-Laberge, C., & Adler, A. (2006). Imaging of conductivity changes and electrode movement in EIT. *Physiol. Meas.*, 27(5), S103–S113.
- Somersalo, E., Cheney, M., & Isaacson, D. (1992). Existence and uniqueness for electrode models for electric current computed tomography. *SIAM Journal on Applied Mathematics*, 52(4), 18.
- Sourbron, S. P., & Buckley, D. L. (2013). Classic models for dynamic contrast-enhanced MRI. *NMR in Biomedicine*, 26(8), 1004–1027.
- Šribar, A., Merc, V., Peršec, Z., Peršec, J., Milas, I., & Husedžinović, S. (2020). Influence of different PEEP levels on electrical impedance tomography findings in

- patients under general anesthesia ventilated in the lateral decubitus position.
Journal of Clinical Monitoring and Computing, 34(2), 311–318.
- Stowe, S., & Adler, A. (2020). The effect of internal electrodes on electrical impedance tomography sensitivity. *2020 42nd Annual International Conference of the IEEE Engineering in Medicine Biology Society (EMBC)*, 1457–1460.
- Stowe, S., Boyle, A., Sage, M., See, W., Praud, J.-P., Fortin-Pellerin, É., & Adler, A. (2019). Comparison of bolus- and filtering-based EIT measures of lung perfusion in an animal model. *Physiol. Meas.*, 40(5), 054002.
- Stowe, S., Samson, N., Nadeau, C., Morin, C., Praud, J.-P., Fortin-Pellerin, É., & Adler, A. (2021a). Using esophageal electrodes for increased sensitivity to cardiac-frequency impedance changes. *Proceedings of the 21st International Conference on Biomedical Applications of Electrical Impedance Tomography*, 24.
- Stowe, S., Zhao, Z., Huxter, E., He, H., Long, Y., & Adler, A. (2021b). Generating forward models from CT images for ventilation monitoring in ARDS patients. *Proceedings of the 21st International Conference on Biomedical Applications of Electrical Impedance Tomography*, 20.
- Vauhkonen, M., Vadassz, D., Karjalainen, P., Somersalo, E., & Kaipio, J. (1998). Tikhonov regularization and prior information in electrical impedance tomography. *IEEE Transactions on Medical Imaging*, 17(2), 285–293.

- Vauhkonen, P. J., Vauhkonen, M., Savolainen, T., & Kaipio, J. P. (1999). Three-dimensional electrical impedance tomography based on the complete electrode model. *IEEE Trans Biomed Eng*, *46*(9), 1150–1160.
- Vijayalakshmi, K., Kelly, D., Chapple, C.-L., Williams, D., Wright, R., Stewart, M. J., Hall, J. A., Sutton, A., Davies, A., Haywood, J., & de Belder, M. A. (2007). Cardiac catheterisation: Radiation doses and lifetime risk of malignancy. *Heart*, *93*(3), 370–371.
- Vonk-Noordegraaf, A., Kunst, P. W. A., Janse, A., Marcus, J. T., Postmus, P. E., Faes, T. J. C., & Vries, P. M. J. M. d. (1998). Pulmonary perfusion measured by means of electrical impedance tomography. *Physiol. Meas.*, *19*(2), 263–273.
- Waldmann, A. D., Wodack, K. H., März, A., Ukere, A., Trepte, C. J., Böhm, S. H., & Reuter, D. A. (2017). Performance of novel patient interface for electrical impedance tomography applications. *J. Med. Biol. Eng.*, *37*(4), 561–566.
- Watson, R. E. (2015). Lessons learned from MRI safety events. *Curr Radiol Rep*, *3*(10), 37.
- Witsoe, D. A., & Kinnen, E. (1967). Electrical resistivity of lung at 100 kHz. *Med. & biol. Engng.*, *5*(3), 239–248.
- Yang, L., Dai, M., Möller, K., Frerichs, I., Adler, A., Fu, F., & Zhao, Z. (2021). Lung regions identified with CT improve the value of global inhomogeneity index measured with electrical impedance tomography. *Quant Imaging Med Surg*, *11*(4), 1209–1219.

- Zadehkoochak, M., Blott, B. H., Hames, T. K., & George, R. F. (1992). Pulmonary perfusion and ventricular ejection imaging by frequency domain filtering of EIT images. *Clin. Phys. Physiol. Meas.*, 13, 191–196.
- Zhao, Z., Fischer, R., Frerichs, I., Müller-Lisse, U., & Möller, K. (2012). Regional ventilation in cystic fibrosis measured by electrical impedance tomography. *Journal of Cystic Fibrosis*, 11(5), 412–418.
- Zhao, Z., Möller, K., Steinmann, D., Frerichs, I., & Guttmann, J. (2009). Evaluation of an electrical impedance tomography-based global inhomogeneity index for pulmonary ventilation distribution. *Intensive Care Medicine*, 35(11).

Appendices

Appendix A

GMSH models

A.1 Tank model

A.2 Internal probe model

Appendix B

Algorithms

B.1 External boundary

The following steps were used to segment the external boundary from a single slice of a CT image using Matlab 2021b with the image processing toolbox:

Algorithm 1: Segment the external body boundary.

Input: image

Output: external boundary

- 1 weiner filter;
 - 2 Set the lung intensity to 0;
 - 3 erode image using disk size 20;
 - 4 reconstruct on image from line 4;
 - 5 dilate with disk of size 20;
 - 6 reconstruct on image from line 6;
 - 7 binarize, thresh = 0.5;
 - 8 fill holes;
 - 9 close using disk size = 2;
 - 10 open using disk size = 5;
 - 11 external boundary = largest object;
-

B.2 Ribcage

B.3 Lungs